

https://dspace.org/

Prospects of gibbsite-rich laterite as a source of aluminosilicates in geopolymerisation

Gilayeneh, Victor Saye

2024
University of the Witwatersrand, Johannesburg
https://hdl.handle.net/10539/45420
Gilayeneh, Victor Saye . (2024). Prospects of gibbsite-rich laterite as a source of aluminosilicates in geopolymerisation [PhD thesis, University of the Witwatersrand, Johannesburg]. WIReDSpace. https://hdl.handle.net/10539/45420

Downloaded from a DSpace repository. https://dspace.org/

PROSPECTS OF GIBBSITE-RICH LATERITE AS A SOURCE OF ALUMINOSILICATES IN GEOPOLYMERISATION

Victor Saye Gilayeneh

A thesis submitted to the Faculty of Engineering and the Built Environment, University of the Witwatersrand, Johannesburg, in fulfilment of the requirements for the degree of Doctor of Philosophy in Engineering.

Johannesburg, 2024

DECLARATION

I declare that this thesis is my own unaided work. It is being submitted for the Degree of Doctor of Philosophy in Engineering to the University of the Witwatersrand, Johannesburg. It has not been submitted before for any degree or examination to any other university.



……

2nd day of September 2024

ABSTRACT

Laterite, an iron-rich soil widely found in the tropical and subtropical regions of the world, has shown promise for the development of eco-friendly construction materials through geopolymerisation. However, this material varies greatly in composition based on location, prevailing climate conditions, and even in depth within a given lateritic profile. The top layer of most lateritic profiles is usually low in kaolinite but rich in aluminium or iron hydroxide minerals. Despite these variations, research on the use of laterite in geopolymerisation has predominantly focused on materials rich in kaolinite.

Therefore, this study explores the potential of aluminium-rich laterite as a source of aluminosilicates in geopolymerisation. In this study, the reaction kinetics, setting times, flow behaviour, strength development, phase composition, and pore structure of geopolymer derived from aluminous laterite were examined. This study also considered both calcined and uncalcined laterite as well as the influence of calcium minerals, namely calcium carbonate ($CaCO_3$) and Portland cement, which replaced 40% of the laterite. In addition, the influence of the laterite's properties on the performance of the derived geopolymer was also examined.

The flow behaviour of the paste was found to be influenced by the viscosity of the activating solution, while the setting times and heat of reaction varied according to the type of laterite and the presence of calcium carbonate or Portland cement, which reduced the setting times and accelerated the rate of heat liberation within the first hour of the isothermal calorimetry test. The geopolymer mix based on calcined laterite displayed the highest amount of heat liberated, while its uncalcined laterite counterpart showed the lowest. All mixes within the calcined laterite series exhibited higher compressive strength than those in the uncalcined series, but only the calcined laterite mixes containing calcium minerals achieved structural strength. The uncalcined laterite mixes experienced strength regressions, with samples of the uncalcined laterite mix containing calcium carbonate developing cracks and subsequently disintegrating. The phase assemblage, porosity and pore structure were also influenced by the type of laterite and the presence of calcium carbonate or Portland cement. However, the presence of calcium carbonate also led to severe efflorescence and subflorescence, which negatively impacted the porosity and structural integrity. Also, the dissolution of gibbsite initiated the development of unstable phases in the uncalcined laterite mixes within the geopolymer and hybrid categories. Conversely, in the absence of activators, especially sodium hydroxide, as demonstrated in the binary mix containing uncalcined laterite, the dissolution of gibbsite is inhibited, resulting in the formation of stable phases.

ACKNOWLEDGEMENT

With utmost gratitude, I offer my praises and thanks to God Almighty, the source of all wisdom and understanding, for the strength and perseverance bestowed upon me during this challenging academic journey. It is through His grace that I have been able to complete this work.

I am pleased to extend my deepest gratitude to Professor Sunday Nwaubani and Professor Mike Otieno for their exceptional mentorship, scholarly guidance, unwavering commitment to excellence, and steadfast support during my doctoral studies. Their expertise, consistent encouragement, and invaluable feedback have been instrumental in shaping the trajectory of this thesis and the direction of my research.

I am also profoundly thankful to the University of the Witwatersrand for the financial support provided through the Postgraduate Merit Award. Special recognition is also extended to the School of Civil and Environmental Engineering for the bursary facilitated by Professor Mike Otieno, as well as for providing the necessary resources and facilities for conducting this research.

I would like to convey my heartfelt gratitude to the Microscopy and Microanalysis Unit of the University of the Witwatersrand for granting me access to their state-of-the-art XRD and SEM equipment, as well as for providing the required training. I also extend my sincere thanks to the School of Chemical and Metallurgical Engineering for the use of their TGA and FTIR equipment, and to their dedicated technicians, Letta Ntuli and Matshidiso Tsotetsi, for conducting the TGA and FTIR analyses, which significantly broadened the scope of my research.

Finally, I extend my heartfelt appreciation to my family and friends for their steadfast support, sacrifices, patience, and understanding, as well as their continuous encouragement throughout this demanding journey. I would not have reached this milestone without them; their enduring love and firm belief in me have served as a source of strength and motivation.

TABLE OF CONTENTS

DECLARATION ..... **I**

ABSTRACT ..... **II**

ACKNOWLEDGEMENT ..... **III**

List of Figures ..... **VII**

List of Tables ..... **IX**

List of Abbreviations and Notations ..... **X**

Chapter 1: Introduction **1**

1.1 Background and Motivation 1

1.2 Research Aim 3

1.3 Objectives 3

1.4 Scope and Limitations 3

1.5 Thesis Outline 4

1.6 References 4

Chapter 2: Literature Review **7**

2.1 Introduction 7

2.2 Geopolymer 7

2.2.1 Overview of Geopolymer 7

2.2.2 Historical Background and Development of Geopolymer 8

2.2.3 Classification of Geopolymers 10

2.2.4 Mechanism and Chemistry of Geopolymerisation 10

2.2.5 Factors Influencing the Properties and Performance of Geopolymer 12

2.2.6 Applications of Geopolymers 14

2.3 Laterite 14

2.3.1 Definition of Laterite 14

2.3.2 Formation of Laterite 15

2.3.3 Characteristics and Composition of Laterite 16

2.3.4 Variations in Lateritic Profiles 18

2.4 Laterite in Geopolymerisation: Research Trends and Findings 18

2.5 Summary 22

2.6 References 23

Chapter 3: Materials and Characterisation 29
3.1 Introduction 29
3.2 Materials 29
3.2.1 Laterite 29
3.2.2 Calcium Carbonate 34
3.2.3 Portland Cement 35
3.2.4 Activators 37
3.2.5 Fine Aggregate 38
3.3 Processing of the Laterite 39
3.4 Characterisation of the Laterite 41
3.5 Summary 48
3.6 References 48
Chapter 4: Experimental Methods and Procedures 52
4.1 Introduction 52
4.2 Overview of the Laboratory Investigation 52
4.3 Mix Designs 53
4.4 Casting and Curing Procedure 57
4.5 Fresh Properties 59
4.5.1 Flow Table Test 59
4.5.2 Setting Times 59
4.5.3 Heat of Reaction 60
4.6 Compressive Strength Testing 61
4.7 Microstructural Characterisation 61
4.7.1 Porosity and Pore Structure 61
4.7.2 Phase Identification 66
4.8 Summary 67
4.9 References 67
Chapter 5: Results and Discussion 70
5.1 Introduction 70
5.2 Fresh Properties 71
5.2.1 Setting Times 71
5.2.2 Spread Flow Diameter 73
5.2.3 Heat of Reaction 75

5.3 Compressive Strength 77
5.4 Microstructural Analyses 79
5.4.1 Pore Structure and Porosity 79
5.4.2 Phase Identification 85
5.5 Summary 97
5.6 References 98
Chapter 6: Conclusions and Recommendations 100
6.1 Introduction 100
6.2 Conclusions 101
6.2.1 Impact of Milling and Calcination 101
6.2.2 Factors Influencing the Reactivity of the Laterite 102
6.2.3 Factors Influencing Rheology and Flow Behaviour 102
6.2.4 Factors Influencing Properties and Performance of the Derived Geopolymer 103
6.3 Implications and Practical Applications 104
6.4 Limitations of Findings 105
6.5 Recommendations for Further Research 105

List of Figures

Figure 3.1: Picture of the laterite at the extraction site. 30
Figure 3.2: Sieve analysis of the extracted laterite. 30
Figure 3.3: XRD spectrum of the as-received laterite. 31
Figure 3.4: Thermograms of the as-received laterite. 32
Figure 3.5: XRD spectrum of the calcium carbonate. 34
Figure 3.6: FTIR spectrum of the calcium carbonate. 34
Figure 3.7: Particles micrograph of the calcium carbonate powder. 35
Figure 3.8: XRD spectrum of the Portland cement. 36
Figure 3.9: FTIR spectrum of the Portland cement. 36
Figure 3.10: Particle size distribution of the Portland cement. 37
Figure 3.11: Particles micrograph of the Portland cement. 37
Figure 3.12: Particle size grading curve of the fine aggregate. 38
Figure 3.13: Vibratory disc mill. 40
Figure 3.14: (a) Pulverised laterite (b) Milled or ground laterite. 40
Figure 3.15: (a) Uncalcined laterite (b) Calcined laterite. 40
Figure 3.16: Particle size distribution curves of uncalcined and calcined laterite. 42
Figure 3.17: SEM particle micrograph: (a) Uncalcined laterite (b) Calcined laterite. 42
Figure 3.18: XRD spectra of the laterites. 43
Figure 3.19: Crystallinity of the laterites. 44
Figure 3.20: Thermograms of the laterites. 46
Figure 3.21: FTIR spectra of the laterites. 47
Figure 4.1: Schematic of the laboratory investigation. 53
Figure 4.2: Influence of curing regime on the compressive strength of mix H-CL/CC. 58
Figure 4.3: Flow table apparatus. 59
Figure 4.4: Setup of the isothermal calorimeter. 61
Figure 4.5: Samples of 34-mm paste cube. 63
Figure 4.6: Rate of isopropanol diffusion through the trial sample. 64
Figure 4.7: Setup of the Helium Pycnometer. 65
Figure 5.1: Setting times of the mixes. 71
Figure 5.2: Spread flow diameter of the mixes. 73
Figure 5.3: Images of spread diameter of the pastes. 74
Figure 5.4: Images of spread diameter of the mortars. 74

Figure 5.5: Heat of reaction of the mixes. 75
Figure 5.6: Cumulative exothermic heat of reaction of the mixes. 76
Figure 5.7: Compressive strength of the mixes. 78
Figure 5.8: Cube samples of mix H-UL/CC after 56 days of casting. 79
Figure 5.9: Isopropanol diffusion rate in paste samples of mix G-CL. 80
Figure 5.10: Isopropanol diffusion rate in paste samples of mix G-UL. 80
Figure 5.11: Isopropanol diffusion rate in paste samples of mix H-CL/CC. 81
Figure 5.12: Isopropanol diffusion rate in paste samples of mix H-UL/CC. 81
Figure 5.13: Isopropanol diffusion rate in paste samples of mix H-CL/PC. 81
Figure 5.14: Isopropanol diffusion rate in paste samples of mix H-UL/PC. 82
Figure 5.15: Isopropanol diffusion rate in paste samples of mix B-CL/PC 82
Figure 5.16: Isopropanol diffusion rate in paste samples of mix B-UL/PC. 82
Figure 5.17: Samples of mix H-CL/CC at 90 days after casting. 83
Figure 5.18: Porosity of the mixes obtained by Solvent Exchange. 84
Figure 5.19: Porosity of the mixes obtained by Helium Pycnometry. 85
Figure 5.20: Sample of mix H-CL/CC at 180 Days: (a) Isometric view (b) Top view. 85
Figure 5.21: XRD spectra of mix G-CL. 87
Figure 5.22: XRD spectra of mix G-UL. 87
Figure 5.23: XRD spectra of mix H-CL/CC. 88
Figure 5.24: XRD spectra of mix H-UL/CC 89
Figure 5.25: XRD spectra of mix H-CL/PC. 90
Figure 5.26: XRD spectra of mix H-UL/PC. 90
Figure 5.27: XRD spectra of mix B-CL/PC 91
Figure 5.28: XRD spectra of mix B-UL/PC. 92
Figure 5.29: FTIR spectra of mix G-CL. 93
Figure 5.30: FTIR spectra of mix G-UL. 93
Figure 5.31: FTIR spectra for mix H-CL/CC. 94
Figure 5.32: FTIR spectra of mix H-UL/CC. 94
Figure 5.33: FTIR spectra of mix H-CL/PC. 95
Figure 5.34: FTIR spectra of mix H-UL/PC. 96
Figure 5.35: FTIR spectra of mix B-CL/PC. 97
Figure 5.36: FTIR spectra of mix B-UL/PC. 97

List of Tables

Table 3.1: Major oxide composition of the as-received laterite. 31
Table 3.2: Major oxide composition of Portland cement. 35
Table 3.3: Physical properties of the uncalcined and calcined laterite. 42
Table 4.1: Mix design of mortar per unit volume. 54
Table 4.2: Impact of activator dosage on compressive strength of mix G-CL. 55
Table 4.3: Effects of metasilicate water content on the mixing solution. 56
Table 4.4: pH and molarity of the mixing solution when using liquid sodium silicate. 56
Table 4.5: Impact of calcium carbonate on compressive strength. 57

List of Abbreviations and Notations

Abbreviation

DSC	Differential Scanning Calorimetry
DTA	Differential Thermal Analysis
FTIR	Fourier Transform Infrared Spectroscopy
SEM	Scanning Electron Microscopy
TGA	Thermogravimetric Analysis
XRD	X-ray Diffraction
XRF	X-ray Fluorescence

Notation

B-CL/PC	Binary mix made of calcined laterite and Portland cement
B-UL/PC	Binary mix made of uncalcined laterite and Portland cement
G-CL	Geopolymer mix made of calcined laterite
G-UL	Geopolymer mix made of uncalcined laterite
H-CL/CC	Hybrid mix made of calcined laterite and calcium carbonate
H-CL/PC	Hybrid mix made of calcined laterite and Portland cement
H-UL/CC	Hybrid mix made of uncalcined laterite and calcium carbonate
H-UL/PC	Hybrid mix made of uncalcined laterite and Portland cement
MeO	Metal oxide where the metal has a valence of +2
Me_2O	Metal oxide where the metal has a valence of +1
Me_2O_3	Metal oxide where the metal has a valence of +3
N-A-S-H	Sodium aluminosilicate hydrate
C-A-S-H	Calcium aluminate silicate hydrate
C-(N)-A-S-H	Calcium aluminate silicate hydrate incorporating sodium ions
C-S-H	Calcium silicate hydrate
W_t	Quantity of isopropanol diffusing after a given time
D_{ISO}	Density of isopropanol
D_w	Density of water
M_i	Initial mass of the sample
M_t	Mass of the sample after a given time
P_{SSM}	Porosity obtained from the solvent-saturated mass

SS_M	Solvent-saturated mass
OD_M	Oven-dry mass of the sample
P_{IM}	Porosity derived from the sample's initial mass
P_{HP}	Porosity obtained by Helium pycnometry
V_A	Apparent volume or bulk volume
V_T	True volume of the sample

Chapter 1

Introduction

1.1 Background and Motivation

Cement-based materials play an integral role in today's society and have become the preferred choice for most construction applications [1]. These materials now constitute the largest portion of the built environment and have significantly facilitated global development and industrialisation [2]. This remarkable advancement is primarily accredited to the emergence of Portland cement, a technological milestone in the history of humanity [3].

Despite the considerable benefits of Portland cement, some reservations have emerged. From an environmental standpoint, the production of Portland cement is characterised by high energy consumption and substantial greenhouse gas emissions, accounting for an estimated 8% of the world's total CO_2 emissions and ranking as the third-largest industrial energy consumer [1,2]. In addition, concerns extend to the economic landscape, where the high cost and limited availability of Portland cement, particularly in low-income countries across Africa, present significant challenges [4–6]. This disparity in cost has also prompted urgent considerations for exploring and implementing alternative cement solutions.

The need for eco-friendly and affordable cement has become the primary driving force behind the research and development of alternative cement, including those based on alkali or acid activation technology. Within this category lies a distinct class of materials known as geopolymers. Geopolymers are inorganic polymeric materials synthesised through the reaction of aluminosilicate precursors with alkaline reagents, a process known as geopolymerisation. These materials consist of chains or networks of molecules linked by covalent bonds and have a broad range of applications [7]. In the context of cement-based applications, geopolymers have demonstrated performance comparable to Portland cement, along with a lower carbon footprint [8,9].

Geopolymer technology presents a promising opportunity for producing cost-effective and environmentally friendly cement-based materials, a potential solution for addressing the demand for affordable housing in countries experiencing pronounced economic, social, and

infrastructural challenges. However, the successful deployment of geopolymer technology relies heavily on securing an abundant source of aluminosilicates, as the accessibility of readily available precursors is one of the factors influencing the acceptance and utilisation of alkali-activated binders [10].

Recognizing the significant challenge posed by the limited access to industrial wastes, such as fly ash, in underdeveloped and less-industrialized nations, there is an urgent need for alternative sources of aluminosilicate materials to effectively implement geopolymer technology. In this context, geological materials stand out as the primary source of aluminosilicates that demand exploration in these regions [11]. One such geological material is laterite or lateritic soil, which remains largely overlooked despite its immense potential. Laterite and lateritic materials exist in huge quantities that exceed the projected global production of cement-based materials [10].

Laterites, constituting one-third of the Earth's land surface [12], are reddish or rust-coloured soils primarily found in tropical and subtropical regions. These materials are developed through prolonged weathering of underlying parent rock and are characterised by high iron and aluminium content. Quartz, goethite, hematite, kaolinite, and gibbsite are among the minerals usually found in laterite. Laterites are poorly crystalline materials and exhibit reactivity in finely divided form [13].

The use of laterite as a construction material dates back a millennium, where laterite soil was cut into large blocks and employed in constructing temples in Southeast Asia [14]. Beyond this historical significance, laterite continues to play a vital role in modern construction practices, serving as a compressed stabilized earth block, material for road base and surface pavement, as well as a substitute for Portland cement. As a replacement material for cement, calcined laterite has been proven to exhibit pozzolanic behaviour [15,16], making it an attractive option for sustainable construction, especially in the context of geopolymerisation.

As a source of aluminosilicates, laterite has shown promise in the development of indigenous sustainable cement-based materials through geopolymerisation [17–19]. However, laterite varies greatly in composition based on location, prevailing climate, and even in depth within a given lateritic profile. The top layer of most lateritic profiles is usually low in kaolinite but rich in aluminium or iron minerals. Despite these variations, research on the use of laterite in geopolymerisation has predominantly focused on materials rich in kaolinite.

Given the limitations of focusing solely on kaolinite-rich laterite, investigating other types of laterites, such as those rich in aluminium, becomes imperative. The vast availability of

aluminium-rich laterite, particularly across West Africa and South America [20,21], presents a significant opportunity for the development of sustainable construction materials. This readily accessible resource, often found near the surface, requires minimal excavation compared to deeper kaolinite-rich layers. Therefore, motivated by these prospects, this study seeks to explore the potential of aluminium-rich laterite as a source of aluminosilicates in geopolymerisation.

1.2 Research Aim

This research aimed to evaluate the viability of utilising aluminium-rich or aluminous laterite in producing sustainable cement-based materials through geopolymerisation.

1.3 Objectives

The objectives of this study were as follows:

1. To conduct an extensive literature review on the properties, microstructure and durability performance of geopolymers derived from laterite in order to identify current gaps and develop an appropriate research methodology.
2. To characterise the physical, chemical and mineralogical properties of the aluminium-rich laterite to be used in this investigation.
3. To investigate the rheology, setting times and the heat release during geopolymerisation.
4. To investigate the compressive strength development of the geopolymer derived from aluminium-rich laterite.
5. To characterise the products of geopolymerisation and the pore structure of the hardened material derived from aluminous laterite.

1.4 Scope and Limitations

The scope of this research covered the examinations of fresh and hardened properties of the material synthesized from aluminium-rich laterite through geopolymerisation, along with a comprehensive characterisation of the aluminous laterite itself. The fresh properties examination included rheology, setting times, and reaction kinetics. As for the hardened properties, the focus was on compressive strength development and microstructural characterisations with respect to pore structure and porosity, as well as phase identification of the product of geopolymerisation. Although the activator types, dosages and the impact of curing regimes on the strength development were covered during the preliminary investigation

of the mix design optimisation process, these factors, including acid resistance, soundness in water and the impact of silicate modulus, have been extensively addressed in previous studies to the extent that reasonable inferences can be drawn in relation to other materials. Consequently, these aspects were not within the scope of this study.

1.5 Thesis Outline

This thesis is structured into six chapters, with each chapter making a distinct contribution towards exploring the potential of utilising aluminium-rich laterite as a source of aluminosilicate in geopolymerisation. A comprehensive literature review on the fundamental concepts of geopolymerisation and historical perspectives, as well as a critical assessment of the existing body of knowledge on the use of laterite in geopolymerisation, are presented in Chapter 2. Chapter 3 provides an in-depth description of the laterite and other materials used in this study, with a specific focus on detailing the processes and procedures involved in characterising the aluminium-rich laterite. The experimental procedures and methods employed in the laboratory investigation are outlined in Chapter 4, while Chapter 5 presents the results of the laboratory investigation. To conclude the thesis, Chapter 6 summarises key findings, acknowledges limitations, and proposes recommendations for future research, building upon insights gained during the investigation.

1.6 References

1. Schneider, M., The Cement Industry on the Way to a Low-Carbon Future, *Cement and Concrete Research*. (2019) **124** 105792.
2. Scrivener, K.L., John, V.M., Gartner, E.M., Eco-Efficient Cements: Potential Economically Viable Solutions for a Low-CO2 Cement-Based Materials Industry, *Cement and Concrete Research*. (2018) **114** 2–26.
3. Shi, C., Jiménez, A.F., Palomo, A., New Cements for the 21st Century: The Pursuit of an Alternative to Portland Cement, *Cement and Concrete Research*. (2011) **41** 750–763.
4. Schmidt, W., Peculiarities of African Cement and Concrete Markets - Challenges and Opportunities, In: *Bauma Africa 2013 - Global Issues in Concrete Construction - Markets, Perspectives, Technologies (Proceedings)*, (2013): pp. 25–28.
5. Schmidt, W., Potentials for Sustainable Cement and Concrete Technologies - Comparison between Africa and Europe, In: *Proceedings of the 1st International Conference on Construction Materials for a Sustainable Future*, (2017): pp. 829–835.

6. Schmidt, W., Ngassam, I.L.T., Breitschaft, G., Virchow, S., Challenges of the Growing African Cement Market – Environmental Issues, Regulative Framework, and Quality Infrastructure Requirements, *MATEC Web of Conferences*. (2018) **149**.
7. Davidovits, J., Introduction, In: *Geopolymer Chemistry and Applications*, 5th edition, (2020).
8. Duxson, P., Fernández-Jiménez, A., Provis, J.L., Lukey, G.C., Palomo, A., van Deventer, J.S.J., Geopolymer Technology: The Current State of the Art, *Journal of Materials Science*. (2007) **42** 2917–2933.
9. Duxson, P., Provis, J.L., Lukey, G.C., Van Deventer, J.S.J., The Role of Inorganic Polymer Technology in the Development of 'Green Concrete,' *Cement and Concrete Research*. (2007) **37** 1590–1597.
10. Provis, J.L., Alkali-Activated Materials, *Cement and Concrete Research*. (2018) **114** 40–48.
11. Mcintosh, A., Lawther, S.E.M., Kwasny, J., Soutsos, M.N., Cleland, D., Nanukuttan, S., Selection and Characterisation of Geological Materials for Use as Geopolymer Precursors, *Advances in Applied Ceramics*. (2015) **114** 378–385.
12. Tardy, Y., Laterites, In: *Sedimentology*, Springer, Berlin, Heidelberg, (1978): pp. 668–672.
13. Wagh, A.S., Introduction to Chemically Bonded Ceramics, In: *Chemically Bonded Phosphate Ceramics: Twenty-First Century Materials with Diverse Applications*, Elsevier, (2016).
14. Schellmann, W., Home - An Introduction in Laterite, Available: http://www.laterite.de.
15. Nwaubani, S.O., Properties, Hydration and Durability of Pozzolanic Mortars and Concrete, PhD Thesis, Department of Civil Engineering, University of Leeds, (1990).
16. Pera, T.M.J., Ambroise, J., Action of Some Aggressive Solutions on Portland and Calcined Laterite Blended Cement Concretes, *Special Publication*. (1992) **132** 763–780.
17. Obonyo, E.A., Kamseu, E., Lemougna, P.N., Tchamba, A.B., Melo, U.C., Leonelli, C., A Sustainable Approach for the Geopolymerization of Natural Iron-Rich Aluminosilicate Materials, *Sustainability*. (2014) **6** 5535–5553.
18. Lemougna, P., Madi, A., Kamseu, E., Melo, U., Delplancke, M., Rahier, H., Influence of the Processing Temperature on the Compressive Strength of Na Activated Lateritic Soil for Building Applications, *Construction and Building Materials*. (2014) **65** 60–66.
19. Gualtieri, M.L., Romagnoli, M., Pollastri, S., Gualtieri, A.F., Inorganic Polymers from Laterite Using Activation with Phosphoric Acid and Alkaline Sodium Silicate Solution:

Mechanical and Microstructural Properties, *Cement and Concrete Research*. (2015) **67** 259–270.

20. Tardy, Y., Kobilsek, B., Paquet, H., Mineralogical Composition and Geographical Distribution of African and Brazilian Periatlantic Laterites. The Influence of Continental Drift and Tropical Paleoclimates during the Past 150 Million Years and Implications for India and Australia, *Journal of African Earth Sciences (and the Middle East)*. (1991) **12** 283–295.
21. Monsels, D.A., Bauxite Deposits in Suriname: Geological Context and Resource Development, *Netherlands Journal of Geosciences*. (2016) **95** 405–418.

Chapter 2

Literature Review

2.1 Introduction

Geopolymers, formed through chemical activation of aluminosilicate materials, offer a wide range of desirable properties, including high mechanical strength and outstanding fire resistance, and have since found applications in several industries. However, the use of geopolymer in cement-based applications has gained the most attention, primarily due to perceived environmental benefits such as reduced greenhouse gas emissions (CO_2) and the utilisation of waste materials.

Therefore, this chapter presents a literature review on geopolymers, with an emphasis on their use in cement-based applications. The review encompasses various aspects, including the historical development of geopolymers, fundamental concepts of geopolymerisation, and factors influencing the properties and performance of geopolymers. In addition, this review covers the use of laterite as a source of aluminosilicates, capturing relevant research trends and findings. This chapter also presents a discussion on laterite, a geological material abundant in tropical and subtropical regions, covering its formation processes, characteristics, composition, and inherent variations in lateritic profiles.

2.2 Geopolymer

2.2.1 Overview of Geopolymer

Geopolymer generally refers to a class of inorganic polymeric materials synthesised through chemical reaction of aluminosilicate materials containing little or no calcium oxide with an alkaline or acidic reagent. These aluminosilicate-sourced materials are called ‘precursors’ and are usually industrial wastes such as fly ash and slags, which may not require further processing. However, geological materials like calcined kaolin clay (metakaolin) and volcanic ash are also popular choices of precursors for geopolymerisation.

This intriguing class of materials is distinguished by its three-dimensional network structure, consisting of repeating tetrahedral frameworks of SiO_4^{4-} and AlO_4^{5-} linked by shared oxygen

atoms [1]. These repeating frameworks attract alkali metal ions (such as Na^+, K^+, and Li^+) to counterbalance the negative charge of the aluminate tetrahedra (AlO_4), gained as a result of replacing the silicate tetrahedra in the chain network, as is the case for alkaline activation [2,3]. In contrast, for acid activation, typically carried out with phosphoric acid, phosphate tetrahedra (PO_4^{3+}) are incorporated into the three-dimensional network, also replacing SiO_4^{4-} and counterbalancing the negative charge of the aluminate tetrahedral [4,5].

The precursors generally provide the silicate and aluminate components. However, these components can also be supplied by the reagents or activators. It is worth mentioning that, in addition to aluminium, silicon, and oxygen, other elements may be present in the geopolymeric network depending on the chemical composition of the precursor and the activators used in the synthesis process. The ability of the geopolymeric network to incorporate other elements is an exciting property that makes geopolymers suitable for hazardous waste encapsulation and immobilization [6,7].

2.2.2 Historical Background and Development of Geopolymer

The term 'geopolymer' was introduced by Joseph Davidovits, a French chemist, in the late 1970s. Davidovits coined this term to describe a new class of inorganic polymeric material he formulated by reacting calcined kaolin clay (metakaolin) with sodium hydroxide [8,9]. The resulting product exhibited an intriguing structure, ranging from amorphous to semi-crystalline, and a complex three-dimensional polymeric network comprising SiO_4 and AlO_4 tetrahedra. This network arrangement resembled that of naturally occurring zeolites, a geological material, hence the name 'Geopolymer' [9].

However, the concept of synthesizing materials similar to naturally occurring minerals from aluminosilicates dates back to the early 19th century [10,11]. As revealed by Provis [12], a 1908 patent indicates that a German cement chemist by the name of Kühl was the first to react slag (an aluminosilicate precursor) with alkali to produce cement-like material. Kühl is reported to have investigated the setting behaviour and performance of slag mixed with an alkali activator (potash powder), with the intention of developing a binder [11,13].

In 1937, a pioneering metallurgist named Chassevent investigated the reactivity of various slags with the aim of developing a more efficient metallurgical process and also reducing industrial waste. Chassevent is also credited for employing caustic potash and soda solutions in the investigation of slag reactivity [14]. Another interesting milestone in the history of alkaline activation was reached when Purdon, in 1940, conducted an extensive investigation

into the use of blast furnace slag in the development of clinker-less cement [3,11]. Purdon is credited with the first detailed scientific publication in the field of alkali activation [15], where he examined the reaction of slag with sodium hydroxide and various sodium salts, with or without calcium hydroxide, and reported conclusions that remain valuable to modern practices. These include insights into mixing procedures, strength development, low permeability, and the heat of hydration of alkali-activated slag [12,15].

These developments were followed by Victor Glukhovsky's pioneering investigation into the use of low-calcium or calcium-free aluminosilicate precursors, such as kaolin clay. In the late 1950s, Glukhovsky conducted research on these precursors, as well as on slags, in alkaline activation, in response to the shortage of Portland cement in the former Soviet Union [11,16]. Victor Glukhovsky is also credited with pioneering the use of alkali silicates in alkaline activation of aluminosilicate precursors, as well as being the first to propose a model that describes the reaction mechanism of alkaline activation. This proposed model consists of three stages: destruction–coagulation, coagulation–condensation, and condensation–crystallisation [17]. Glukhovsky also proposed two systems for classifying alkali-activated binders based on the composition of the precursor. These systems include the alkaline binding system (Me_2O-Me_2O_3-SiO_2-H_2O) and the alkaline earth binding system (Me_2O-MeO-Me_2O_3-SiO_2-H_2O) [3,11].

The notations Me_2O, MeO, and Me_2O_3 denote metal oxides, where the metal has valences of +1, +2, and +3, respectively. Today, based on the most common alkaline activators and precursors, these systems are described as (Na, K)$_2$O-Al_2O_3-SiO_2-H_2O and (Na, K)$_2$O-CaO-Al_2O_3-SiO_2-H_2O for the alkaline and alkaline earth, also now considered the low-calcium and high-calcium system, respectively [3,17]. Glukhovsky and his research team were pivotal in the development and deployment of alkali-activated blast-furnace slag within the former Soviet Union, facilitating their widespread use in various construction applications, including high-rise residential buildings, railway sleepers, concrete pavements, and drainage systems [18,19].

After this period, interest in alkaline activation declined due to the widespread availability of Portland cement in Europe. Only in the early 1980s was interest in alkaline activation reignited, principally due to the works of Davidovits [2,18]. The sudden resurgence in interest was mainly driven by the potential for use in cement-based applications, especially regarding rapid strength development and low carbon footprint. Since the renewed interest, the term 'geopolymer' has gained widespread acceptance to describe the group of materials linked to the [Me_2O-Me_2O_3-

SiO_2-H_2O] system described by Victor Glukhovsky, which is now recognised as the low-calcium system of alkali-activated binders or alkaline cements [3,11].

Alkaline cement, a term introduced by Pavlo Kryvenko in 1986, refers to binders consisting of amorphous or vitreous aluminosilicates whose cementitious properties are activated or enhanced in the presence of alkalis [3,17]. In addition to the low- and high-calcium systems, alkaline cement also includes a third category called hybrid, which is an intermediate system derived from the combination of high-calcium and low-calcium precursors. As a result, the hybrid system may contain reaction products from both systems: a highly cross-linked calcium aluminate silicate hydrate (C-(N)-A-S-H) incorporating alkali metal ions and a three-dimensional alkali aluminosilicate gel (N-A-S-H), respectively, from the high-calcium and low-calcium systems [20].

2.2.3 Classification of Geopolymers

The diverse applications and formulation procedures associated with geopolymers have rendered it challenging to devise a single classification system. Geopolymers can be categorised based on various factors, including the nature of the gel forming, synthesis processes, and intended applications. This complexity has also led to controversies surrounding the proliferation of names and disagreements over what should be considered a geopolymer [12]. For instance, under alkaline activation conditions, geopolymers fit Victor Glukhovsky's description of the alkaline binding system and can be classified as low-calcium alkali-activated binders, with gels comprising repeating units of Si-O-Al-O in a three-dimensional tetrahedral framework. However, with phosphoric acid activation, although the gel forming contains three-dimensional tetrahedral networks, it consists of repeating units of Si-O-Al-O-P, which does not conform to the descriptions of alkali-activated binders but rather to chemically bonded ceramics. Therefore, based on the nature of the gel forming in the two most popular activating mediums, alkaline and phosphoric acid, geopolymers can be broadly classified into two main categories: alkali aluminosilicate geopolymers and silico-aluminophosphate geopolymers [21].

2.2.4 Mechanism and Chemistry of Geopolymerisation

Geopolymerisation is simply the process of forming or synthesising geopolymers. This process involves reacting powdered aluminosilicate materials with an activator, usually in liquid form, followed by the setting and hardening of the mixture. The exact mechanism of geopolymerisation is not yet fully understood but is thought to be dependent on the type of precursors and activators [2]. However, from a simplistic point of view, the mechanism of

geopolymerisation can be categorised into four stages, which may occur independently or simultaneously. The four stages are chemical attack, dissolution, precipitation of gel, and polymerisation and hardening.

The chemical attack stage is initiated when an alkaline solution comes into contact with the powdered aluminosilicate precursor during alkaline activation. The high pH of the alkaline solution breaks down the Si-O-Si, Si-O-Al, or Al-O-Al bonds in the precursors, resulting in the dissolution of the aluminosilicate particles and the release of ionic species into solution. The specific species in solution depend on the nature of the precursor, with silicate (Si^{4+}) and aluminate (Al^{3+}) being dominant for low-calcium precursors. It should be noted that the formulation of geopolymer also involves the use of solid alkaline activators (in powder form), which can be mixed or calcined with the aluminosilicate powder before adding water [22,23]. This procedure is often referred to as the "Just-add-water" or the One-part mix.

The silicate and aluminate species in solution are usually in the form of monomers. However, the amount of aluminate and silicate monomers in solution depends on the reactivity of the precursors and the type and concentration of the activators [24]. When saturation is reached, these monomers react with one another, forming dimers, trimers, and so on, thereby building the chain of the polymeric network [17,25]. This chain reaction leads to the precipitation of gels or products of geopolymerisation through condensation, polycondensation, and network formation. As the network grows, it becomes increasingly dense and interconnected (polymerisation). Eventually, the geopolymer sets and hardens due to strong covalent bonds within the network, as well as the loss of water from the system (hardening).

The resulting products of geopolymerisation under alkaline conditions are the alkali aluminosilicate gel as the main reaction product and secondary products such as chabazite, faujasite, and hydroxysodalite [17]. This alkali aluminosilicate gel (N-A-S-H), as described in Section 2.2.1, has a semi-crystalline to amorphous structure with silicon and aluminium in tetrahedral coordination within a continuous three-dimensional framework.

The formulation process for phosphoric acid activation follows the same dissolution-precipitation mechanism as alkaline activation, with the difference being that dissolution is induced by the low pH of the solution due to the high concentration of proton (H^+) ions instead of hydroxide (OH^-) ions. Under phosphoric acid conditions, the main reaction product is a silico-aluminophosphate gel, which is also three-dimensional and contains silicate, aluminate, and phosphate tetrahedra in repeating units. The phosphate tetrahedra (PO_4^3) partially replace

the silicate tetrahedral (SiO_4^4) and balance the negative charge acquired by aluminate tetrahedra, as presented in Section 2.2.1. It is worth noting that PO_4^3, as a network-forming ion, is also fully capable of taking on the role of silicate as a network-forming ion in a three-dimensional network in silica-deficient systems [26].

2.2.5 Factors Influencing the Properties and Performance of Geopolymer

Geopolymer is a unique type of inorganic polymeric materials that exhibit exceptional performance across various applications, including the construction industry. However, the inherent properties, characteristics, and performance of geopolymers are influenced by factors such as the source of aluminosilicates (precursors), the mix design, activator type and concentration, and curing regimes. An understanding of these factors and their interrelationships, particularly in the context of cement-based applications, is essential for optimising desired properties.

2.2.5.1 Nature of the Precursor

The aluminosilicate precursor is the raw material that requires activation in geopolymer formulation, and the choice and composition of raw materials significantly influence both the fresh and hardened properties of geopolymers. While fly ash, slag, and metakaolin are the commonly used aluminosilicate sources [27,28], each possesses unique physical, chemical, and mineralogical characteristics that affect their reactivity with activators, behaviour in the fresh mix, and strength development of the resulting geopolymer. For example, fly ash has a spherical shape that improves workability, while metakaolin, a highly reactive pozzolan with a larger surface area, displays high water demand and poor workability.

Aluminosilicate materials with a high amorphous content typically demonstrate enhanced reactivity with activators, leading to increased dissolution rates and, ultimately, better mechanical properties, in contrast to materials with higher crystallinity [29]. The chemical composition of the precursor(s) also influences the types of gel forming, thus impacting the properties of the geopolymer. The presence of calcium oxide, either in the primary precursor or added as a secondary, reduces the setting time, promotes strength development, and densifies the matrix due to the formation of C(N)ASH gel that coexists with the alkali aluminosilicate gel.

The nature of the raw material may sometimes prescribe imperatively the type of activators to be used and the mix design, as well as dictate the curing conditions. Low-calcium materials like metakaolin tend to exhibit long setting times under ambient conditions and often require

elevated temperature curing to achieve desirable strength. In cases where the material is deficient in alumina, such as in rice husk ash, sodium aluminate is often considered as the activator, or some secondary alumina-rich precursor is incorporated to provide alumina for the Si-O-Al network formation. Additionally, aluminosilicate material containing a high amount of alumina necessitates higher dosages of activator (alkali or phosphate) to balance the aluminate anion in the framework.

2.2.5.2 Mix designs and Activators

In mix design, the key factors influencing performance are the water-binder ratio and the dosage or concentration of activators. However, activator concentration usually becomes a concern after the selection of the activator. Similar to the Portland cement system, the water-binder ratio affects the workability of the fresh mix as well as the compressive strength and porosity of the hardened geopolymer. A higher water content generally improves workability but reduces mechanical strength and increases porosity. Although factors such as the Si/Al ratio of the aluminosilicate precursor are sometimes considered in the mix design process, their impact on the system depends on the rate of release from the precursors.

Activators, being the second most essential components in the formation of geopolymers [30], play a crucial role in the setting behaviour and flow characteristics of the fresh mix, as well as strength development. Regarding alkaline activation, sodium hydroxide and sodium silicate are the most commonly used alkaline activators for low-calcium aluminosilicate precursors and are often employed together. Sodium hydroxide and sodium silicate facilitate a faster rate of dissolution and gel precipitation, while phosphoric acid tends to exhibit a slower reaction. However, phosphoric acid activation generally results in better mechanical properties.

The presence of sodium silicate provides soluble silica that is immediately available for the geopolymerisation reaction, resulting in shorter setting times, higher strength, and a denser microstructure compared to using sodium hydroxide alone. Higher concentrations of activators accelerate the dissolution of the aluminosilicate precursor. However, excessive alkali may lead to alkali leaching or efflorescence, potentially compromising durability. While optimal concentration levels for activators have been reported, the necessary amount varies based on the precursor's dissolution rate, which is influenced by its amorphous or crystalline nature. Generally, compressive strength tends to increase with increased activator concentration up to a certain threshold.

2.2.5.3 Curing conditions or regimes

Curing conditions or regimes are another crucial factor influencing the properties and performance of hardened geopolymers. The curing process plays a pivotal role in facilitating the chemical reaction of geopolymerisation. Low-calcium aluminosilicate precursors such as metakaolin typically require high-temperature curing (40 – 80 ˚C) for optimal strength development, as elevated temperatures accelerate the geopolymerisation process, leading to faster dissolution of the aluminosilicates and precipitation of the geopolymeric gel. However, it has been observed that curing at lower temperatures for a prolonged period can improve compressive strength at later stages, while prolonged curing at high temperatures may reduce compressive strength and, in some cases, lead to complete failure [31]. Also, applying heat curing after a resting period (8 – 24 hours after casting) has been reported to result in better compressive strength and microstructural properties compared to immediate heat curing after casting. Similarly, the type of heat curing methods employed has been found to influence the properties and performance of the resulting geopolymer. Steam curing has been identified as the most effective curing method, yielding higher strength than oven curing.

2.2.6 Applications of Geopolymers

Geopolymers have a wide range of applications and are incredibly versatile due to their intrinsic physical and chemical properties [32]. Beyond their traditional usage as fire-resistant products and low CO_2 binders, geopolymers have found applications in several areas. These include waste encapsulation, water purification processes as filters and antimicrobial agents, electronics as insulators and conductors, and biomedical applications, to name a few.

2.3 Laterite

2.3.1 Definition of Laterite

The term ‘laterite’, derived from the Latin word for brick, was coined by Francis Buchanan in 1807 to describe an indurated clay soil he encountered in Malabar, India, which was being cut in the form of bricks and used for construction [33–37]. The main distinguishing features of Buchanan’s description were that the soil contained a huge amount of iron, evident from the red and yellow pigments, and hardened upon exposure to air, becoming water-resistant [34,35]. However, the term ‘laterite’ has been broadly applied to most red-coloured soils found both within and outside of the tropics, regardless of other characteristics, and this has since sparked intense debate regarding what should be classified as laterite [33,34,36].

Paton and Williams [34] have attributed the controversy to the lack of understanding of the characteristics and formation of laterite, and have asserted that tropical conditions are not generally necessary for the formation of laterite. In contrast, Tady [36] has advocated for a broader use of the term 'laterite' but proposed limiting the definition to weathered products within the zone of rubefaction. This zone, which is characterised by the reddening of soil due to the presence of hematite and goethite [36,38], falls approximately between latitudes 40˚ N and 40˚ S. Interestingly, the zone of rubefaction directly overlaps with the tropics and subtropics, which fall between latitudes 35˚ N and 35˚ S, a region generally favoured for the formation of laterite [39,40]. Therefore, adopting Tady's recommendation, laterite can be defined as a highly weathered soil that developed under intertropical conditions, enriched in iron or aluminium oxides, and varies in colour from red to reddish-brown to yellow.

It is worth highlighting that this definition includes both ferruginous and aluminous lateritic materials, as well as soft kaolinitic lithomarge and non-indurated soils. The adopted definition or meaning also encompasses both lateritic materials derived from in situ parent material (bedrock) and those derived from material transported by erosion from its original location, such as alluvial and colluvial deposits. Laterite derived from in situ material is often called residual or true laterite, while those derived from transported materials are called detrital or secondary laterite [33,41].

2.3.2 Formation of Laterite

The formation of laterite, a distinctive type of soil prevalent in tropical and subtropical regions, is intricately linked to a combination of geological and climatic factors. This process involves complex interactions between the environment and geochemical processes and can occur on various materials, including bedrock, alluvial and colluvial deposits, or reworked primary laterite [40–42]. The nature of the resulting material depends specifically on the environmental conditions and geochemical processes such as weathering and leaching. Laterite can develop from any material containing aluminosilicate and iron minerals, or ferro-aluminosilicate minerals.

However, irrespective of the type of parent material, laterite formation is primarily associated with intense weathering under certain climate conditions that promote or facilitate the breakdown of the parent material through weathering and leaching. The climatic conditions favourable for laterite formation (laterisation) are high temperatures, alternating wet and dry seasons, and heavy rainfall during the wet season. These conditions are mostly found in tropical

and subtropical climates, which explains why the majority of the world's laterite deposits are located within these regions. The high temperatures and heavy rainfall directly accelerate chemical reactions and the dissolution and leaching of minerals, while seasonal variations facilitate the precipitation and accumulation of sesquioxides [37,38].

Under conditions conducive to laterisation, most parent material undergoes a process of decomposition facilitated by both weathering and leaching processes, resulting in the formation of laterite. The process generally begins with the infiltration of rainwater through the parent material carrying dissolved gases such as oxygen and carbon dioxide, along with organic acids. These agents initiate chemical reactions, including ion exchange, oxidation, hydrolysis, and reduction, collectively known as chemical weathering, resulting in the fragmentation or disintegration of the parent material (bedrock) into small fractions.

It should be noted that chemical weathering is often accompanied by physical or mechanical weathering due to daily or seasonal temperature fluctuations and erosional forces [38]. Further weathering of the disintegrated particles leads to decomposition of the constituent minerals of the parent material and the formation of secondary minerals and, simultaneously, the washing away of soluble compounds by leaching.

The leaching process, which removes alkali and alkaline earth metals as well as soluble silica from the parent material, leaves behind a residue enriched in less soluble compounds, notably iron and aluminium. The alternating wet and dry seasons promote the precipitation and accumulation of sesquioxides, particularly iron and aluminium oxides, in the upper layers of the soil profile. This phenomenon contributes significantly to the distinctive characteristics and composition of laterite soil or residual weathered soils, commonly referred to as laterite.

2.3.3 Characteristics and Composition of Laterite

Laterite, a highly weathered material developed under tropical conditions, exhibits a wide range of characteristics and composition influenced by the constituent minerals of the parent material, prevailing climate and drainage conditions of the soil, as well as the degree of weathering [35].

The colour spectrum of laterite, typically ranging from red to reddish-brown to yellow, is primarily determined by its chemical composition, which depends on the type of iron oxides present, drainage conditions, and prevailing climate. The red colour is associated with high hematite content, favoured under drier conditions, while yellowish hues are attributed to high goethite levels resulting from the hydration or rehydration of hematite due to alternating wet

and dry seasons. Under saturated conditions, such as below the groundwater table, hematite undergoes reduction through microbial activity, forming ferrous oxide (FeO) and sometimes magnetite (Fe_3O_4), resulting in a black to dark-brown colour.

Besides being rich in sesquioxide minerals of iron and aluminium, laterite may contain anatase, quartz, and kaolinite, as well as trace elements of nickel and manganese. However, the composition of laterite not only varies according to the parent material, drainage conditions, and prevailing climate but also with wet and dry seasons. For instance, under dry conditions, gibbsite and goethite may dehydrate to form boehmite and hematite, respectively, which revert to their respective hydrates under wet conditions. Also, longer dry periods or drier climates are associated with the formation of hematite, which coincides with high clay content (kaolinite), while extended wet periods lead to the formation of gibbsite through the dissolution and leaching of kaolinite. Despite the variations, the two most common types or variants of laterite in terms of composition are ferruginous and aluminous.

2.3.3.1 Ferruginous laterite

Ferruginous laterite is characterised by high iron oxide content, typically in the form of hematite (Fe_2O_3) and goethite (FeOOH). This variant, often derived from iron-rich parent material, occurs in low-forested regions experiencing high temperatures, moderate to heavy rainfall, and defined dry and wet seasons [43]. Ferruginous laterite often displays a red to reddish-brown colouration due to hematite being the dominant iron oxide present.

2.3.3.2 Aluminous laterite

Aluminous laterite is a type of laterite that contains a high amount of aluminium oxides, usually in the form of gibbsite [$Al(OH)_3$] or boehmite [AlO(OH)], resulting in a white to yellowish-brown colouration. This type of laterite typically forms from aluminium-bearing parent soil in regions with high annual rainfall, longer wet periods, or constantly wet conditions with good drainage and high gradients, often under forested cover. These conditions accelerate the decomposition of kaolinite into quartz and gibbsite and also favour the leaching or removal of quartz. Aluminous laterites can be referred to as gibbsite-rich laterite, lateritic bauxite, or simply bauxite. However, gibbsite-rich laterite specifically refers to laterite in which gibbsite is the most dominant mineral, while the term bauxite is exclusively used for laterite containing a substantial amount of aluminium oxide (alumina), usually above 46% [43]. High gibbsite content in laterite generally coincides with goethite, while high boehmite coexists with hematite.

It should be noted that both ferruginous and aluminous laterite can originate from the same parent material or rock. However, the type of laterite that forms is ultimately determined by factors such as climate patterns, drainage conditions, and slope gradient. Additionally, it is worth noting that, apart from the overlying soil or overburden, which is not considered part of lateritic profiles in pedology, laterite is generally characterised as soil low in humus due to high temperatures that limit bacterial activity [39].

2.3.4 Variations in Lateritic Profiles

Lateritic profile refers to the vertical arrangement of soil layers or horizons formed during laterite formation. These layers generally exhibit distinct characteristics and vary in composition, colour, and particle sizes, reflecting the evolutionary stages of the laterite formation processes. Typically, a lateritic profile comprises several layers, with the uppermost layer well-drained, rich in sesquioxides, and poor in kaolinite, while the base layer is composed entirely of the unaltered parent material or bedrock. The intermediate layers generally show varying degrees of weathering, transitioning from fragmented bedrock closer to the base, to the clay, and then nodular-like structures of the sesquioxides-enriched zone. The lower portion of the profile, particularly above the ground water table, tends to be enriched with clay minerals and is associated with poor drainage conditions.

The drainage conditions of the top layer allow for the washing away of clay particles, resulting in low kaolinite concentration and the accumulation of iron and aluminium oxides. This enrichment or accumulation is attributed to the well-drained condition of the top layer. The accumulation of these oxides in the upper layer of the lateritic profile is also attributed to the fluctuating groundwater table due to the alternating wet and dry seasons. The upward movement of water within the soil profile causes dissolved iron and aluminium ions to migrate upwards, leading to precipitation and accumulation of iron and aluminium oxides in the upper layer of the profile.

2.4 Laterite in Geopolymerisation: Research Trends and Findings

Laterite, a naturally occurring soil rich in iron and aluminium oxides, has attracted significant attention from researchers due to its potential as a source of aluminosilicates in geopolymerisation. The readily available nature of laterite has contributed to this growing interest. Another contributing factor is the possibility of iron (Fe), which is usually present in substantial amounts in laterite, to substitute aluminium (Al) in the geopolymeric network, similar to its behaviour in kaolinite and other clay minerals under geological conditions [44,45].

However, there is an ongoing debate regarding the likelihood of this substitution, with some studies suggesting the nonparticipation of iron in the geopolymerisation reaction [46,47], while others express disagreement over the necessary state of iron (Fe^{2+} or Fe^{3+}) that should be present for incorporation [48–50].

Although the concept of stabilising lateritic soils through chemical activation using lime, alkalis, or pozzolans is not new, its application within the context of geopolymerisation or the development of inorganic polymers is relatively novel. Research on the use of laterite in geopolymerisation has primarily been focused on cement-based applications. However, very few studies have explored the potential of laterite-based geopolymer in other applications, such as wastewater treatment [51,52].

Despite the existence of a significant volume of research on laterite as a source of aluminosilicates in geopolymerisation and previous investigations suggesting that alkali-activated laterite or laterite-based geopolymer is suitable for construction purposes, there are still gaps in understanding, particularly regarding the variability of laterite. Laterite varies greatly in composition and characteristics according to location as well as in depth within a given lateritic profile. Yet, many studies have focused on either iron-rich or kaolin-rich laterite, with some considered derivative and offering limited new insights. Therefore, the below review on laterite as a source of aluminosilicates captures only seminal studies on lateritic materials sourced from the tropical and subtropical regions, in adherence to the adopted definition of laterite in Section 2.3.1. It is worth noting that the laterites used in the reviewed studies were calcinated unless stated otherwise.

Obonyo et al. [44] investigated the suitability of utilising laterite as a solid precursor in geopolymerisation. In this study, portions of the laterite ranging from 15 to 35% by weight were calcined at 700 ˚C to serve as nucleation sites for the geopolymerisation. The authors considered two types of laterite: one sample rich in kaolinite and low in iron oxide, while the other was rich in iron oxide and low in kaolinite. They examined the final product in terms of stability in water, biaxial flexural strength, pore size distribution, and phase composition. Obonyo et al.'s findings revealed that the final product exhibited excellent stability in water, low porosity, and water absorption, as well as flexural strength comparable to conventional concrete. However, the authors observed notable differences between the two types of laterite samples. The high-kaolinite laterite displayed higher strength and more zeolitic phases than the iron oxide-rich laterite sample.

Lamougna et al. [53] examined the influence of curing temperatures and the amount of sodium hydroxide (NaOH), the sole activator, on the compressive strength of geopolymer derived from lateritic clay containing kaolinite as the dominant mineral (approximately 50%). The authors observed that both the curing temperature and alkali concentration influenced the strength development and reported 450 ˚C and 8.5 M NaOH as the optimum curing temperature and alkali concentration, respectively. Also, studying the potential of utilising laterite as a raw material in geopolymerisation, Gualtieri et al. [54] studied the mechanical and microstructural properties of phosphoric acid-activation and sodium silicate alkali-activation of laterite-based geopolymer. The laterite investigated contained 41.3% quartz, 36.0% kaolinite, and 15.8% and 6.3% of goethite and hematite, respectively. The authors found that the laterite-based geopolymer activated with phosphoric acid produced better mechanical properties and low porosity than the sodium silicate activation.

Lamougna et al. [55] also investigated the effects of replacing laterite with slag and calcium carbonate (calcite) on the development of laterite-based inorganic polymer. The replacement level ranges from 5 to 50% and 2 to 20% for the slag and calcite, respectively. The laterite examined contained 24.33% of Fe_2O_3 and 24.54% of Al_2O_3. The authors reported that calcite had little influence, while replacing laterite with 20% or more slag significantly improved compressive strength and bulk density, reduced porosity, and resulted in a denser microstructure. Lamougna et al. attributed the poor performance of calcite to its nonparticipation and the subsequent absence of C-A-S-H in the system.

Studying the influence of calcination temperature on fully indurated two iron-rich laterites with similar mineralogical content, Kaze et al. [56] examined water absorption, flexural strengths and the microstructure of laterite-based geopolymer paste. The authors reported 500 ˚C as the optimum calcination temperature for both laterites in terms of flexural strength and dense microstructure. However, the resistance to water absorption was observed to increase as the calcination temperature increased. Still concerned with the performance of geopolymer derived from the two iron-rich laterites, Kaze et al. [57] investigated the flexural strength, water absorption, porosity and microstructure of laterite-based geopolymer containing rice husk ash (RHA) at 10 – 40% replacement level, cured at room temperature and 90 ˚C. The authors reported significant improvement in the mechanical properties and microstructure of the laterite-based geopolymer containing RHA at higher replacement levels and cured at elevated temperature (90 ˚C).

Similarly, Kaze et al. [58] investigated the effect of silicate modulus with varying NaOH concentration on the setting times, compressive strength and microstructural properties of laterite-based geopolymer cured at room temperature. The geopolymer was derived from two iron-rich laterites, as in the previous studies. The authors reported that the laterite-based geopolymer paste produced from the activating solution of 0.75 silicate modulus and 12 M of NaOH obtained the highest compressive strength, the lowest water absorption and exhibited the densest microstructure.

Boum et al. [59] investigated the influence of uncalcined aluminous laterite (bauxite) as a secondary precursor on the properties and performance of geopolymer derived from metakaolin. The bauxite contained 57.4% Al_2O_3, 31.5% SiO_2 and 6.52% Fe_2O_3 and replaced up to 50 % of the metakaolin. The author examined the derived geopolymer in terms of setting times, compressive strength, water absorption and thermal shrinkage (up to 1200 ˚C). Boum et al. reveal that increasing the bauxite content was found to increase setting time and reduce the compressive strength of samples cured at 28 ˚C, attributed to the slow dissolution of the bauxite. However, the sample cure at 28 ˚C did display a decrease in water absorption and a compact microstructure up to 20% replacement level. Curing at higher temperatures did increase compressive strength and reduce thermal shrinkage only from 30% replacement level, but also increased water absorption and induced more cracks in the microstructure.

Tchadjié et al. [60] used mechanically activated bauxite (uncalcined) with varying fineness to supplement alumina in the formation of geopolymer derived from volcanic ash. The uncalcined bauxite replaced 5 – 25% of the volcanic ash, which was deficient in alumina, and the mixtures were activated with sodium hydroxide and sodium silicate. The authors reported that the bauxite with high fineness (1000 – 1730 m2/kg) improved compressive strength, reduced water absorption, and densified the microstructure of the volcanic ash geopolymer, with 15% replacement level being identified as the optimal. Tchadjié et al. also noted that a high amount of alumina in the system negatively affected the geopolymer.

Tchakouté et al. [61] also investigated the influence of calcined bauxite as a secondary precursor on the properties of metakaolin- and laterite-based geopolymers activated with phosphoric acid. The bauxite was calcined at 600 ˚C and replaced up to 20% of the metakaolin and laterite, respectively. According to the authors, increasing the content of calcined bauxite increased the compressive strength and densified the microstructure of the geopolymer derived from metakaolin and laterite, respectively.

Investigating the influence of calcination on the properties of geopolymer derived from low-iron lateritic material, Ghani et al. [62] synthesised geopolymer form material calcinated at 500, 700 and 900 ˚C. The material investigated was a lateritic material poor in iron but rich in silica (63.92%). The author also added commercial aluminium hydroxide (analytical grade) to supplement the alumina content of the material. The synthesised low-iron lateritic clay was cured at 60 ˚C for six days and examined in terms of compressive strength, water absorption and phase composition. Ghani et al. reported that the samples made from the lateritic material calcined at 900 ˚C displayed the best performance in terms of compressive strength, water absorption, and stability in chloride solution, as well as the highest reactivity.

Kaze et al. [63] also studied the effects of laterite chemical composition and activator type on the rheology and performance of laterite-based geopolymers. In this study, the authors considered an iron-rich laterite and a lateritic clay (higher clay content). The lateritic materials were calcined at 600 ˚Celsius for 4 hours and activated with phosphoric acid and alkaline activators. The author reported that both the mineralogy composition and activator type influence the properties of the geopolymer. The phosphoric acid was found to improve flowability but prolong the setting time and display slow strength development. However, the acid-activated samples did achieve the highest 28-day compressive strength and the lowest water absorption and porosity, irrespective of the laterite type.

As presented above, the current research on the use of laterite geopolymerisation in cement-based applications has predominantly focused on iron-rich and kaolinite-rich laterites. To date, however, no study has extensively explored the use of aluminous laterite as the sole or primary precursor, despite its widespread availability and accessibility. Nevertheless, a few studies have attempted to examine the potential of utilising aluminous laterite (bauxite) as a supplementary source of alumina (secondary precursor), with one study reaching up to 50% replacement. Results from these investigations indicate that the inclusion of aluminous laterite significantly improves the performance of geopolymers, albeit within certain limits of replacement.

2.5 Summary

In summary, this chapter reviewed geopolymers, covering definition, historical development, mechanism of geopolymerisation, and factors influencing performance. This was followed by reviews on laterite as a geological material and source of aluminosilicates in geopolymerisation, respectively. The review on laterite as a geological material highlighted the diverse characteristics and composition of laterite with respect to location, environmental conditions,

and even in depth within a given lateritic profile. On the other hand, the review on laterite as a source of aluminosilicates in geopolymerisation highlighted the limited scope of research on aluminium-rich laterite in geopolymerisation, as well as the need for further investigations into its potential as the sole precursor in geopolymerisation.

2.6 References

1. Davidovits, J., Geopolymers: Inorganic Polymeric New Materials, *Journal of Thermal Analysis and Calorimetry*. (2005) **37** 1633–1656.
2. Pacheco-Torgal, F., Castro-Gomes, J., Jalali, S., Alkali-Activated Binders: A Review: Part 1. Historical Background, Terminology, Reaction Mechanisms and Hydration Products, *Construction and Building Materials*. (2008) **22** 1305–1314.
3. Palomo, A., Krivenko, P., Garcia-Lodeiro, I., Kavalerova, E., Maltseva, O., Fernández-Jiménez, A., A Review on Alkaline Activation: New Analytical Perspectives, *Materiales de Construcción*. (2014) **64** e022.
4. Cao, D., Su, D., Lu, B., Yang, Y., Synthesis and Structure Characterisation of Geopolymeric Material Based on Metakaolinite and Phosphoric Acid, *Guisuanyan Xuebao(Journal of the Chinese Ceramic Society)*. (2005).
5. Louati, S., Baklouti, S., Samet, B., Geopolymers Based on Phosphoric Acid and Illito-Kaolinitic Clay, *Advances in Materials Science and Engineering*. (2016) **2016** e2359759.
6. Provis, J.L., Immobilisation of Toxic Wastes in Geopolymers, In: J.L. Provis, J.S.J. van Deventer (Editors), *Geopolymers*, Woodhead Publishing, (2009): pp. 421–440.
7. Lancellotti, I., Barbieri, L., Leonelli, C., Use of Alkali-Activated Concrete Binders for Toxic Waste Immobilization, In: F. Pacheco-Torgal, J.A. Labrincha, C. Leonelli, A. Palomo, P. Chindaprasirt (Editors), *Handbook of Alkali-Activated Cements, Mortars and Concretes*, Woodhead Publishing, Oxford, (2015): pp. 539–554.
8. Davidovits, J., Geopolymer Chemistry and Sustainable Development. The Poly (Sialate) Terminology: A Very Useful and Simple Model, In: *The International Workshop on Geopolymer Cements and Concrete for the Promotion and Understanding of Green-Chemistry, Australia*, (2005): pp. 2278–0181.
9. Davidovits, J., Introduction, In: *Geopolymer Chemistry and Applications*, 5th edition, (2020).
10. Glukhovsky, V.D., Ancient, Modern and Future Concretes, In: *Proceedings of the First International Conference on Alkaline Cements and Concretes*, Kiev, Ukraine, (1994): pp. 1–8.

11. Shi, C., Roy, D., Krivenko, P., Introduction, In: *Alkali-Activated Cements and Concretes*, CRC Press, (2003).
12. Provis, J.L., Introduction and Scope, In: J.L. Provis, J.S.J. van Deventer (Editors), *Alkali Activated Materials: State-of-the-Art Report, RILEM TC 224-AAM*, Springer Netherlands, Dordrecht, (2014): pp. 1–9.
13. Provis, J.L., Deventer, J.S.J. van, Introduction and Scope, In: *Alkali Activated Materials: State-of-the-Art Report, RILEM TC 224-AAM*, Springer Science & Business Media, (2013).
14. Chassevent, L., Hydraulicity of Slags, *Comptes Rendus*. (1937) **250** 670–672.
15. Provis, J.L., Bernal, S.A., Milestones in the Analysis of Alkali-Activated Binders, *Journal of Sustainable Cement-Based Materials*. (2015) **4** 74–84.
16. Provis, J.L., Duxson, P., Kavalerova, E., Krivenko, P.V., Pan, Z., Puertas, F., van Deventer, J.S.J., Historical Aspects and Overview, In: J.L. Provis, J.S.J. van Deventer (Editors), *Alkali Activated Materials: State-of-the-Art Report, RILEM TC 224-AAM*, Springer Netherlands, Dordrecht, (2014): pp. 11–57.
17. Garcia-Lodeiro, I., Palomo, A., Fernández-Jiménez, A., An Overview of the Chemistry of Alkali-Activated Cement-Based Binders, In: F. Pacheco-Torgal, J.A. Labrincha, C. Leonelli, A. Palomo, P. Chindaprasirt (Editors), *Handbook of Alkali-Activated Cements, Mortars and Concretes*, Woodhead Publishing, Oxford, (2015): pp. 19–47.
18. Duxson, P., Van Deventer, J.S.J., Commercialization of Geopolymers for Construction – Opportunities and Obstacles, In: J.L. Provis, J.S.J. van Deventer (Editors), *Geopolymers*, Woodhead Publishing, (2009): pp. 379–400.
19. van Deventer, J.S.J., Provis, J.L., Duxson, P., Brice, D.G., Chemical Research and Climate Change as Drivers in the Commercial Adoption of Alkali Activated Materials, *Waste and Biomass Valorization*. (2010) **1** 145–155.
20. García-Lodeiro, I., Fernández-Jiménez, A., Palomo, A., Variation in Hybrid Cements over Time. Alkaline Activation of Fly Ash–Portland Cement Blends, *Cement and Concrete Research*. (2013) **52** 112–122.
21. Wang, Y.-S., Alrefaei, Y., Dai, J.-G., Silico-Aluminophosphate and Alkali-Aluminosilicate Geopolymers: A Comparative Review, *Frontiers in Materials*. (2019) **6**.
22. Koloušek, D., Brus, J., Urbanova, M., Andertova, J., Hulinsky, V., Vorel, J., Preparation, Structure and Hydrothermal Stability of Alternative (Sodium Silicate-Free) Geopolymers, *Journal of Materials Science*. (2007) **42** 9267–9275.

23. Feng, D., Provis, J.L., van Deventer, J.S.J., Thermal Activation of Albite for the Synthesis of One-Part Mix Geopolymers, *Journal of the American Ceramic Society*. (2012) **95** 565–572.
24. Buchwald, A., Kaps, C., Hohmann, M., Alkali-Activated Binder and Pozzolan Cement Binder-Compete Binder Reaction or Two Sides of the Same Story, In: *Proceedings of the 11th International Conference on the Chemistry of Cement*, (2003).
25. Fernández-Jiménez, A., Palomo, A., Nanostructure/Microstructure of Fly Ash Geopolymers, In: J.L. Provis, J.S.J. van Deventer (Editors), *Geopolymers*, Woodhead Publishing, (2009): pp. 89–117.
26. Wagh, A.S., Chemically Bonded Phosphate Ceramics - A Novel Class of Geopolymers, In: J.P. Singh (Editor), *Advances in Ceramic Matrix Composites X: Proceedings of the 106th Annual Meeting of The American Ceramic Society, Indianapolis, Indiana, USA 2004*, John Wiley & Sons, (2012).
27. Heah, C.Y., Kamarudin, H., Mustafa Al Bakri, A.M., Bnhussain, M., Luqman, M., Khairul Nizar, I., Ruzaidi, C.M., Liew, Y.M., Study on Solids-to-Liquid and Alkaline Activator Ratios on Kaolin-Based Geopolymers, *Construction and Building Materials*. (2012) **35** 912–922.
28. Yang, K.-H., Song, J.-K., Song, K.-I., Assessment of CO2 Reduction of Alkali-Activated Concrete, *Journal of Cleaner Production*. (2013) **39** 265–272.
29. Xu, H., Van Deventer, J.S.J., The Geopolymerisation of Alumino-Silicate Minerals, *International Journal of Mineral Processing*. (2000) **59** 247–266.
30. Garcia-Lodeiro, I., Palomo, A., Fernández-Jiménez, A., Crucial Insights on the Mix Design of Alkali-Activated Cement-Based Binders, In: F. Pacheco-Torgal, J.A. Labrincha, C. Leonelli, A. Palomo, P. Chindaprasirt (Editors), *Handbook of Alkali-Activated Cements, Mortars and Concretes*, Woodhead Publishing, Oxford, (2015): pp. 49–73.
31. Heah, C.Y., Kamarudin, H., Bakri, A.M.M.A., Binhussain, M., Luqman, M., Nizar, I.K., Ruzaidi, C.M., Liew, Y.M., Effect of Curing Profile on Kaolin-Based Geopolymers, *Physics Procedia*. (2011) **22** 305–311.
32. MacKenzie, K.J.D., Innovative Applications of Inorganic Polymers (Geopolymers), In: F. Pacheco-Torgal, J.A. Labrincha, C. Leonelli, A. Palomo, P. Chindaprasirt (Editors), *Handbook of Alkali-Activated Cements, Mortars and Concretes*, Woodhead Publishing, Oxford, (2015): pp. 777–805.
33. Martin, F.J., Doyne, H.C., Laterite and Lateritic Soils in Sierra Leone, *The Journal of Agricultural Science*. (1927) **17** 530–547.

34. Paton, T.R., Williams, M. a. J., The Concept of Laterite, *Annals of the Association of American Geographers*. (1972) **62** 42–56.
35. Gidigasu, M.D., ed., Introduction, In: *Developments in Geotechnical Engineering*, Elsevier, (1976): pp. 1–11.
36. Tardy, Y., Diversity and Terminology of Lateritic Profiles, In: I.P. Martini, W. Chesworth (Editors), *Developments in Earth Surface Processes*, Elsevier, (1992): pp. 379–405.
37. Persons, B.S., Genesis, In: *Laterite: Genesis, Location, Use*, Springer Science & Business Media, (2012).
38. Gidigasu, M.D., ed., Chapter 3 - Pedogenic Processes of Tropical Weathering and Laterization, In: *Developments in Geotechnical Engineering*, Elsevier, (1976): pp. 35–70.
39. Gidigasu, M.D., ed., Chapter 4 - Environments of Genesis and Evolution of Laterite Soils, In: *Developments in Geotechnical Engineering*, Elsevier, (1976): pp. 71–96.
40. Retallack, G.J., Lateritization and Bauxitization Events, *Economic Geology*. (2010) **105** 655–667.
41. Martin, F.J., Doyne, H.C., Laterite and Lateritic Soil in Sierra Leone, II, *The Journal of Agricultural Science*. (1930) **20** 135–143.
42. Bourman, R.P., Ollier, C.D., A Critique of the Schellmann Definition and Classification of 'Laterite,' *CATENA*. (2002) **47** 117–131.
43. Sherman, G.D., Gibbsite-Rich Soils of the Hawaiian Islands, (1958).
44. Obonyo, E.A., Kamseu, E., Lemougna, P.N., Tchamba, A.B., Melo, U.C., Leonelli, C., A Sustainable Approach for the Geopolymerization of Natural Iron-Rich Aluminosilicate Materials, *Sustainability*. (2014) **6** 5535–5553.
45. Davidovits, J., Davidovits, R., Ferro-Sialate Geopolymers (-Fe-O-Si-O-Al-O-), (2020).
46. Lloyd, R.R., Provis, J.L., van Deventer, J.S.J., Microscopy and Microanalysis of Inorganic Polymer Cements. 1: Remnant Fly Ash Particles, *Journal of Materials Science*. (2009) **44** 608–619.
47. Lloyd, R.R., Provis, J.L., van Deventer, J.S.J., Microscopy and Microanalysis of Inorganic Polymer Cements. 2: The Gel Binder, *Journal of Materials Science*. (2009) **44** 620–631.
48. Wagh, A.S., Jeong, S.Y., Chemically Bonded Phosphate Ceramics: III, Reduction Mechanism and Its Application to Iron Phosphate Ceramics, *Journal of the American Ceramic Society*. (2003) **86** 1850–1855.
49. Lemougna, P.N., MacKenzie, K.J.D., Jameson, G.N.L., Rahier, H., Chinje Melo, U.F., The Role of Iron in the Formation of Inorganic Polymers (Geopolymers) from Volcanic

Ash: A 57Fe Mössbauer Spectroscopy Study, *Journal of Materials Science*. (2013) **48** 5280–5286.

50. Hu, Y., Liang, S., Yang, J., Chen, Y., Ye, N., Ke, Y., Tao, S., Xiao, K., Hu, J., Hou, H., Fan, W., Zhu, S., Zhang, Y., Xiao, B., Role of Fe Species in Geopolymer Synthesized from Alkali-Thermal Pretreated Fe-Rich Bayer Red Mud, *Construction and Building Materials*. (2019) **200** 398–407.
51. Ghani, U., Hussain, S., Noor-ul-Amin, Imtiaz, M., Ali Khan, S., Laterite Clay-Based Geopolymer as a Potential Adsorbent for the Heavy Metals Removal from Aqueous Solutions, *Journal of Saudi Chemical Society*. (2020) **24** 874–884.
52. Duna, L.L., Kaze, C.R., Fekoua, J.N.N., Nzouebet, W.A.L., Kamseu, E., Djocgoue, P.F., Rossignol, S., Leonelli, C., Performances of Laterite-Based Geopolymer Matrice Filters on the Bacteriological Filtration of Contaminated Groundwater and Microstructure, *Journal of Water Process Engineering*. (2023) **53** 103699.
53. Lemougna, P.N., Madi, A.B., Kamseu, E., Melo, U.C., Delplancke, M.-P., Rahier, H., Influence of the Processing Temperature on the Compressive Strength of Na Activated Lateritic Soil for Building Applications, *Construction and Building Materials*. (2014) **65** 60–66.
54. Gualtieri, M.L., Romagnoli, M., Pollastri, S., Gualtieri, A.F., Inorganic Polymers from Laterite Using Activation with Phosphoric Acid and Alkaline Sodium Silicate Solution: Mechanical and Microstructural Properties, *Cement and Concrete Research*. (2015) **67** 259–270.
55. Lemougna, P.N., Wang, K., Tang, Q., Kamseu, E., Billong, N., Melo, U.C., Cui, X., Effect of Slag and Calcium Carbonate Addition on the Development of Geopolymer from Indurated Laterite, *Applied Clay Science*. (2017) **148** 109–117.
56. Kaze, R.C., à Moungam, L.B., Djouka, M.F., Nana, A., Kamseu, E., Melo, U.C., Leonelli, C., The Corrosion of Kaolinite by Iron Minerals and the Effects on Geopolymerization, *Applied Clay Science*. (2017) **138** 48–62.
57. Kaze, R.C., à Moungam, L.M.B., Cannio, M., Rosa, R., Kamseu, E., Melo, U.C., Leonelli, C., Microstructure and Engineering Properties of Fe2O3 (FeO)-Al2O3-SiO2 Based Geopolymer Composites, *Journal of Cleaner Production*. (2018) **199** 849–859.
58. Kaze, C.R., Djobo, J.N.Y., Nana, A., Tchakoute, H.K., Kamseu, E., Melo, U.C., Leonelli, C., Rahier, H., Effect of Silicate Modulus on the Setting, Mechanical Strength and Microstructure of Iron-Rich Aluminosilicate (Laterite) Based-Geopolymer Cured at Room Temperature, *Ceramics International*. (2018) **44** 21442–21450.

59. Boum, R.B.E., Kaze, C.R., Nemaleu, J.G.D., Djaoyang, V.B., Rachel, N.Y., Ninla, P.L., Owono, F.M., Kamseu, E., Thermal Behaviour of Metakaolin–Bauxite Blends Geopolymer: Microstructure and Mechanical Properties, *SN Applied Sciences*. (2020) **2** 1358.
60. Tchadjié, L.N., Ekolu, S.O., Quainoo, H., Tematio, P., Incorporation of Activated Bauxite to Enhance Engineering Properties and Microstructure of Volcanic Ash Geopolymer Mortar Composites, *Journal of Building Engineering*. (2021) **41** 102384.
61. Tchakouté, H.K., Bewa, C.N., Fotio, D., Dieuhou, C.M., Kamseu, E., Rüscher, C.H., Influence of Alumina on the Compressive Strengths and Microstructural Properties of the Acid-Based Geopolymers from Calcined Indurated Laterite and Metakaolin, *Applied Clay Science*. (2021) **209** 106148.
62. Ghani, U., Hussain, S., Noor-ul-Amin, Imtiaz, M., Khan, S.A., Role of Calcination on Geopolymerization of Lateritic Clay by Alkali Treatment, *Journal of Saudi Chemical Society*. (2021) **25** 101198.
63. Kaze, C.R., Lecomte-Nana, G.L., Adesina, A., Nemaleu, J.G.D., Kamseu, E., Chinje Melo, U., Influence of Mineralogy and Activator Type on the Rheology Behaviour and Setting Time of Laterite Based Geopolymer Paste, *Cement and Concrete Composites*. (2022) **126** 104345.

Chapter 3

Materials and Characterisation

3.1 Introduction

This chapter provides a comprehensive overview of the materials employed in the laboratory investigation as well as the procedures used to characterise these materials. The materials employed in the laboratory investigation were aluminium-rich laterite, calcium carbonate, Portland cement and sodium-based alkaline activators. However, since the primary goal of this study was to explore the potential of utilising gibbsite-rich laterite in geopolymerisation, most of this chapter is dedicated to describing the properties and processing procedures of the laterite.

The material characterisations covered physical and chemical properties, which include oxide composition, mineralogical phases, particle size distribution, true density, and surface area. From the chemical characterisations, it was confirmed that the laterite being investigated contained a substantial amount of gibbsite and alumina in terms of mineralogical and oxide compositions, respectively. Consequently, based on composition, this lateritic material can be classified as gibbsite-rich, aluminium-rich, or aluminous laterite.

3.2 Materials

The principal materials considered in this investigation were the aluminous laterite, calcium carbonate ($CaCO_3$), Portland cement and alkaline activators. The aluminous laterite was employed as the primary precursor, while the calcium carbonate and Portland cement were used as secondary precursors. The secondary precursors served as a source of calcium oxide and have been considered to promote setting and hardening of the derived geopolymers at ambient temperature (23 ± 2˚ C) [1–3].

3.2.1 Laterite

The laterite used in this investigation was sourced from Liberia, a tropical region located in West Africa. This material was extracted from the gravel-rich zone (the upper layer) of the lateritic profile, which was located on the outskirts of Monrovia. At the time of extraction, the site was being used as a borrow pit for road construction projects around Monrovia. Figure 3.1

shows a picture of the laterite at the point of extraction. From the sieve analysis of the extracted material, presented in Figure 3.2, this material can be characterised as having predominantly coarser particles, with approximately 60% of its particles falling within the sieve size range of 6.75 and 1.18 mm. From the preliminary characterisations conducted to determine the suitability of the laterite, it was found that this material mainly contains alumina (Al_2O_3), ferric oxide (Fe_2O_3), and silica (SiO_2) totalling 93.46%, which is above the minimum requirement (70%) of major oxide composition for pozzolanic material as prescribed by ASTM C618 [4].



Figure 3.1: Picture of the laterite at the extraction site.

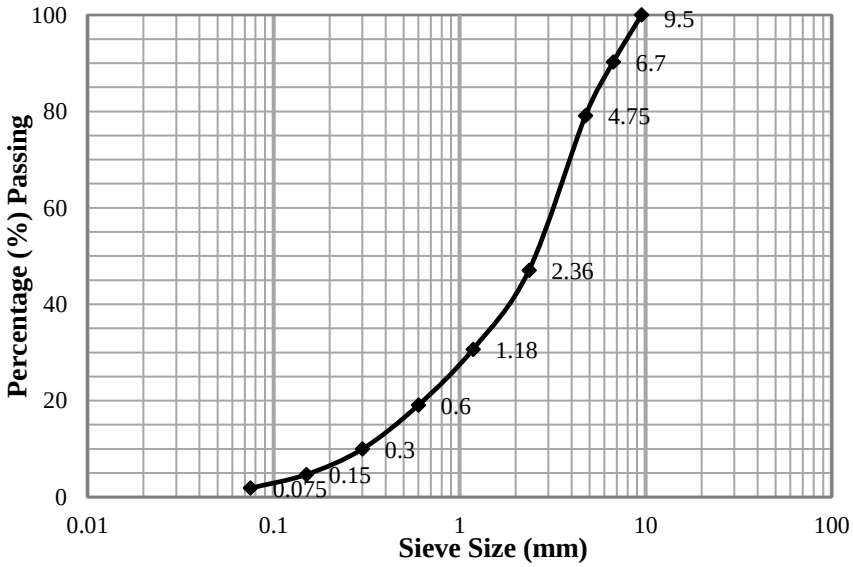

Figure 3.2: Sieve analysis of the extracted laterite.

The portion of the extracted laterite taken for preliminary analyses was first sieved to remove particles larger than 600 μm to obtain a proper representation of the extracted sample. This was

followed by manual crushing using a mortar and pestle to have particles passing the sieve size of 45 µm. The mineralogical and oxide compositions of the extracted material, referred to as 'as-received laterite', were obtained by X-ray diffraction (XRD) and X-ray fluorescence (XRF) and are presented in Figure 3.3 and Table 3.1, respectively. The XRD analysis revealed the presence of gibbsite [$Al(OH)_3$], goethite [$FeO(OH)$], kaolinite [$Al_2Si_2O_5(OH)_4$], and quartz [SiO_2], in amounts of 70.6%, 12.8%, 11.2%, and 5.6%, respectively. It is important to note that the mineralogical composition presented in Figure 3.3 is based on a semi-quantitative analysis.

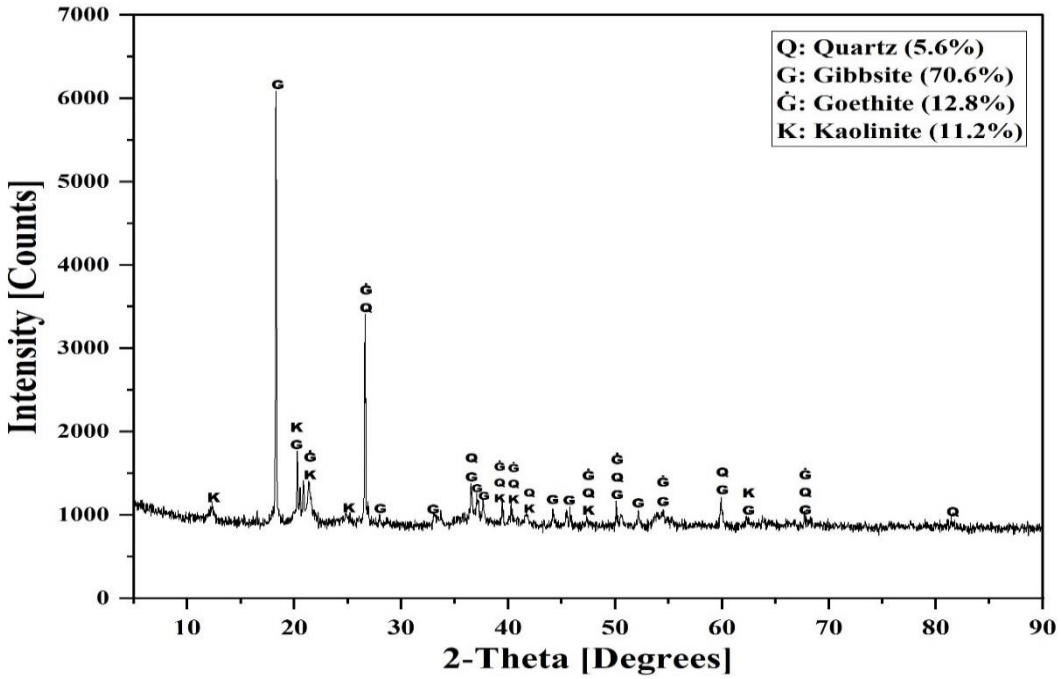

Figure 3.3: XRD spectrum of the as-received laterite.

Table 3.1: Major oxide composition of the as-received laterite.

Material	Oxide Composition (%)								
	SiO_2	Al_2O_3	Fe_2O_3	CaO	MgO	K_2O	Na_2O	TiO_2	SO_3
Laterite (As-received)	29.50	46.10	17.86	0.10	0.17	0.11	0.00	2.00	0.00

Prior to the processing of the laterite, thermal analyses were also conducted on the as-received material as part of the preliminary characterisation. The thermal analysis tests were performed in a nitrogen atmosphere at a heating rate of 10 degrees Celsius (˚C) per minute on a sample size of 10 mg. The resulting thermal analysis curves, which include Thermogravimetric Analysis (TGA), Differential Scanning Calorimetry (DSC), and Differential Thermal Analysis (DTA) curves, are presented in Figure 3.4.

The TGA curve, depicted by the black line, shows four distinct weight loss regions (30 – 200 ˚C, 200 – 380 ˚C, 380 – 550 ˚C, and 550 – 1380 ˚C). The weight loss occurring before 200 ˚C

is attributed to the removal of organic materials or water loosely held on the particle surfaces, while subsequent weight losses beyond this temperature (200 ˚C) can be associated with other thermal events, including dehydroxylation, crystallisation, and melting. The weight loss observed in the temperature range of 200 – 380 ˚C is ascribed to the dehydroxylation of gibbsite [5]. Dehydroxylation is the process in which minerals containing hydroxyl (–OH) groups, such as gibbsite, undergo the removal of the hydroxyl group in the form of water (H_2O) when subjected to heat [6]. This removal is usually accompanied by a discernible weight loss. Therefore, the dehydroxylation of gibbsite involves the transformation of the gibbsite into alumina (Al_2O_3), accompanied by the release of water and a reduction in weight.

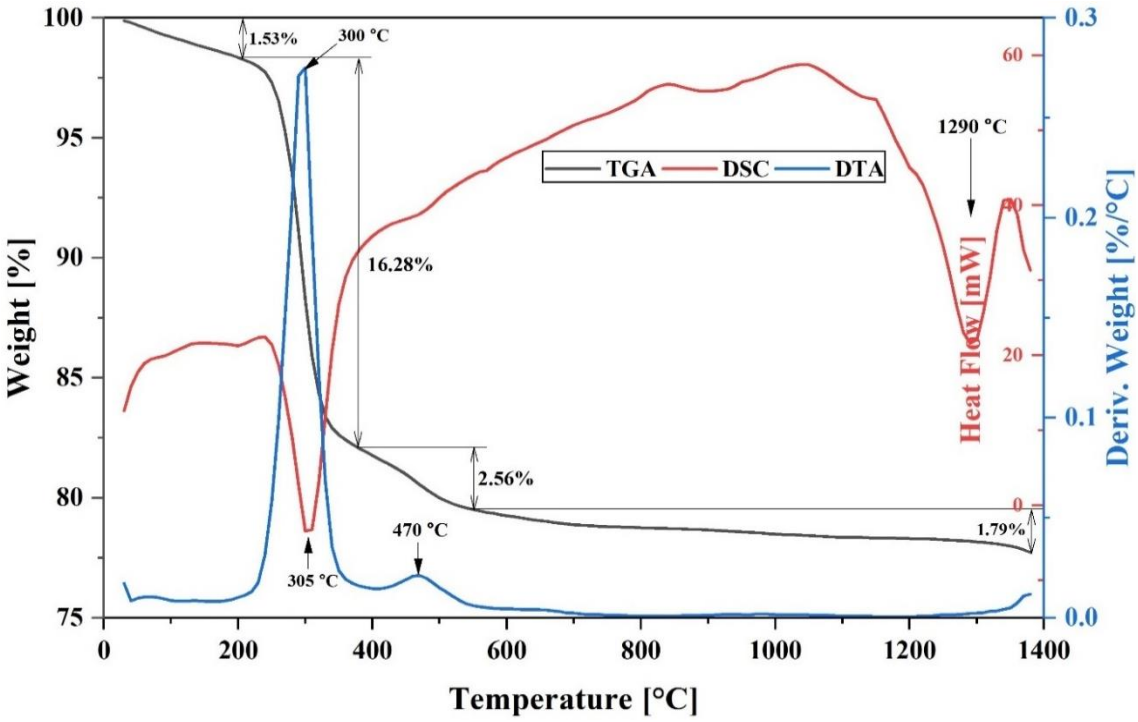

Figure 3.4: Thermograms of the as-received laterite.

In the temperature range of 380 – 550 ˚C, the weight loss corresponds to the dehydroxylation of goethite. The dehydroxylation of goethite typically occurs between 300 – 600 ˚C, converting goethite to hematite (Fe_2O_3) [7,8]. Similarly, within the temperature range of 550 – 800 ˚C, the observed weight loss can be linked to the dehydroxylation of kaolinite. This thermal process, occurring between 500 and 800 ˚C, induces the transformation of kaolinite into metakaolin ($Al_2Si_2O_7$). At temperatures above 900 ˚C, metakaolin undergoes a series of alterations, eventually transforming into mullite, a less reactive and highly stable compound [9,10].

Equations 3.1 to 3.3 illustrate the dehydroxylation reactions for gibbsite, goethite, and kaolinite, respectively. However, the dehydroxylation of gibbsite is usually not as straightforward as

expressed in Equation 3.1. Under dehydroxylation conditions, gibbsite may also transition into an intermediate phase, known as boehmite [AlO(OH)], before the complete removal of water from its structure [11,12].

$$\underset{\text{Gibbsite}}{2Al(OH)_3} \xrightarrow{(200-380^{\circ}C)} \underset{\text{Alumina}}{Al_2O_3} + \underset{\text{Water}}{3H_2O} \qquad \text{Equation – 3.1}$$

$$\underset{\text{Goethite}}{2FeO(OH)} \xrightarrow{(380-550^{\circ}C)} \underset{\text{Hematite}}{Fe_2O_3} + \underset{\text{Water}}{H_2O} \qquad \text{Equation – 3.2}$$

$$\underset{\text{Kaolinite}}{Al_2Si_2O_5(OH)_4} \xrightarrow{(550-800^{\circ}C)} \underset{\text{Metakaolin}}{Al_2O_3{\cdot}2SiO_2} + \underset{\text{Water}}{2H_2O} \qquad \text{Equation – 3.3}$$

It is worth noting that the magnitude of the weight losses along the TGA curve corresponds to the quantity of the respective minerals undergoing dehydroxylation. As depicted in Figure 3.4, the weight losses for the respective temperature ranges are 16.28%, 2.56% and 1,79% for 200 – 380 ˚C, 380 – 550 ˚C, and 550 – 1380 ˚C, respectively, with the maximum occurring in the region attributed to the dehydroxylation of gibbsite. Therefore, from the TGA curve, it can also be confirmed that the as-received laterite is rich in gibbsite mineral and deficient in kaolinite, thereby corroborating the findings of the XRD analysis. Assuming no overlapping thermal footprints, the amount of gibbsite, goethite, and kaolinite in the laterite can also be estimated from the TGA data. This process involves multiplying the weight loss assigned to each mineral by its molecular mass and then dividing by the molecular mass of water [13]. The resulting estimated values are 70.5%, 12.6%, and 10.9% for gibbsite, goethite, and kaolinite, respectively. The weight loss associated with kaolinite in the 550 to 800 ˚C temperature range was 0.76%.

The DTA curve (blue line) displays two prominent exothermic peaks at 300 ˚C and 470 ˚C, corresponding to the dehydroxylation of gibbsite and goethite, respectively. The peak at 300 ˚C is notably sharper and more intense than the one at 470 ˚C, signifying the abundance of gibbsite in comparison to goethite. Also, on the DSC curve (red line), two peaks are clearly visible at 305 ˚C and 1290 ˚C. Interestingly, only the observed peak at 305 ˚C aligns with the TGA weight loss profile associated with the identified minerals. Specifically, this peak corresponds to the dehydroxylation process of gibbsite. However, there is also a less pronounced peak at 470 ˚C, which corresponds to the dehydroxylation reaction of goethite. It should be emphasised that the area under each peak, both in the DSC and DTA curves, is directly proportional to the enthalpy change associated with the dehydroxylation of the gibbsite and goethite, thus further confirming that gibbsite is the dominant mineral in the laterite.

3.2.2 Calcium Carbonate

The calcium carbonate ($CaCO_3$) employed was of analytical grade, with a purity of 98.5%, and was in powder form. This product is commercially available in South Africa. As shown in Figure 3.5, which presents the XRD pattern, this material consisted of only calcite, the purest form of calcium carbonate. Figures 3.6 and 3.7 present the FTIR spectrum and particle micrograph of the calcium carbonate powder, respectively. The transmittance peaks in Figure 3.6 are typical of pure calcite [14,15].

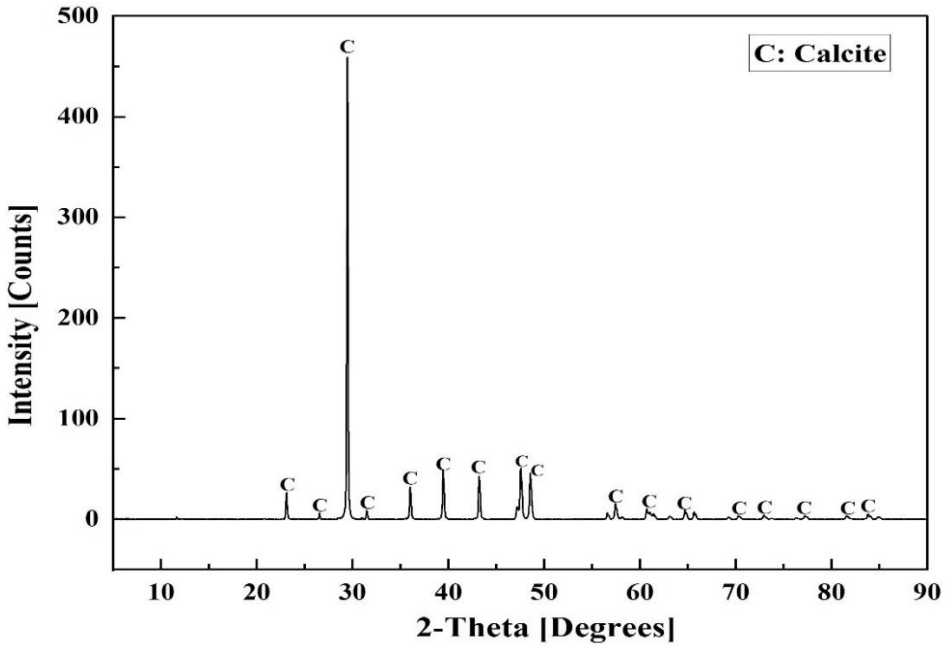

Figure 3.5: XRD spectrum of the calcium carbonate.

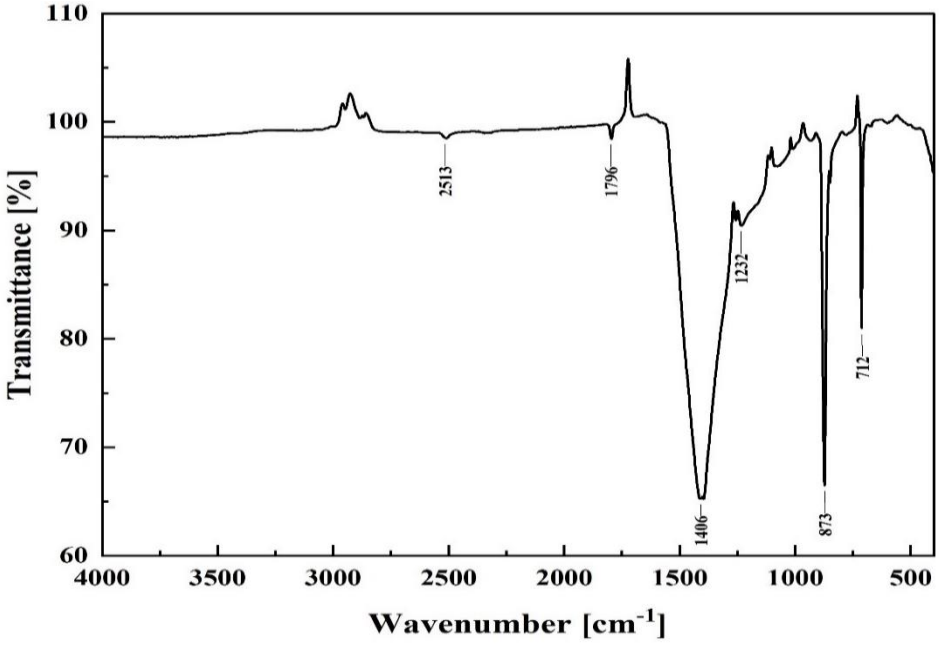

Figure 3.6: FTIR spectrum of the calcium carbonate.

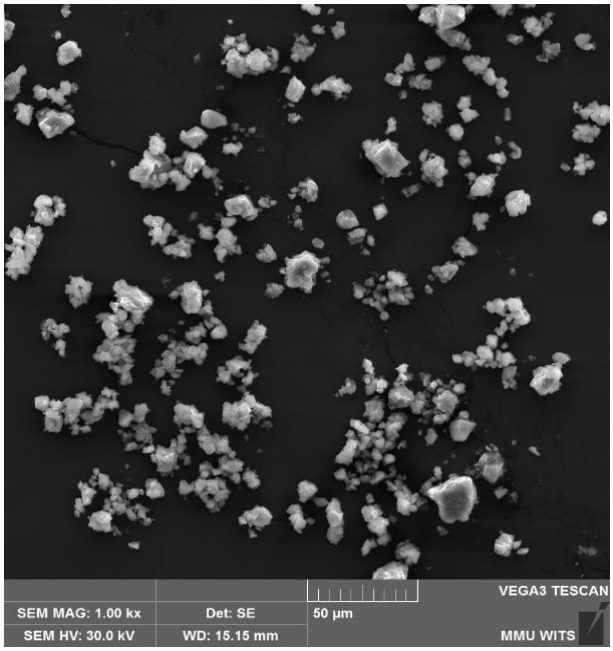

Figure 3.7: Particles micrograph of the calcium carbonate powder.

3.2.3 Portland Cement

A rapid-hardening Portland cement (CEM-I, 52.5R) was used in this investigation. This cement is a commercially available product on the South African market and has a true density and surface area of 3.2 g/cm^3 and 2.22 m^2/g, determined by Helium Pycnometry and the BET method, respectively. Table 3.2 presents the major oxide composition of the rapid-hardening cement, while Figures 3.8 and 3.9, respectively, illustrate the XRD and FTIR spectra. The XRD analysis revealed the presence of alite, belite, aluminate, ferrite, and gypsum. These findings were validated by the FTIR. In the FTIR spectrum, the peaks at 3536 and 3399 cm^{-1} correspond to the vibrations of OH bonds in gypsum [14], while those at 1620, 668, and 600 cm^{-1} relate to the Fe-O bonds in ferrite [14], and 1460 and 713 cm^{-1} correspond to the Al-O bonds in aluminate [16]. The peaks at 1138, 916, 878, 516, and 444 cm^{-1} signify Si-O bonds in alite and belite [16,17]. It is worth noting that the peak at 3642 cm^{-1} on the far left is associated with the OH bonds in portlandite, indicating partial hydration, likely due to exposure to air [17].

Table 3.2: Major oxide composition of Portland cement.

	Oxide Composition (%)								
Material	SiO_2	Al_2O_3	Fe_2O_3	CaO	MgO	K_2O	Na_2O	TiO_2	SO_3
Portland Cement	20.79	4.64	2.69	65.05	1.73	0.47	0.15	0.39	2.99

The particle size distribution curve of the rapid-hardening Portland cement is presented in Figure 3.10 and was obtained using the Anton Paar Particle Size Analyser (PSA 1090), which is based on laser diffraction. The cement has 90% of its particles below 26 µm with an average

particle size of 11 μm. Figure 3.11 presents the SEM micrograph of the cement particles. The incorporation of Portland cement in this study stems from its widespread availability, making it the most accessible and affordable source of calcium oxide in underdeveloped countries, particularly those situated in Africa.

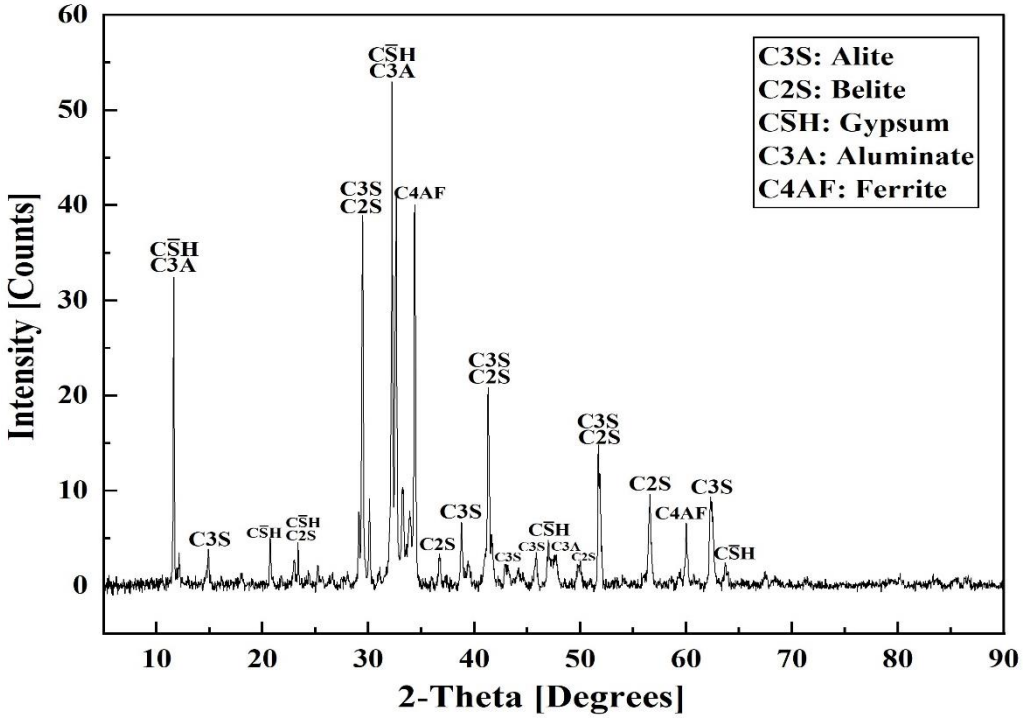

Figure 3.8: XRD spectrum of the Portland cement.

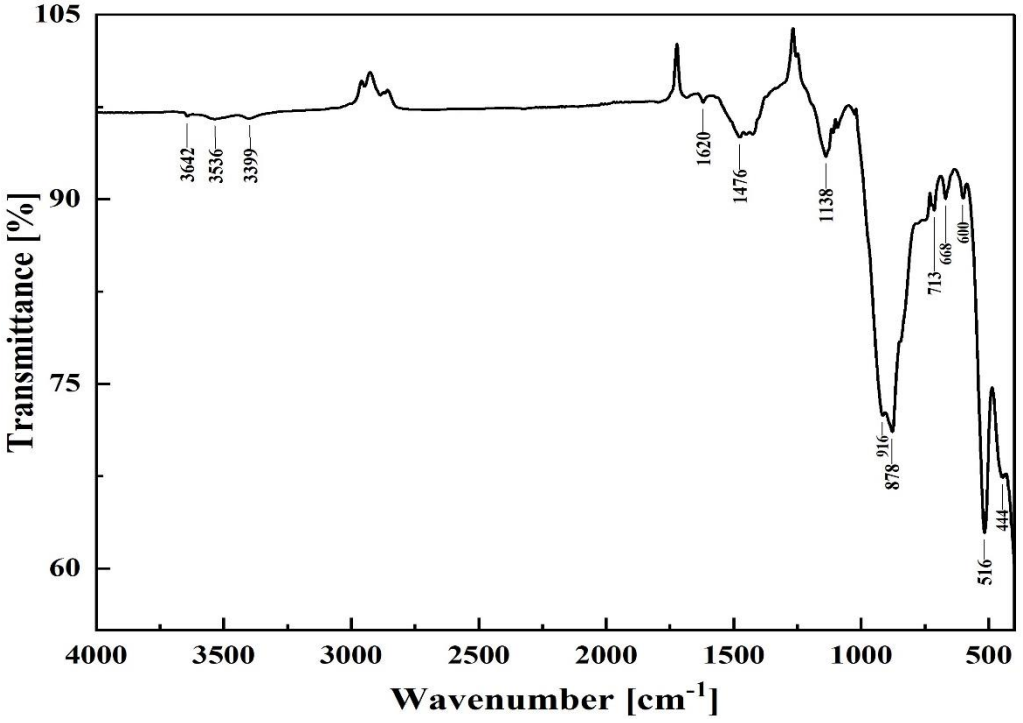

Figure 3.9: FTIR spectrum of the Portland cement.

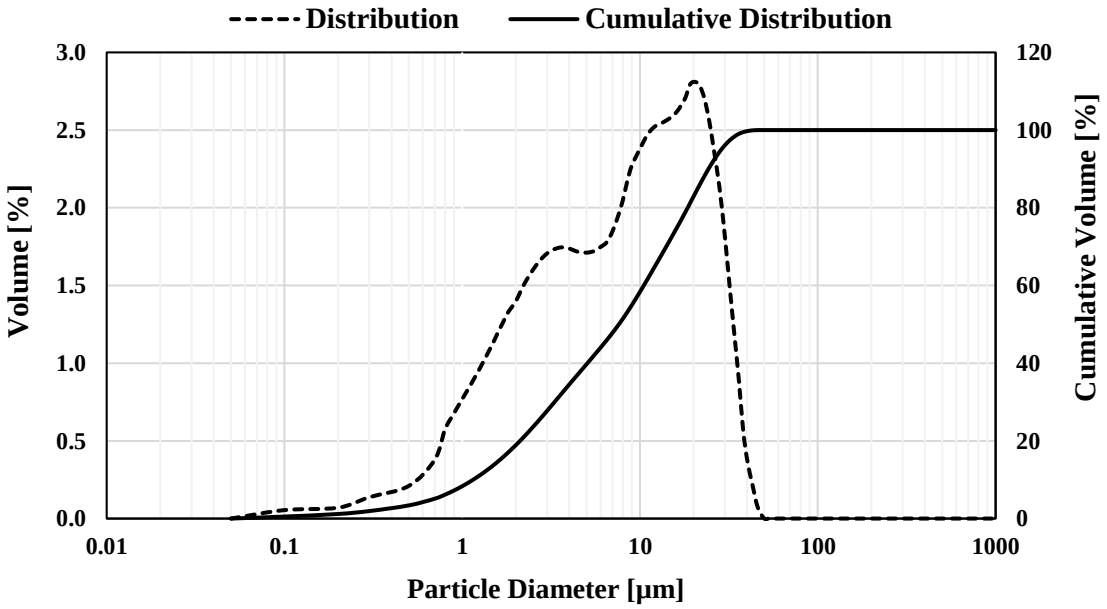

Figure 3.10: Particle size distribution of the Portland cement.

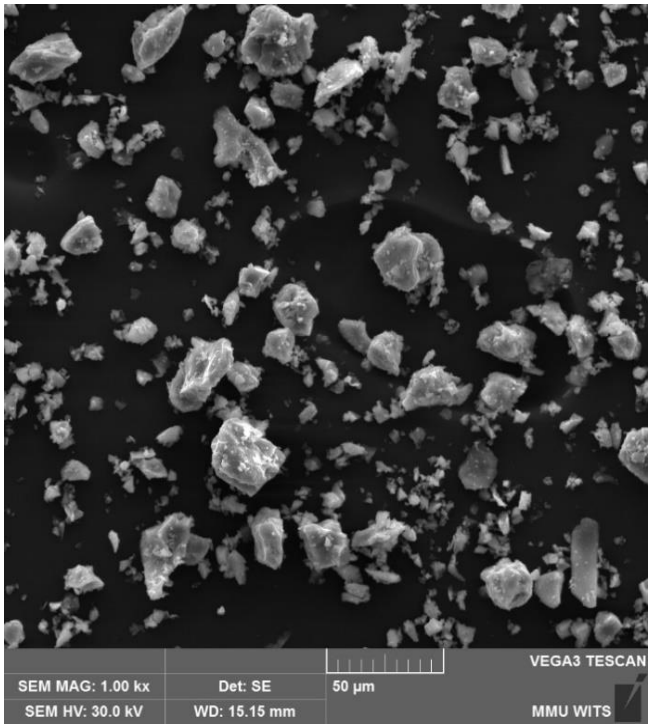

Figure 3.11: Particles micrograph of the Portland cement.

3.2.4 Activators

The selection of activators was based on predefined criteria, which included availability, affordability, and most importantly, the ability to promote ambient temperature (20 ± 3 ˚C) setting. Based on these criteria, four activators, namely sodium carbonate, sodium sulphate, sodium hydroxide and sodium silicate, were initially investigated. The initial assessment of

these activators was based on their ability to promote the demoulding of the specimen within 24 hours after casting. From the preliminary trials, it was found that only the combination of sodium hydroxide and sodium silicate achieved the objective. It was also observed that the sodium hydroxide to sodium silicate ratio of 1:2.5 led to a shorter time to demoulding. As a result, the activators chosen for this experiment were sodium hydroxide and sodium silicate, and were used at a ratio of 1 part sodium hydroxide to 2.5 parts sodium silicate.

3.2.4.1 Sodium Hydroxide

The sodium hydroxide (NaOH) used was of analytic grade in pelletized form and anhydrous state, with a purity of 98.5%.

3.2.4.2 Sodium Silicate

A sodium silicate solution, which had a silica (SiO_2) content of 28.3%, sodium oxide (Na_2O) content of 8.45% and water (H_2O) content of 63.25%, was used in this investigation. However, granulated sodium metasilicate pentahydrate was also part of the preliminary investigation. The granulated sodium metasilicate pentahydrate consisted of 28% Na_2O, 28% SiO_2 and 44% H_2O.

3.2.5 Fine Aggregate

The fine aggregate employed in this research was crushed andesite sand. This material had a fineness modulus of 3.14, a maximum particle size of 4.75 mm, and a true density of 2.83 g/cm^3. The particle size grading curve of the fine aggregate is presented in Figure 3.12.

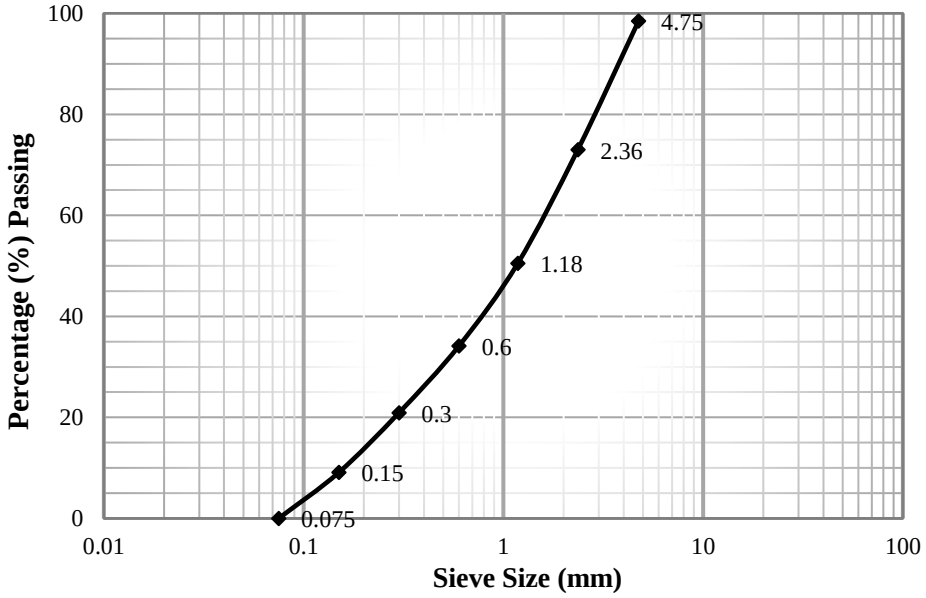

Figure 3.12: Particle size grading curve of the fine aggregate.

3.3 Processing of the Laterite

The processing of the as-received laterite was conducted at laboratory facilities within the School of Civil and Environmental Engineering at the University of the Witwatersrand. The procedure, which consisted of four stages, included drying, pulverising, milling or grinding, and calcination.

Following the preliminary characterisation that established the suitability of the laterite for this investigation, the as-received laterite was spread out to dry under the ambient conditions of the Concrete Laboratory at the School of Civil and Environmental Engineering. The drying process lasted for three days and was carried out to ensure the removal of any surface or absorbed moisture.

After dying, the laterite was first crushed in a pulveriser to reduce the particle size before being further ground using a vibratory disc mill. Figure 3.13 shows the vibratory disc mill employed in the milling process, while Figures 3.14a and 3.14b show the pulverised and ground laterite, respectively. The pulverised laterite was milled to have about 90% of its particles passing the sieve size of 45 μm. During the milling process, a fixed amount of 250 ml of pulverised laterite was placed in the disc pan of the vibratory disc mill and milled for five minutes. This specific quantity and duration were determined through several trials to ensure that approximately 90% of the particles were below 45 μm.

After the milling process, the entire material was homogenised to ensure uniformity. Subsequently, a portion of the milled laterite was then calcinated at a temperature of 750 ˚C for an hour in a programmable electric furnace. The calcination temperature and duration were determined from the thermal analyses conducted on the material (as-received) before processing. This was necessary because it was anticipated that the grinding process might reduce the crystallinity of laterite, potentially causing a shift in thermal reactions, such as the dehydroxylation of constituent minerals, to a lower temperature range [18,19]. As shown in the TGA curve in Figure 3.4, 95% of the weight loss occurred between 30 – 750 ˚C; hence, 750 ˚C was selected as the calcination temperature.

Figures 3.15a and 3.15b illustrate the appearance of the milled laterite, both before and after undergoing calcination at 750 ˚C. The milled laterite before calcination is now referred to as uncalcined laterite.



Figure 3.13: Vibratory disc mill.

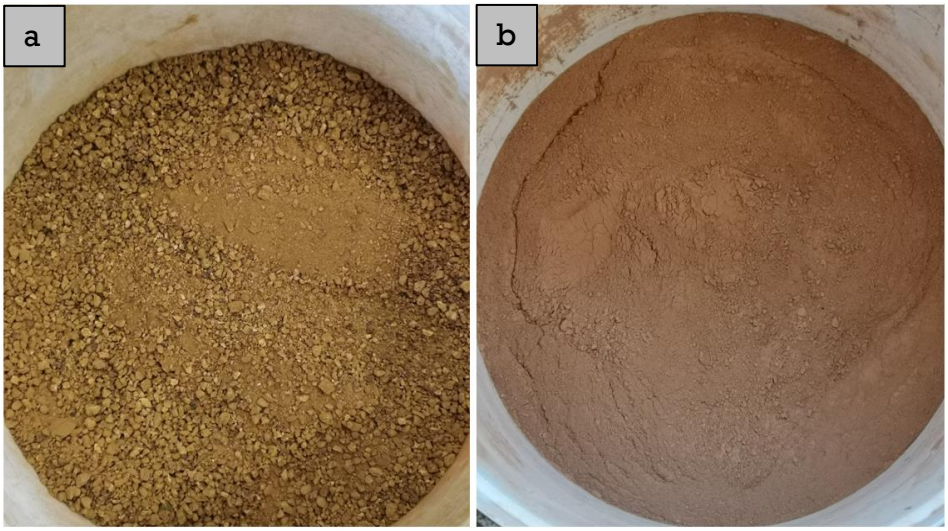

Figure 3.14: (a) Pulverised laterite (b) Milled or ground laterite.



Figure 3.15: (a) Uncalcined laterite (b) Calcined laterite.

3.4 Characterisation of the Laterite

After the calcination process, additional characterisations of both the physical and chemical properties of the uncalcined (milled) and calcined laterite were conducted. These characterisations encompass particle size distribution, surface area, true density, particle micrography, and composition analysis. The composition analysis involved the application of techniques such as XRD for phase identification and thermal analysis for assessing thermal footprints, as well as identifying minerals based on their thermal properties. At this stage of the characterisation, Fourier transform infrared spectroscopy (FTIR) was employed to complement the phase identification process. It is worth noting that FTIR analysis was also performed on the as-received laterite to further examine the impact of milling and calcination on the composition of the laterite. This multifaceted approach aimed to achieve a thorough characterisation of the mineralogical composition of the laterite and importantly, to provide a deeper understanding of how the processing methods, specifically, milling and calcination, influenced the laterite's composition and reactivity.

The true density was determined using a Helium Pycnometer, the particle size distribution by a laser diffraction particle size analyser (PSA 1090), and the surface area by the BET method. Table 3.3 presents data on the surface area and true density of the calcined and uncalcined laterite, as well as the particle size distribution data (D_{90}, D_{50}, D_{10}). The particle size distribution curves and SEM micrographs of particles for both calcined and uncalcined laterite are presented in Figure 3.16 and Figure 3.17, respectively.

The data presented in Table 3.3 and Figures 3.16 and 3.17 reveal noticeable changes in the physical properties of the laterite after calcination. The calcination process led to an increase in true density, a decrease in surface area, and a shift toward larger particle size in the calcined laterite. The increase in particle size can be attributed to the coarsening of particles induced by the calcination process, and this phenomenon generally contributes to a reduction in surface area [20]. However, regarding true density, the increase is most likely due to the removal of hydroxyl groups from the laterite's hydrated minerals during calcination, or due to both dehydroxylation and particle coarsening.

Although there is an overall trend of larger particles in the calcined laterite, there was also a slight shift of the particles toward the finer regions, as shown in the particle size distribution curve (Figure 3.16) and the D_{10} value in Table 3.3. This shift could be attributed to the breakdown or disintegration of larger particles caused by the calcination process.

Table 3.3: Physical properties of the uncalcined and calcined laterite.

	Uncalcined Laterite (UL)	Calcined Laterite (CL)
True Density (g/cm^3)	2.93	3.36
Surface Area (m^2/g)	23.06	20.21
Particle Diameter: Mean (µm)	18.19	23.60
D_{90} (µm)	45.35	61.40
D_{50} (µm)	10.73	12.10
D_{10} (µm)	1.54	1.27

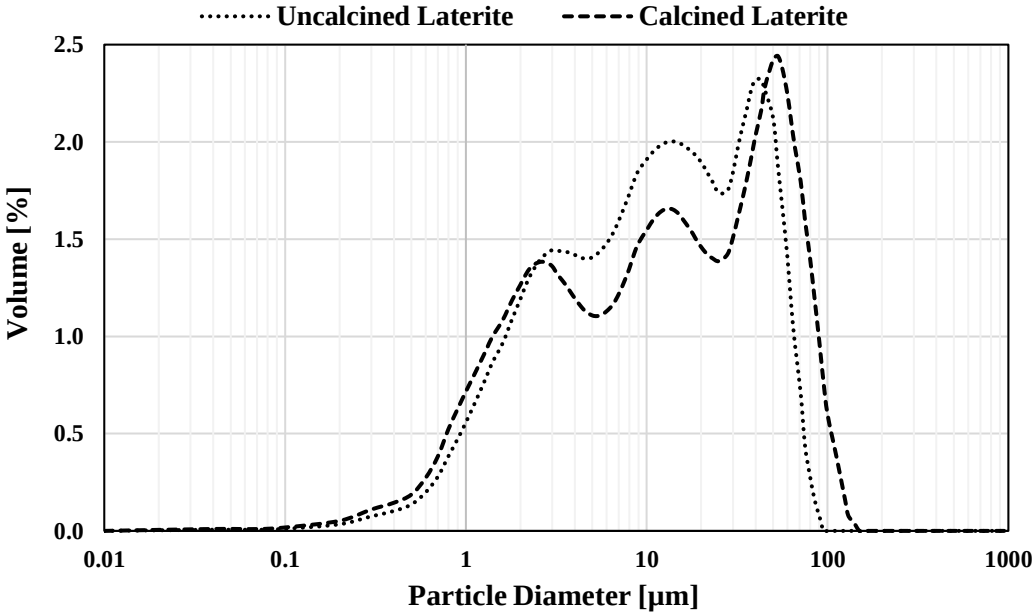

Figure 3.16: Particle size distribution curves of uncalcined and calcined laterite.

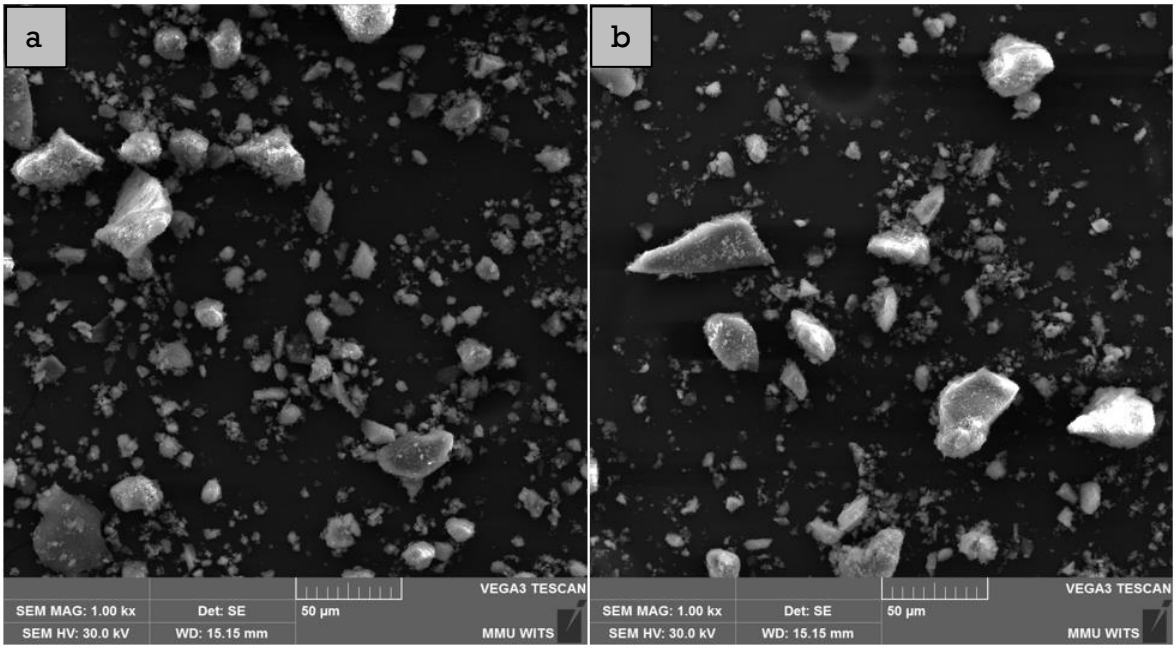

Figure 3.17: SEM particle micrograph: (a) Uncalcined laterite (b) Calcined laterite.

Figure 3.18 displays the XRD spectra for both calcined and uncalcined laterite. The XRD revealed the presence of gibbsite, goethite, and quartz in the uncalcined laterite, while for the calcined laterite, only hematite and quartz were detected. The absence of kaolinite in the uncalcined laterite suggests that the milling process may have altered the crystal structure of the kaolinite, rendering it undetectable by XRD. Hence, it is safe to suggest that the milling process may have led to a reduction in crystallinity of the laterite.

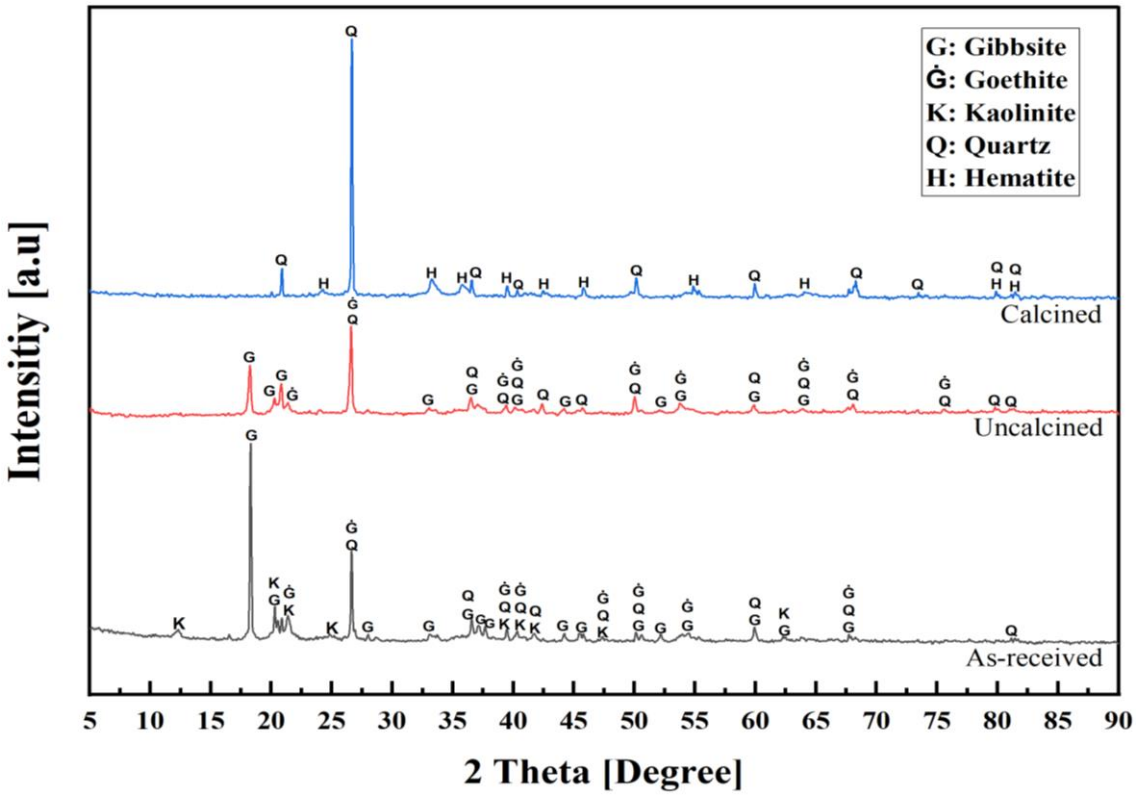

Figure 3.18: XRD spectra of the laterites.

The calcination process also had a profound impact on the chemical composition and crystal structure of the laterite. Notably, this process brought about a substantial alteration in the mineralogical composition by eliminating gibbsite and goethite through dehydroxylation, as described in Section 3.1.1. During the calcination of the laterite, gibbsite and goethite minerals underwent dehydroxylation, resulting in the formation of alumina (Al_2O_3) and hematite (Fe_2O_3), respectively. However, only hematite was detected through the XRD analysis of the calcined laterite, thus suggesting that the alumina must be X-ray amorphous. It is crucial to emphasise that dehydroxylation induces alterations in the crystal structure of materials, leading either to a new crystal structure characterised by reduced order of crystallinity or, alternatively, to the formation of an amorphous phase lacking a well-defined order of crystal structure.

To further examine the impact of the processing procedures on the laterite's crystal structure, the degree of crystallinity, also known as crystallinity, was calculated based on the XRD data. The estimated crystallinity of the laterite is presented in Figure 3.19 and was obtained using Equation 3.4, adapted from Navarro-Pardo et al. [21]. The areas under the peaks along the XRD curve were determined through integration in Origin software. As depicted in Figure 3.19, both the uncalcined and calcined laterite exhibited a lower degree of crystallinity compared to the as-received sample, with the calcined laterite displaying the lowest. This observation implies that both the milling process and calcination contributed to the reduction in crystallinity of the laterite.

$$\text{Crystallinity (\%)} = \frac{Area\ of\ Crystalline\ Peaks}{Area\ of\ all\ Peaks\ (crystalline\ and\ amorphous)} \times 100 \qquad \text{Equation -------3.4}$$

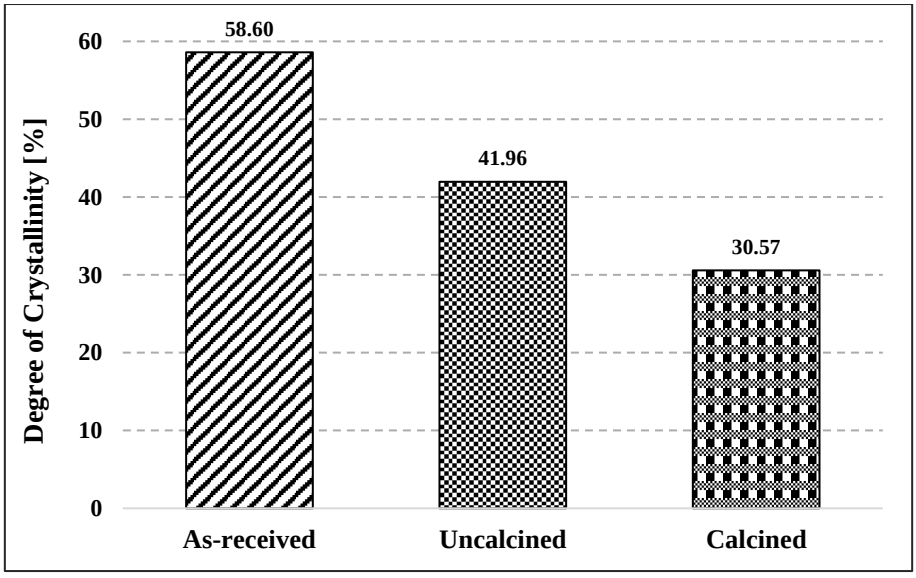

Figure 3.19: Crystallinity of the laterites.

For the thermal analyses of the processed material, the sample size, heating conditions, and testing procedures were consistent with those applied to the as-received material. The sample preparations also involved sieving below 45 μm. Figure 3.20 presents the thermograms of the uncalcined and calcined laterite, along with those of the as-received laterite. Analyses of the results revealed the presence of similar minerals identified in the as-received laterite in the milled laterite (uncalcined), while for the calcined laterite, it was evident that complete dehydroxylation occurred during the calcination process. However, the TGA, DTA, and DSC techniques all reveal that the processing of the laterite not only altered its physical properties but also its chemical structure.

The milling process was found to reduce the amount of heat required to cause the dehydroxylation of gibbsite and goethite minerals. Although the as-received laterite and the uncalcined sample displayed similar TGA and DTA curves, the uncalcined laterite exhibited lower weight loss and dehydroxylation temperatures than the as-received sample. For instance, gibbsite and goethite dehydroxylated at 300 and 470 ˚C, respectively, in the as-received laterite and at 270 and 440 ˚C in the milled (uncalcined) laterite. Also, considering the weight losses in regions (200 – 380 ˚C and 380 – 550 ˚C) assigned to gibbsite and goethite as specified in Section 3.1.1, weight losses of 11.17% and 1.87% were observed in the uncalcined laterite, while in the as-received sample, the corresponding values were 16.28% and 2.56% for gibbsite and goethite, respectively.

Looking closely at the third region (550 – 1380 ˚C) in the uncalcined laterite, an increase in weight loss is observed, from the value of 1.79% in the as-received to 1.94% in the uncalcined laterite. This indicates that more thermal events (phase transformation) are occurring as a result of the reduced particle size, increased surface area, and reduced crystal structure. Another issue worthy of concern in this region is the weight loss associated with the dehydroxylation of kaolinite within the temperature range of 550 to 800 ˚C. In this interval, the corresponding weight losses in the as-received and uncalcined samples are 0.76% and 0.67%, respectively. The marginal disparity between the two raises suspicion about the presence of kaolinite in the uncalcined sample, indicating that the milling process may not have removed the hydroxyl group from the kaolinite structure. Similar findings by Rivas Mercury et al. [22] suggest that milling-induced amorphisation of minerals typically preserves their original water content, despite the distortion of the minerals' crystal structures.

In the calcined laterite, the shapes of the thermographs (TGA, DTA, and DSC curves) are completely different from those of the uncalcined and as-received laterite. The thermographs of the calcined laterite reveal neither the presence of gibbsite, goethite, nor kaolinite, indicating that the selected calcination temperature was the most appropriate. The maximum weight loss in the calcined laterite occurred after 800 ˚C. It is worth highlighting that the maximum weight loss in the calcined laterite corresponds to an endothermic DTA peak at 1110 ˚C and an exothermic DSC peak at 1000 ˚C, suggesting that melting is the dominant thermal event. Unlike the as-received laterite, the entire heat flow (DSC curves) of the uncalcined and calcined laterites appears to be exothermic, indicating more melting compared to the as-received material.

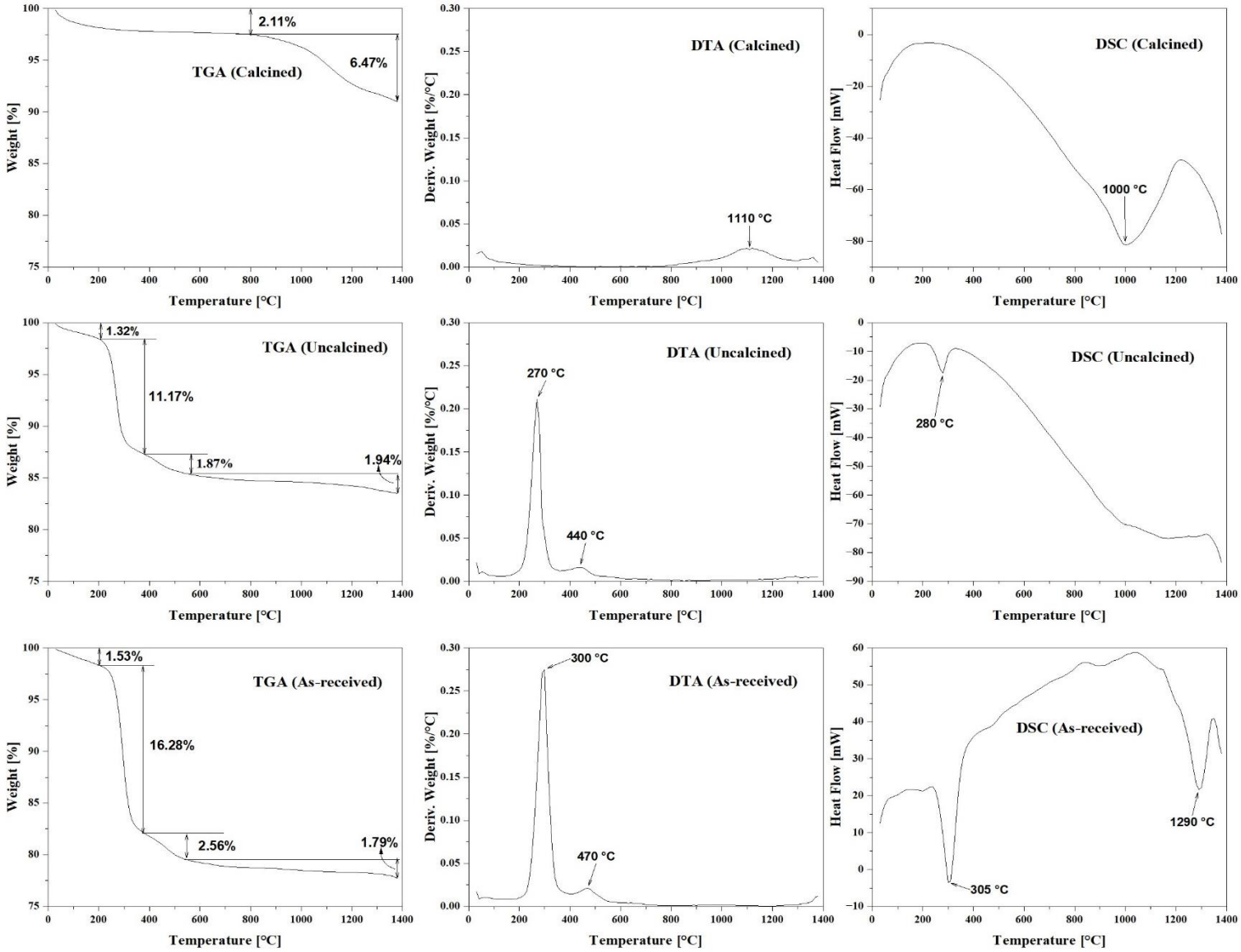

Figure 3.20: Thermograms of the laterites.

The FTIR spectra of the laterites are presented in Figure 3.21 in the form of transmittances, which is the amount of infrared light passed through the sample. Within the functional group region, 1500 – 4000 wavenumber (cm^{-1}), as shown in Figure 3.21, five major transmittance peaks are observed between 3300 – 3700 cm^{-1}, and these peaks are only found in the as-received and uncalcined laterite. These peaks, attributed to stretching vibrations of molecules containing hydroxyl groups, can be assigned to gibbsite, goethite, and kaolinite, thus confirming the presence of these minerals in the laterite. The peak at 3696 cm^{-1} can be identified with the OH group in kaolinite [23], while 3621, 3527, and 3376 cm^{-1} correspond to gibbsite [14,24], and 3447 cm^{-1} to goethite [25]. The calcined laterite displayed no transmittance peaks in the functional group region, which indicates a complete removal of the OH groups via the process of dehydroxylation.

Interestingly, the FTIR analysis clearly revealed that the uncalcined laterite still contained kaolinite mineral. Despite the reduction in crystallinity of the laterite through milling and kaolinite being undetectable in the XRD analysis of the uncalcined sample, the milling process did not remove the hydroxyl group or water molecule from the kaolinite's structure. These findings also provide additional support to the TGA analysis regarding the presence of kaolinite in the uncalcined sample.

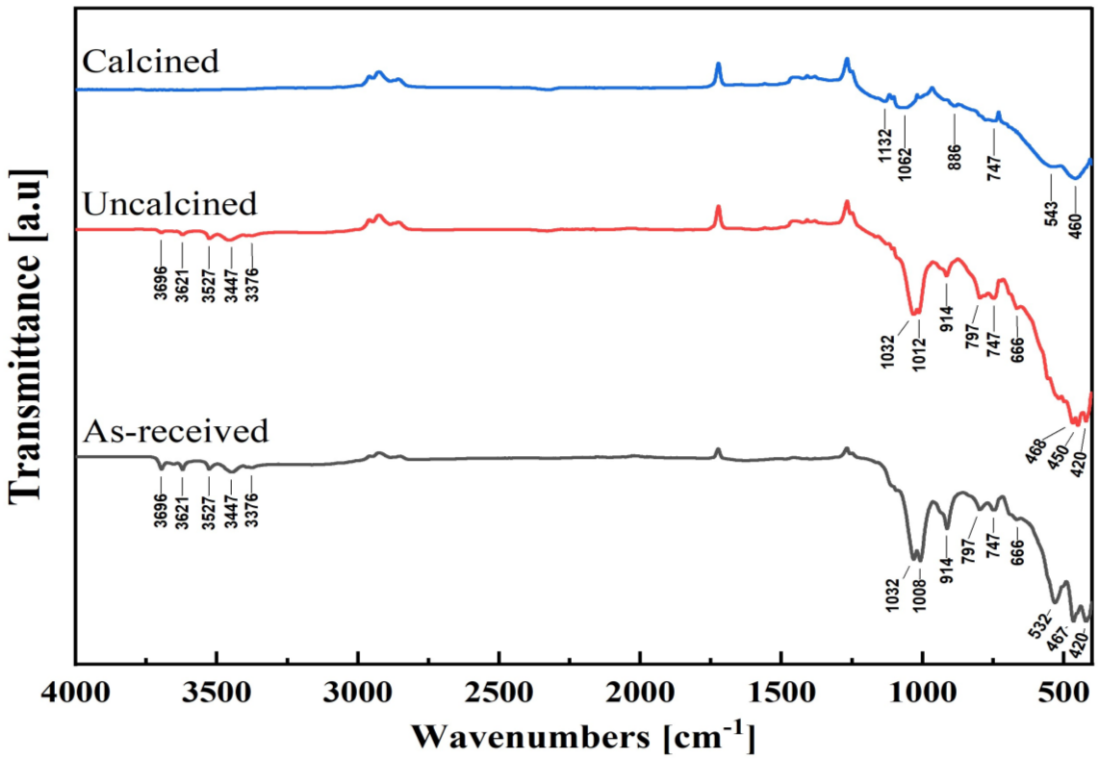

Figure 3.21: FTIR spectra of the laterites.

Moving into the fingerprint region (1500 – 400 cm^{-1}), the peaks observed within this range can be ascribed to the Al-O bonds found in gibbsite and kaolinite, the Fe-O bond in goethite, and the Si-O bonds in kaolinite and quartz. It is worth noting that the peaks in this region may correspond to more than one molecular structures or bonds. Therefore, no attempt will be made to assign the peaks to the respective hydroxyl minerals identified in the functional group region. For instance, the peak at 914 cm^{-1} has been linked to gibbsite, goethite, and kaolinite, while 797 cm^{-1} has also been associated with Fe-O, Si-O, and Si-O-Al bonds, respectively, in goethite, quartz, and kaolinite [14,23].

In the calcined laterite, all the peaks associated with the hydroxyl-group minerals in the as-received and uncalcined samples disappeared upon heating. The peaks in the calcined laterite can be attributed to metakaolin, alumina, hematite, and quartz. The peak at 1062 cm^{-1} is associated with the Si-O-Al bonds in metakaolin, while peaks at 776 and 460 cm^{-1} correspond to the Al-O bonds in both the alumina and metakaolin. Also, the peaks at 886 and 543 cm^{-1} are associated with the Fe-O bonds in hematite, and peaks at 1132 and 747 cm^{-1} can be assigned to the Si-O bonds in quartz.

3.5 Summary

In this chapter, detailed descriptions of the materials used in the laboratory investigation have been presented, accompanied by a discussion on the impact of the processing procedures, particularly milling and calcination, on the properties of laterite. The material characterisation involved methods such as BET, laser diffraction, helium pycnometry, XRD, XRF, TGA, and FTIR to assess both the physical and chemical properties of the laterite and secondary precursors, namely calcium carbonate and Portland cement. Both XRD and TGA confirmed the laterite's composition as gibbsite-rich, affirming its suitability for the study. The milling and calcination processes were found to reduce the crystallinity and alter the mineralogical composition of the laterite. Milling made kaolinite undetectable by XRD, while calcination was observed to completely remove hydroxyl groups from the minerals.

3.6 References

1. Temuujin, J., van Riessen, A., Williams, R., Influence of Calcium Compounds on the Mechanical Properties of Fly Ash Geopolymer Pastes, *Journal of Hazardous Materials*. (2009) **167** 82–88.

2. Khater, H.M., Effect of Calcium on Geopolymerization of Aluminosilicate Wastes, *Journal of Materials in Civil Engineering*. (2012) **24** 92–101.
3. Nath, P., Sarker, P.K., Properties of Fly Ash Based Geopolymer for Curing at Ambient Temperature, In: *In Proceedings of 2012 PCI National Convention and Bridge Conference*, (2012).
4. ASTM C618, Standard Specification for Coal Fly Ash and Raw or Calcined Natural Pozzolan for Use in Concrete, (2013).
5. Kloprogge, J.T., Ruan, H.D., Frost, R.L., Thermal Decomposition of Bauxite Minerals: Infrared Emission Spectroscopy of Gibbsite, Boehmite and Diaspore, *Journal of Materials Science*. (2002) **37** 1121–1129.
6. Ahmari, S., Zhang, L., 13 - The Properties and Durability of Mine Tailings-Based Geopolymeric Masonry Blocks, In: F. Pacheco-Torgal, P.B. Lourenço, J.A. Labrincha, S. Kumar, P. Chindaprasirt (Editors), *Eco-Efficient Masonry Bricks and Blocks*, Woodhead Publishing, Oxford, (2015): pp. 289–309.
7. Rendon, J.L., Serna, C.J., IR Spectra of Powder Hematite: Effects of Particle Size and Shape, *Clay Minerals*. (1981) **16** 375–382.
8. Rabie, M.S., Infrared Study of FeO" OH ~ Fe203 Thermal Transformation, *Journal of Chemical Sciences*. (1986) **96** 315–320.
9. Percival, H.J., Duncan, J.F., Foster, P.K., Interpretation of the Kaolinite-Mullite Reaction Sequence from Infrared Absorption Spectra, *Journal of the American Ceramic Society*. (1974) **57** 57–61.
10. Lee, S., Kim, Y.J., Moon, H.-S., Phase Transformation Sequence from Kaolinite to Mullite Investigated by an Energy-Filtering Transmission Electron Microscope, *Journal of the American Ceramic Society*. (1999) **82** 2841–2848.
11. Perić, J., Krstulović, R., Vučak, M., Investigation of Dehydroxylation of Gibbsite into Boehmite by DSC Analysis, *Journal of Thermal Analysis*. (1996) **46** 1339–1347.
12. Redaoui, D., Sahnoune, F., Heraiz, M., Raghdi, A., Mechanism and Kinetic Parameters of the Thermal Decomposition of Gibbsite Al (OH) $_3$ by Thermogravimetric Analysis, *Acta Physica Polonica A*. (2017) **131** 562–565.
13. Lothenbach, B., Durdzinski, P., De Weerdt, K., Thermogravimetric Analysis, In: *A Practical Guide to Microstructural Analysis of Cementitious Materials*, CRC press Boca Raton, FL, USA, (2016): pp. 177–211.
14. Chukanov, N.V., Infrared spectra of mineral species: Extended library, Springer Science & Business Media, (2013).

15. Vahur, S., Teearu, A., Peets, P., Joosu, L., Leito, I., ATR-FT-IR Spectral Collection of Conservation Materials in the Extended Region of 4000-80 Cm–1, *Analytical and Bioanalytical Chemistry*. (2016) **408** 3373–3379.
16. Ghosh, S.N., IR Spectroscopy, In: *Handbook of Analytical Techniques in Concrete Science and Technology, Principles, Techniques, and Applications*, (2001): pp. 174–200.
17. Kuzielová, E., Slaný, M., Žemlička, M., Másilko, J., Palou, M.T., Phase Composition of Silica Fume—Portland Cement Systems Formed under Hydrothermal Curing Evaluated by FTIR, XRD, and TGA, *Materials*. (2021) **14** 2786.
18. Dellisanti, F., Valdrè, G., Linear Relationship between Thermo-Dehydroxylation and Induced-Strain by Mechanical Processing in Vacuum: The Case of Industrial Kaolinite, Talc and Montmorillonite, *International Journal of Mineral Processing*. (2008) **88** 94–99.
19. Pang, Y., Liu, Y., Zhang, X., Gao, M., Pan, H., Role of Particle Size, Grain Size, Microstrain and Lattice Distortion in Improved Dehydrogenation Properties of the Ball-Milled Mg(AlH4)2, *International Journal of Hydrogen Energy*. (2013) **38** 1460–1468.
20. Schultz, L.N., Dideriksen, K., Lakshtanov, L., Hakim, S.S., Müter, D., Haußer, F., Bechgaard, K., Stipp, S.L.S., From Nanometer Aggregates to Micrometer Crystals: Insight into the Coarsening Mechanism of Calcite, *Crystal Growth & Design*. (2014) **14** 552–558.
21. Navarro-Pardo, F., Martínez-Barrera, G., Martínez-Hernández, A.L., Castaño, V.M., Rivera-Armenta, J.L., Medellín-Rodríguez, F., Velasco-Santos, C., Effects on the Thermo-Mechanical and Crystallinity Properties of Nylon 6,6 Electrospun Fibres Reinforced with One Dimensional (1D) and Two Dimensional (2D) Carbon, *Materials*. (2013) **6** 3494–3513.
22. Rivas Mercury, J.M., Sucupira, J.R.M., Rodríguez, M.A., Cabral, A.A., De Aza, A.H., Pena, P., Influence of the Milling Conditions on the Thermal Decomposition of Bayer Gibbsite, *Powder Technology*. (2020) **362** 188–196.
23. Chukanov, N.V., Chervonnyi, A.D., Infrared Spectroscopy of Minerals and Related Compounds, Springer, (2016).
24. J. Ingram-Jones, V., T. Slade, R.C., W. Davies, T., C. Southern, J., Salvador, S., Dehydroxylation Sequences of Gibbsite and Boehmite: Study of Differences between Soak and Flash Calcination and of Particle-Size Effects, *Journal of Materials Chemistry*. (1996) **6** 73–79.

25. Yusiharni, E., Gilkes, R., Rehydration of Heated Gibbsite, Kaolinite and Goethite: An Assessment of Properties and Environmental Significance, *Applied Clay Science*. (2012) **64** 61–74.

Chapter 4

Experimental Methods and Procedures

4.1 Introduction

This chapter provides comprehensive and sequential descriptions of the experimental procedures and methodologies employed in the laboratory investigation. An overview of each method employed in this study is first presented, outlining the fundamental concepts before delving into the detailed procedures. Also, presented in this chapter are the results of preliminary trials upon which certain decisions were based.

In alignment with the overall research goals, the objectives of the laboratory investigation were:

1. To examine the rheology, setting times and the heat released during the process of geopolymerisation.
2. To investigate the compressive strength development of the geopolymer derived from aluminium-rich laterite.
3. To characterise the product of geopolymerisation and the pore structure of the hardened material derived from aluminium-rich laterite.

Therefore, to achieve these objectives, a series of laboratory examinations involving Vicat apparatus, flow table testing, isothermal calorimetry, compressive strength testing, gas pycnometry and solvent exchange method were employed in this investigation. For the characterisation of the product of geopolymerisation, advanced analytical techniques such as X-ray diffraction and Fourier transform infrared spectroscopy were utilised in this study. It is important to note that, with the exception of the compressive strength test, which was conducted on mortar samples, all other tests were performed on paste samples.

4.2 Overview of the Laboratory Investigation

Figure 4.1 presents the schematic of the laboratory experiment. This schematic provides a clear and concise overview of the experimental processes as well as a visual representation of the scope of the laboratory investigation. The primary focus of the laboratory experiment was to examine the properties of the fresh mix with respect to the flow behaviour, setting times, and

reaction kinetics, and for the hardened properties, compressive strength, pore structure, and phase assemblage.

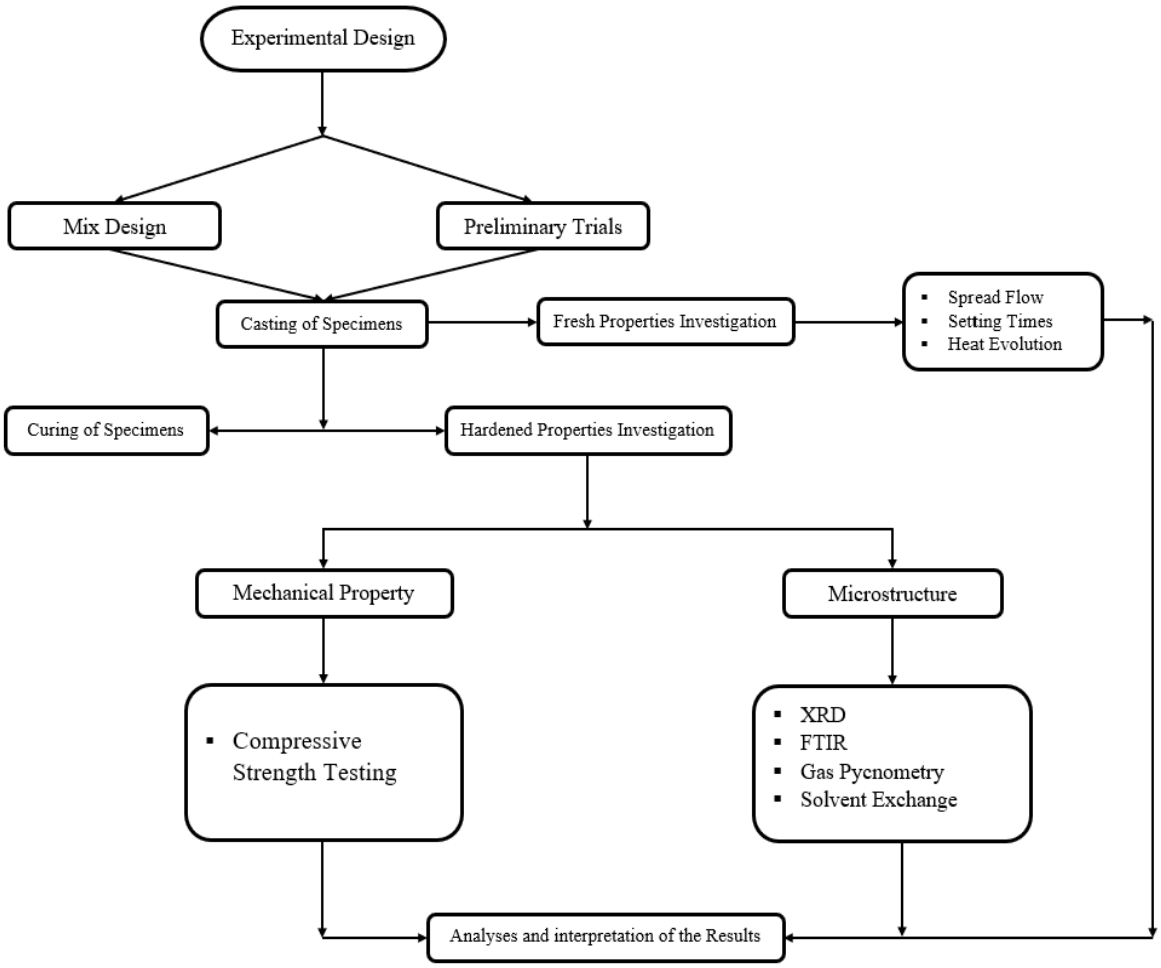

Figure 4.1: Schematic of the laboratory investigation.

4.3 Mix Designs

Three categories of mixes were considered in this investigation, and each category consisted of calcined and uncalcined laterite. These categories comprise pure geopolymer mixes, hybrid mixes and binary mixes. The hybrid mixes were obtained by replacing a portion of the primary precursor (calcined or uncalcined laterite) with either calcium carbonate or Portland cement, while the binary contained only laterite (calcined or uncalcined laterite) and Portland cement. However, the binary mixes were not the focus of this laboratory investigation and were only considered to further differentiate the contribution of the Portland cement from that of the activators. The binary mixes had the same mix design parameters as the hybrid mixes containing Portland cement, except for the activators. The activators were only incorporated in the hybrid and geopolymer mixes.

Table 4.1: Mix design of mortar per unit volume.

	Mix Design of the Mortar							
	Geopolymer		Hybrid				Binary	
Materials (kg/m3)	**G-CL**	**G-UL**	**H-CL/CC**	**H-UL/CC**	**H-CL/PC**	**H-UL/PC**	**B-CL/PC**	**B-UL/PC**
Calcined Laterite (CL)	520	-	312	-	312	-	312	-
Uncalcined Laterite (UL)	-	520	-	312	-	312	-	312
Calcium Carbonate (CC)	-	-	208	208	-	-	-	-
Portland Cement (PC)	-	-	-	-	208	208	208	208
Total Water Content	260	260	260	260	260	260	260	260
Sodium Hydroxide	104	104	104	104	104	104	-	-
Sodium Silicate	260	260	260	260	260	260	-	-
Fine Aggregate	1430	1430	1430	1430	1430	1430	1430	1430
Compressive strength* (MPa)	12.0	5.4	23.9	10.2	27.0	9.9	21.4	13.1
Spread Flow (mm)	106.8	99.8	114.3	123.4	97.9	107.6	94.7	98.3

* 28-day compressive strength of the mortar

Mix Notations:

G-CL: Geopolymer mix made of calcined laterite

G-UL: Geopolymer mix made of uncalcined laterite

H-CL/CC: Hybrid mix made of calcined laterite and calcium carbonate

H-UL/CC: Hybrid mix made of uncalcined laterite and calcium carbonate

H-CL/PC: Hybrid mix made of calcined laterite and Portland cement

H-UL/PC: Hybrid mix made of uncalcined laterite and Portland cement

B-CL/PC: Binary mix made of calcined laterite and Portland cement

B-UL/PC: Binary mix made of uncalcined laterite and Portland cement

A water-to-binder (precursor) ratio of 0.5 was adopted for both paste and mortar to avoid the use of superplasticizer, and the water content of the sodium silicate solution was accounted for during mixing. The mortar mixes consisted of 1 part precursor(s) and 2.75 parts of fine aggregate, adopting ASTM C109 [1]. A single replacement level of 40% was considered for the secondary precursors. The mix designs of mortar are presented in Table 4.1. As shown in Table 4.1, the mix labels indicate the category of the mix and the type of precursor(s) used.

After the initial selection of the activator, as mentioned in Section 3.2.4, several trial mixes were also conducted to determine the suitable dosage of the sodium hydroxide. From these trials, a dosage of 10 molarity (M) of sodium hydroxide was selected and used with the sodium silicate solution at the ratio of 1:2.5, as established previously. This decision was based on the 7- and 21-day compressive strength data of the calcined laterite geopolymer mix (G-CL) as presented in Table 4.2, which considered 8 and 10 M of NaOH, respectively, with sodium silicate solution at the established ratio.

Table 4.2: Impact of activator dosage on compressive strength of mix G-CL.

	Compressive Strength (MPa)	
	Day 7	**Day 21**
8M NaOH	3.4 (± 1.0)	4.8 (± 0.7)
10M NaOH	7.2 (± 0.3)	9.6 (± 0.4)

It is worth emphasizing that granulated sodium metasilicate pentahydrate, which consisted of 28% Na_2O, 28% SiO_2 and 44% H_2O, was first considered for the laboratory experiment but its use presented dissolution and crystallisation challenges. Dissolving the metasilicate at ambient temperature was such a difficult task and can be attributed to the dosing quantity, the 2.5 ratio. In order to achieve complete dissolution, the mixing water had to be preheated to a temperature of 40 – 50 degrees Celsius (˚C). However, when the temperature of the solution drops, recrystallization occurs. Accounting for the water content of the metasilicate was also a challenge. When the water content of the metasilicate was subtracted from the mixing water, achieving complete dissolution became impossible as the solution became supersaturated. Without subtracting the metasilicate water content, the total water content of the mix is increased. Therefore, an increase in the sodium hydroxide concentration automatically increases the metasilicate because of the 1:2.5 activator ratio. This increase in the metasilicate content not only increased the total water content but also, reduced the molarity and slightly decreased the potential of hydrogen (pH) of the solution as well.

Table 4.3 presents data which illustrate the impact of not accounting for the water content in metasilicate on the molarity, pH, and total water content of the mixing solution. This data set contained various quantities of sodium hydroxide and metasilicate required to prepare solutions with concentrations ranging from 8 to 14 M of NaOH in 8 ml of mixing water, as well as the corresponding molarity and pH values for each concentration. The pH measurements were obtained using the Hanna HI9811-51 portable meter.

Table 4.3: Effects of metasilicate water content on the mixing solution.

Molarity of NaOH per 8 ml	8M	9M	10M	12M	14M
Quantity of NaOH (g)	2.56	2.88	3.20	3.84	4.48
Quantity of Na_2SiO_3 (g)	6.40	7.20	8.00	9.60	11.20
Quantity of H_2O in Na_2SiO_3 (ml)	2.82	3.17	3.52	4.22	4.93
Total H_2O (ml)	10.82	11.17	11.52	12.22	12.93
Molarity of NaOH per Total H_2O	5.92	6.45	6.94	7.85	8.66
Potential of Hydrogen (pH)	10.2	10.0	9.8	9.5	9.1

Although the sodium silicate solution had a higher water content (63.25%) compared to the metasilicate, accounting for its water content from the mixing water did not present any issues as sodium hydroxide was the only pellet that needed to be dissolved. The use of the sodium silicate solution ensures that the water content is kept constant regardless of the concentration of sodium hydroxide, as illustrated in Table 4.4. It is worth highlighting that the use of sodium silicate solution resulted in a higher pH compared to the granulated sodium metasilicate pentahydrate. However, the use of sodium silicate solution was not without challenges. Increasing the sodium hydroxide concentration above 10 M resulted in increased viscosity of the solution and rapid stiffening of the mixture. Under these conditions, achieving proper mixing became difficult, hence limiting the trials for compressive strength testing to not more than 10 M of NaOH, as presented in Table 4.2.

Table 4.4: pH and molarity of the mixing solution when using liquid sodium silicate.

Molarity of NaOH per 8 ml	8M	9M	10M	12M	14M
Quantity of NaOH (g)	2.56	2.88	3.20	3.84	4.48
Quantity of Na_2SiO_3 (g)	6.40	7.20	8.00	9.60	11.20
Quantity of H_2O in Na_2SiO_3 (ml)	4.05	4.55	5.06	6.07	7.08
Total H_2O (ml)	8.00	8.00	8.00	8.00	8.00
Molarity of NaOH per Total H_2O	8.00	9.00	10.00	12.00	14.00
pH	11.0	10.9	10.6	10.2	10.0

The replacement level of the secondary precursors was determined through trials involving only calcium carbonate since it was the principal replacement material. As stated in Section 3.2.3, the inclusion of Portland cement as a secondary precursor is based on its widespread availability, which makes Portland cement an accessible source of calcium oxide in developing countries. The selected replacement level was based on strength development and rate of slump loss. Table 4.5 presents the 7-day results of the compressive strength involving 30 – 50% replacement of the calcined laterite with calcium carbonate. Although the results indicate that higher replacement levels of calcium carbonate correspond to increased compressive strength, the fresh mixes also exhibited instantaneous settings due to the rapid reaction between the activators and the calcium carbonate, leaving very little time for proper mixing and placing. Therefore, the 40% replacement level seems to be the compromise if the use of retarders is to be avoided.

Table 4.5: Impact of calcium carbonate on compressive strength.

	Compressive Strength (MPa)		
	H-CL/CC30	**H-CL/CC40**	**H-CL/CC50**
Day 7	14.3 (± 0.2)	17.5 (± 0.6)	18.9 (± 0.9)

4.4 Casting and Curing Procedure

All mixing was done by hand since most of the batching was done in small quantities. For the mortar, the mixing was done in batches of 4 kg in a 5 L stainless steel bowl. The dry materials were first mixed for 3 minutes before introducing the activating solution. Once the activating solution was added, the mixing continued for another 2 minutes. After, the mortar was cast in 50-mm cube steel moulds. A similar mixing procedure was also followed for the paste, which was cast in 34-mm cube plastic moulds.

The mixing solutions were prepared on the day of casting, and this was done to avoid the thickening of the solution. The preparation of the activating solution involves adding the appropriate amount of sodium hydroxide required to prepare 10 M solution based on the total water content of the mix and the corresponding amount of sodium silicate solution to the mixing water, taking into consideration the water content of the silicate solution. The solution was then stirred and allowed to cool to about 35 ± 5 ˚C before use. Allowing the solution to cool below this temperature range presented mixing difficulties, particularly with the hybrid mixes. All mixes, including those examined for fresh properties, were prepared within this temperature range.

After casting, the moulds were wrapped in polyethene plastic and demoulded after 24 hours. Upon demoulding, all cube specimens were wrapped in several layers of polyethene plastic sheets and sealed to facilitate curing at ambient temperature (23 ± 2 ˚C). The wrapped specimens were subsequently stored in black plastic boxes under the ambient conditions of the laboratory until testing.

The decision to employ ambient curing was predicated upon the trial results involving both heat and ambient curing, presented in Figure 4.2. The curing regimes investigated were continuous curing at ambient temperature (23 ± 2 ˚C) and curing at 50 ˚C in a ventilated oven for only 24 hours and five days, respectively, and thereafter, ambient curing. The trial also considered curing sealed samples continuously in water at temperatures of 40 and 50 ˚C. However, this approach was quickly abandoned as the seepage of moisture through the wrapped plastic could not be avoided. As shown in Figure 4.2, the results indicate that both the higher temperature and exposure duration negatively impacted the compressive strength development of the hybrid mix containing calcium carbonate (H-CL/CC). Although the incorporation of the secondary precursors promotes room temperature curing, the trials also sought to explore, if any, the benefit of higher temperature curing on the principal secondary precursor. It is important to note that the hybrid mix containing calcium carbonate was the only mix investigated during the curing trials as it is well established that heat curing is the most preferential curing method for geopolymers made from low-calcium aluminosilicates [2–5].

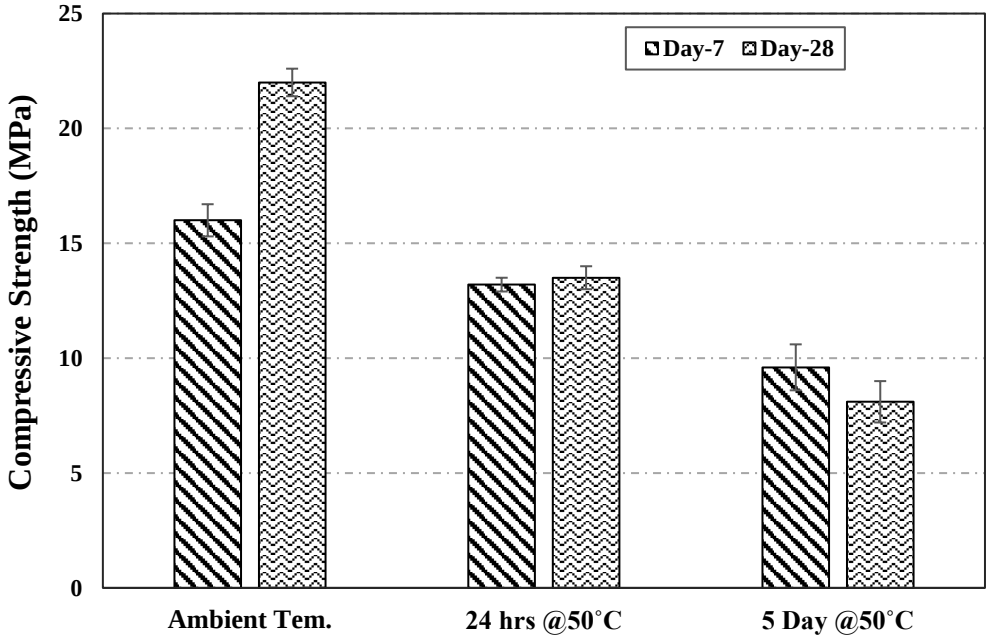

Figure 4.2: Influence of curing regime on the compressive strength of mix H-CL/CC.

4.5 Fresh Properties

The fresh properties investigated included workability, setting times, and the heat of reaction. Workability was examined using the flow table test, setting times were determined using the Vicat apparatus, and the heat of reaction was measured by tracking the heat released during the geopolymerisation process with an isothermal calorimeter.

4.5.1 Flow Table Test

The flow table test was performed according to ASTM C230 [6] but based on the free flow of the paste and mortar samples. As shown in Figure 4.3, the apparatus involved a flow table with a diameter of 255 mm and cylindrical brass mould with a height of 50 mm and a top and bottom diameter of 70 and 100 mm, respectively. The apparatus was oiled, and the samples placed in the cylindrical mould and filled appropriately. After, the mould was lifted steadily in a vertical manner, and the samples were allowed to flow without blows being applied. Following this, the diameter of the spread was recorded at four points along the spread and the average reported.



Figure 4.3: Flow table apparatus.

4.5.2 Setting Times

The setting times were conducted according to EN 196-3 [7]. A sample size of 400 grams of the precursor(s) was mixed appropriately with the required amount of activating solution. The Vicat mould was first oiled, placed on an oiled steel plate and then properly filled with the

required amount of paste. The test sample was then allowed to sit for 60 seconds before being placed under the Vicat instrument. Before oiling the base plate, the base plate was placed under the Vicat apparatus, and the plunger, along with the initial setting needle attached, was lowered to rest on the base plate and adjusted to read zero. As prescribed by EN 196-3 [7], the initial setting was determined when the Vicat needle penetrated to a range of 6 ± 3 mm from the bottom of the mould, and for the final set, when the needle of the final setting time failed to leave a ring mark on the inverted surface of the samples. The setting time test was conducted under a controlled environment with a temperature of 23 ± 2 ˚C and humidity between 50 – 60%.

4.5.3 Heat of Reaction

The heat of reaction, in the context of this investigation, refers to the amount of heat liberated when the mixing solution (activating solution or water) comes in contact with the precursor(s) and this process was examined through isothermal calorimetry. Isothermal calorimetry is a technique used to measure heat released or absorbed during a chemical reaction or a physical process [8, 9]. The fundamental concept of isothermal calorimetry involves measuring the heat flow into or out of a sample under constant temperature within a controlled system. Measuring the heat flow associated with a chemical process, such as geopolymerisation, provides valuable information about the reaction kinetics and thermodynamics [10].

For this study, an I-Cal 4000 HPC Isothermal Calorimeter was used to monitor the amount of heat released or absorbed during the geopolymerisation process. Figure 4.4 illustrates the arrangement of the calorimetry setup employed in this investigation, which comprised an I-Cal 4000 HPC Isothermal Calorimeter unit and a laptop equipped with CalCommander software for controlling the unit. The testing procedures included configuring the isothermal calorimeter to a temperature of 23 ± 2 ˚C and allowing it to equilibrate for 24 hours before commencing the test. The room housing the calorimeter is a controlled environment, and the temperature was also set to 23 ± 2 ˚C.

Given that the dissolution of sodium hydroxide is exothermic, the mixing solutions were not kept in the calorimeter, as the solution temperature needed to be monitored. Instead, the solutions were kept under the ambient conditions of the room hosting the calorimeter until the temperature cooled down to 30 ˚C. Once the temperature of the mixing solution reached 30 ˚C, a sample size of 20 grams of precursor(s) was mixed with the solution and placed in the calorimeter, and the heat of reaction was recorded over a period of 72 hours. The mixing was

done by hand as this calorimeter does not have a stirrer attached. The heat flow was logged at intervals of 10 seconds for the first 60 minutes and then every minute for the rest of the 72 hours.



Figure 4.4: Setup of the isothermal calorimeter.

4.6 Compressive Strength Testing

The compressive strength testing was conducted on 50 x 50 x 50 mm mortar cubes in accordance with ASTM C109 [1]. ASTM C109 was selected for this study because it specifically outlines testing procedures for 50-mm mortar cube specimens, including the mix proportion. The compressive strength was tested at 7, 14, 28, 56, 90, and 180 days after casting. The applied loading rate was 100 kN/min, and the reported value is the average of three cubes.

4.7 Microstructural Characterisation

The microstructural characterisation was conducted to gain insights into the phases forming and transformations occurring within the hardened matrix, particularly in relation to pore structure and porosity evolution.

4.7.1 Porosity and Pore Structure

The porosity and pore structure of the hardened paste were examined up to 180 days after casting, employing the solvent exchange technique and Helium Pycnometry.

4.7.1.1 Isopropanol Solvent Exchange

The solvent exchange method, also called the solvent replacement technique, was employed to investigate transport-related properties of the hardened geopolymer paste. As the name implies,

the solvent exchange method involves the removal of one solvent with another within a given system through a counter-diffusion process [11]. This technique, specifically isopropanol solvent exchange, is widely used by cement and concrete researchers for hydration stoppage and the removal of pore water [12,13]. However, solvent replacement technique has also been used to study pore structure and porosity in hydrated cement paste [14–17]. Solvent exchange provides information on the rate of diffusion of solvents through a medium as well as the diffusion coefficient, total pore volume, and pore connectivity of the medium undergoing the exchange process, all under the assumption that there is little or no chemical interaction between the solvent and the medium. The porosity obtained by solvent exchange is based on the total pore volume accessible to the solvent.

The procedure of the solvent exchange generally involves submerging the samples in an organic solvent, which has lower surface tension and specific density than water and allowing the solvent to diffuse through the samples, replacing any water that may be present within the microstructure. The solvent employed in this study was isopropanol, with a purity level of 99%. Isopropanol was selected because of its low surface tension and specific density compared to other organic solvents, as well as its high rate of diffusion and miscibility in water. It is worth noting that the solvent exchange process was also part of the sample preparation procedures for the phase identification analyses.

In this study, the solvent exchange was conducted on paste samples of 34-mm cubes, and Figure 4.5 displays samples of cubes utilised in the exchange process. The setup of the solvent exchange comprised a sealable 2-litre rectangular plastic container for hosting the isopropanol, along with three cube specimens for each test and a weight balance with an accuracy of two decimal places. The ratio, in terms of volume, of the isopropanol solution to sample was set at 15:1, and the solution was not renewed during the test period. The exchange process was carried out under a controlled environment with a temperature of 23 ± 2 ˚C and humidity between 50 – 60%. The initial masses of the samples and dimensions were first recorded before being placed in the isopropanol solution and weighed at various intervals over a specified period. During the first 24 hours of submersion, the samples were weighed at 15-minute, 30-minute, 1-hour, 2-hour, 4-hour, 8-hour, 12-hour and 24-hour intervals. Thereafter, the samples were weighed once after every 24 hours up to 144 hours. The diffusion test lasted for 6 days, and during weighing, the samples were wiped to a saturated-surface-dry condition with a paper towel, weighed and placed back in the isopropanol solution. At the end of the saturation period, the samples were placed in a ventilated oven and dried for 48 hours to a constant weight. Upon

removal from the oven, the samples were allowed to cool to a temperature of 23 ± 2 ˚C in a desiccator for about 2 hours before recording the oven dry masses.

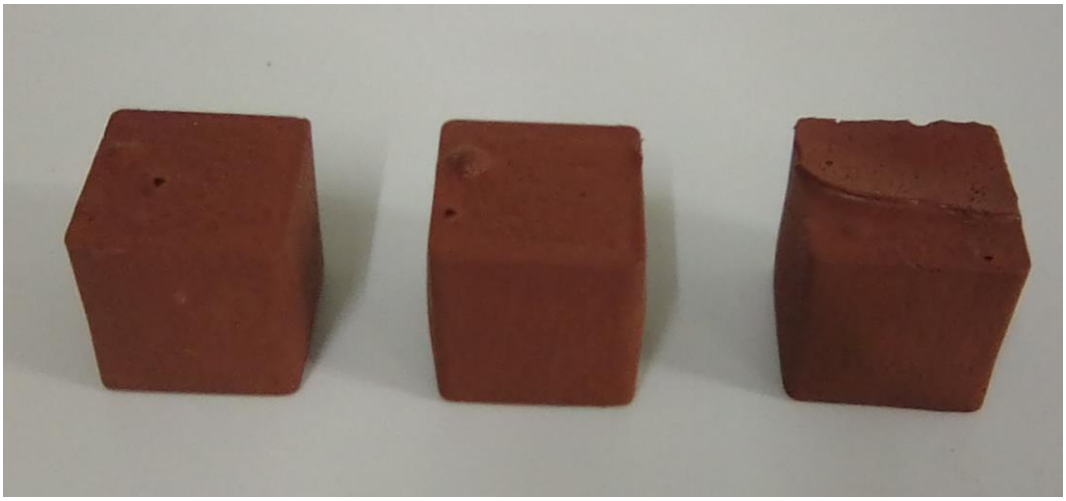

Figure 4.5: Samples of 34-mm paste cube.

The exchange data was then analysed to obtain the rate of diffusion and the total porosity (pore volume occupied by the isopropanol). The rate of diffusion is obtained by plotting the quantity of isopropanol diffused (g/cm^3) vs time. Given the premise that isopropanol exchanges pore water on a one-to-one volume basis [15,17], the quantity of isopropanol diffusing after a given time can be calculated using Equation – 4.1 [18].

$$W_t = \frac{D_{ISO}}{D_W}[M_i - M_t] \qquad \text{Equation -------4.1}$$

Where $\mathbf{W_t}$ is the quantity of isopropanol diffused after a given time in grams, $\mathbf{D_{ISO}}$ and $\mathbf{D_w}$, the density of isopropanol and water, respectively, and $\mathbf{M_i}$ and $\mathbf{M_t}$, the initial mass and mass of the sample after a given time, respectively. The unit weight per volume (g/cm^3) is obtained by dividing the $\mathbf{W_t}$ by the measured volume of the sample prior to the solvent exchange process.

The porosity based on the solvent exchange data can be computed by subtracting the oven-dry mass from the final isopropanol saturated mass, as expressed in Equation – 4.2. The porosity can also be obtained using the initial mass of the samples, as expressed in Equation – 4.3 [19].

$$P_{SSM}(\%) = \frac{SS_M - OD_M}{OD_M} \times 100 \qquad \text{Equation -------4.2}$$

Where $\mathbf{P_{SSM}}$ is the porosity obtained from the solvent-saturated mass, $\mathbf{SS_M}$, the solvent-saturated mass and $\mathbf{OD_M}$, the oven-dry mass of the sample.

$$P_{IM}(\%) = \frac{I_M - OD_M}{OD_M} \times 100 \qquad \text{Equation -------4.3}$$

Where $\mathbf{P_{IM}}$ is the porosity derived from the sample's initial mass, $\mathbf{I_M}$, the initial mass and $\mathbf{OD_M}$, the oven-dry mass.

The duration of the solvent exchange period was established from trials conducted to ascertain the time to full saturation at the given solution-to-sample ratio. The trials were conducted on samples of Mix G-CL and lasted for eight days. From the trails, as presented in Figure 4.6, it took approximately 144 hours to reach saturation. Another aspect investigated during the trials was regularly renewing the solution to ensure boundary conditions are kept constant. Contrary to reports from other studies [15,18,20], renewing the solution during the exchange process did not seem to keep the diffusion process in a steady state. A sharp rise or an abrupt upward slope was observed in the diffusion curve each time the solution was renewed. It should be noted that the diffusion curve shown in Figure 4.6 is derived from a non-renewed solution trial.

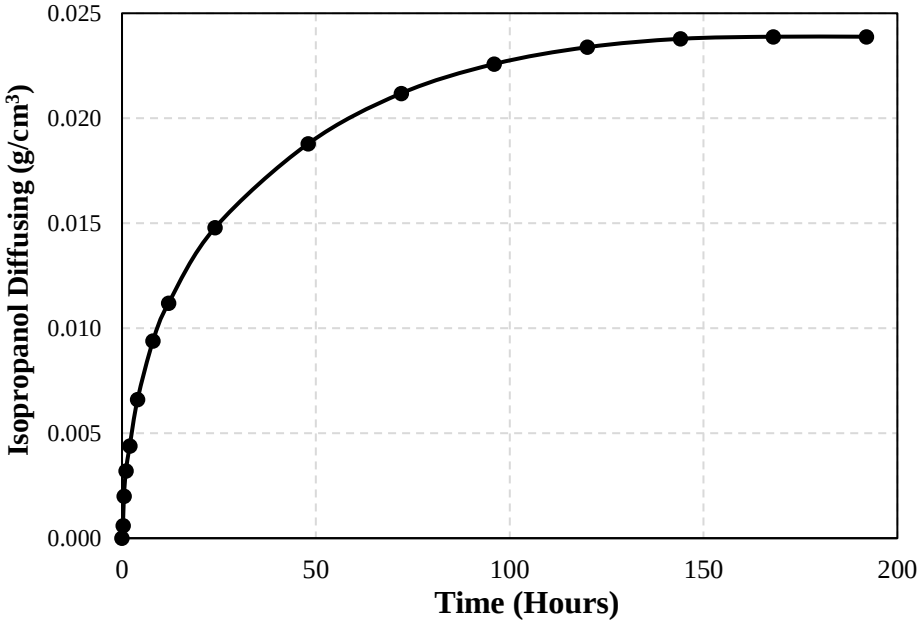

Figure 4.6: Rate of isopropanol diffusion through the trial sample.

4.7.1.2 Helium Pycnometry

Helium Pycnometry, a technique used to determine the true density of a substance by measuring its true volume using helium gas as the displacing medium, was applied to examine the total pore volume of hardened geopolymer pastes. Helium, due to its small size and inert nature, has the ability to penetrate and fill pores or empty spaces within a material. This unique property is at the core of Helium Pycnometry. The fundamental principle of Helium Pycnometry

involves measuring the change in pressure in a closed chamber with a known volume. As helium displaces the air or any other gas within the pores of the sample, it facilitates the determination of the true volume of the sample through gas law relationships. This, in turn, enables the calculation of the true density of the sample. It is important to note that while Helium Pycnometry provides information about the total pore volume within a sample, it does not provide information about the pore sizes or pore size distribution within the sample [19].

In this investigation, the procedure involved introducing the oven-dry sample from the solvent exchange experiment into the Helium pycnometer, inputting the sample mass (oven-dry mass) and obtaining the true volume or skeleton density of the samples. The porosity of the sample was subsequently obtained by Equation – 4.4 using the true volume and the apparent or bulk volume of the sample prior to the solvent exchange process. The calculation of porosity is based on the assumption that volume change is negligible, given the presumed absence of interaction between the isopropanol and the hardened paste during the solvent exchange process. Figure 4.7 illustrates the arrangement of the pycnometer setup. The specific Helium pycnometer employed for the experiment was the Anton Paar Ultrapyc 3000 true density analyser.

$$P_{HP}(\%) = \left[1 - \frac{V_T}{V_A}\right] \times 100 \qquad \text{Equation -------4.4}$$

Where $\mathbf{P_{HP}}$ is the porosity obtained using a Helium pycnometer, $\mathbf{V_T}$, is the true volume of the sample and $\mathbf{V_A}$, the apparent volume or bulk volume of the sample.



Figure 4.7: Setup of the Helium Pycnometer.

4.7.2 Phase Identification

X-ray diffraction and Fourier transform infrared spectroscopy were employed to determine the phase assemblage of the reaction product. The sample preparation involved crushing the oven-dry specimens from the solvent exchange method and sieving to achieve a particle size of less than 300 μm. The XRD and FTIR analyses were performed on samples as early as 24 hours after casting and up to 180 days.

4.7.2.1 X-ray Diffraction

X-ray diffraction (XRD) is an analytical technique for characterising the structure of crystalline materials [21]. This technique is among the most widely used methods for identifying crystalline phases as it offers a rapid and non-destructive approach to characterisation [22,23]. The fundamental concept of XRD involves the interaction of X-ray with a crystalline sample, resulting in the scattering of X-ray in specific directions and forming a distinct pattern. This scattering pattern, referred to as a diffraction pattern, provides unique information about the crystal structures that are unique to the compounds within the sample. The diffraction pattern can then be cross-referenced against a database of crystal structures to identify the phases present in the sample.

In this study, XRD was used to obtain both qualitative and semi-quantitative information about the crystalline structures in the sample. The testing procedures involved loading the powdered sample onto the sample holder and placing it in the Bruker D2 Phaser XRD machine. The sample was scanned within the range of 5 to 90 degrees 2-theta in 30 minutes. The resulting X-ray diffractogram was analysed in High Score Plus software using Crystallography Open Database (COD 2023) and Inorganic Crystal Structure Database (ICSD 2004).

4.7.2.2 Fourier Transform Infrared Spectroscopy

Fourier transform infrared spectroscopy (FTIR) is an analytical technique used to identify chemical composition of a material based on its molecular structure or functional groups. The basic principle of FTIR involves exposing a sample to infrared light and measuring the amount of light that is absorbed (absorption) or passed (transmittance) through. The absorption or transmittance data are then used to generate an infrared spectrum that provides information about the molecular composition and structure of the sample.

For this investigation, powdered samples were tested using the Attenuated Total Reflectance (ATR) mode of the FTIR. Prior to testing, the ATR crystal was cleaned, and the background measurement taken. Subsequently, the powdered sample was placed on the crystal, and the

knob tightened to ensure proper contact. The sample was then exposed to infrared radiation, and the spectrum was acquired within the range of 4000 to 400 cm^{-1} through 16 scans at a resolution of 2 cm^{-1}. The obtained spectrum was compared with reference spectra from published literature to analyse the results. The instrument used in this investigation was the PerkinElmer FTIR Spectrometer, Spectrum Two.

4.8 Summary

This chapter presents the methods and procedures employed in the laboratory investigation to examine the fresh and hardened properties of aluminous laterite-derived geopolymer. It also provides results from preliminary investigations on the optimization of the mix design, including activator concentration and the replacement level of the secondary precursors, as well as the impact of curing conditions on the strength development of the geopolymer derived from aluminous laterite. The laboratory investigation examined the rheology, setting times, and reaction kinetics of the fresh mix, as well as compressive strength development, pore structure, and phase assemblage of the hardened product resulting from the geopolymerisation process. In the laboratory investigation, three categories of mixes were considered: geopolymer, hybrid, and binary, and each category comprised both calcined and uncalcined laterite mixes. The samples or specimens were cured at ambient temperature, and their hardened properties were examined up to 180 days after casting.

4.9 References

1. ASTM C109, Standard Test Method for Compressive Strength of Hydraulic Cement Mortars (Using 2-in. or [50-Mm] Cube Specimens), (2009).
2. Palomo, A., Grutzeck, M.W., Blanco, M.T., Alkali-Activated Fly Ashes: A Cement for the Future, *Cement and Concrete Research*. (1999) **29** 1323–1329.
3. Swanepoel, J.C., Strydom, C.A., Utilisation of Fly Ash in a Geopolymeric Material, *Applied Geochemistry*. (2002) **17** 1143–1148.
4. Najafi Kani, E., Allahverdi, A., Effects of Curing Time and Temperature on Strength Development of Inorganic Polymeric Binder Based on Natural Pozzolan, *Journal of Materials Science*. (2009) **44** 3088–3097.
5. Heah, C.Y., Kamarudin, H., Bakri, A.M.M.A., Binhussain, M., Luqman, M., Nizar, I.K., Ruzaidi, C.M., Liew, Y.M., Effect of Curing Profile on Kaolin-Based Geopolymers, *Physics Procedia*. (2011) **22** 305–311.

6. ASTM C230, Standard Specification for Flow Table for Use in Tests of Hydraulic Cement, (2003).
7. BS EN 196-3, Methods of Testing Cement – Part 3: Determination of Setting Times and Soundness, (2016).
8. Mazzei, L., Ciurli, S., Zambelli, B., Isothermal Titration Calorimetry to Characterize Enzymatic Reactions, In: A.L. Feig (Editor), *Methods in Enzymology*, Academic Press, (2016): pp. 215–236.
9. Khalef, N., Campanella, O., Bakri, A., Isothermal Calorimetry: Methods and Applications in Food and Pharmaceutical Fields, *Current Opinion in Food Science*. (2016) **9** 70–76.
10. Zogg, A., Stoessel, F., Fischer, U., Hungerbühler, K., Isothermal Reaction Calorimetry as a Tool for Kinetic Analysis, *Thermochimica Acta*. (2004) **419** 1–17.
11. Parrott, L.J., Effect of Drying History upon the Exchange of Pore Water with Methanol and upon Subsequent Methanol Sorption Behaviour in Hydrated Alite Paste, *Cement and Concrete Research*. (1981) **11** 651–658.
12. Winnefeld, F., Schöler, A., Lothenbach, B., Sample Preparation, In: *A Practical Guide to Microstructural Analysis of Cementitious Materials*, CRC Press Boca Raton, FL, USA, (2016): pp. 1–32.
13. Snellings, R., Chwast, J., Cizer, Ö., De Belie, N., Dhandapani, Y., Durdzinski, P., Elsen, J., Haufe, J., Hooton, D., Patapy, C., Santhanam, M., Scrivener, K., Snoeck, D., Steger, L., Tongbo, S., Vollpracht, A., Winnefeld, F., Lothenbach, B., RILEM TC-238 SCM Recommendation on Hydration Stoppage by Solvent Exchange for the Study of Hydrate Assemblages, *Materials and Structures*. (2018) **51** 172.
14. Parrott, L.J., Thermogravimetric and Sorption Studies of Methanol Exchange in an Alite Paste, *Cement and Concrete Research*. (1983) **13** 18–22.
15. Day, R.L., Marsh, B.K., Measurement of Porosity in Blended Cement Pastes, *Cement and Concrete Research*. (1988) **18** 63–73.
16. Thomas, M.D.A., The Suitability of Solvent Exchange Techniques for Studying the Pore Structure of Hardened Cement Paste, *Advances in Cement Research*. (1989) **2** 29–34.
17. Feldman, R.F., Diffusion Measurements in Cement Paste by Water Replacement Using Propan-2-OL, *Cement and Concrete Research*. (1987) **17** 602–612.
18. Beaudoin, J.J., Marchand, J., Pore Structure, In: *Analytical Techniques in Concrete Science and Technology, 1st Ed.; Ramachandran, VS, Beaudoin, JJ, Eds*, (2001): pp. 528–628.

19. Aligizaki, K.K., Pycnometry and Thermoporometry, In: *Pore Structure of Cement-Based Materials: Testing, Interpretation and Requirements*, CRC Press, (2005).
20. Zhang, J., Scherer, G.W., Comparison of Methods for Arresting Hydration of Cement, *Cement and Concrete Research*. (2011) **41** 1024–1036.
21. Snellings, R., X-Ray Powder Diffraction Applied to Cement, In: *A Practical Guide to Microstructural Analysis of Cementitious Materials*, CRC Press Boca Raton, FL, USA, (2016): pp. 104–176.
22. Poppe, L.J., Paskevich, V.F., Hathaway, J.C., Blackwood, D.S., A Laboratory Manual for X-Ray Powder Diffraction, *US Geological Survey Open-File Report*. (2001) **1** 1–88.
23. Das, R., Ali, E., Abd Hamid, S.B., Current Applications of X-Ray Powder Diffraction – A Review., *Reviews on Advanced Materials Science*. (2014) **38**.

Chapter 5

Results and Discussion

5.1 Introduction

Aluminium-rich laterite, owing to its accessibility and widespread abundance, emerges as a potentially attractive indigenous source of aluminosilicates. However, the lack of available data to confirm its suitability for geopolymerisation has prompted this research. An in-depth laboratory investigation, scrutinising both the properties of geopolymer derived from aluminium-rich laterite and the characteristics of the aluminous laterite itself, has been conducted. Chapters 3 and 4 of this thesis comprehensively cover the characterisations of the laterite and examinations of the properties and performance of geopolymer derived from aluminium-rich laterite, respectively. Therefore, this chapter presents the findings of the laboratory investigation aimed at examining the setting times, flow behaviour, reaction kinetics, compressive strength, phase composition, and pore structure of geopolymers derived from aluminous laterite.

The laboratory investigation considered three categories of mixes, namely geopolymer, hybrid, and binary. Each category consisted of both calcined and uncalcined laterite mixes to assess the impact of milling and calcination on the properties of the derived geopolymer, as well as the influence of the mineralogical composition of the laterite. The hybrid mixes incorporated either calcium carbonate or Portland cement at a 40% replacement level of the laterite, while the binary mixes only incorporated Portland cement at the same replacement level as the hybrid but without activators. The essence of the binary mixes was to differentiate the contribution of Portland cement from that of the activators.

In addition to presenting the results, this chapter also engages in a discussion that explores the influence of the laterite's composition, its processing procedures, and the inclusion of calcium minerals on the fresh and hardened properties of the derived geopolymer. However, it is important to emphasize that the absence of data on aluminium-rich laterite in geopolymerisation poses a challenge for discussing and interpreting the findings of this laboratory investigation within the broader context of existing literature.

5.2 Fresh Properties

5.2.1 Setting Times

Figure 5.1 presents the results of the initial and final setting times. The findings indicate that both the calcined and uncalcined laterite, as well as the secondary precursors (calcium carbonate and Portland cement), influenced the setting behaviour of the mixes. The calcined laterite geopolymer mix (G-CL) displayed the longest initial and final setting times, with values of 840 and 1080 minutes, respectively, while the shortest setting times were recorded in the binary mix category. The binary mix based on calcined laterite (B-CL/PC) exhibited the shortest initial and final setting times of 30 and 60 minutes, respectively. It should be noted that the setting time test was conducted under a controlled environment, as mentioned in Section 4.5.2, to minimise variability. As a result, only one sample per mix was tested.

Although there is no distinct trend of the setting behaviours across the mixes, the presence of calcium minerals can be seen to cause a reduction in setting times for both the calcined and uncalcined laterite mixes. In terms of reducing setting time, Portland cement proved to be more effective in the calcined laterite series compared to calcium carbonate. Conversely, in the uncalcined laterite series, calcium carbonate demonstrated greater effectiveness than Portland cement in reducing setting times. This trend can be attributed to the coating of Portland cement particles by the clayey particles of the uncalcined laterite, which slows down or hinders hydration [1].

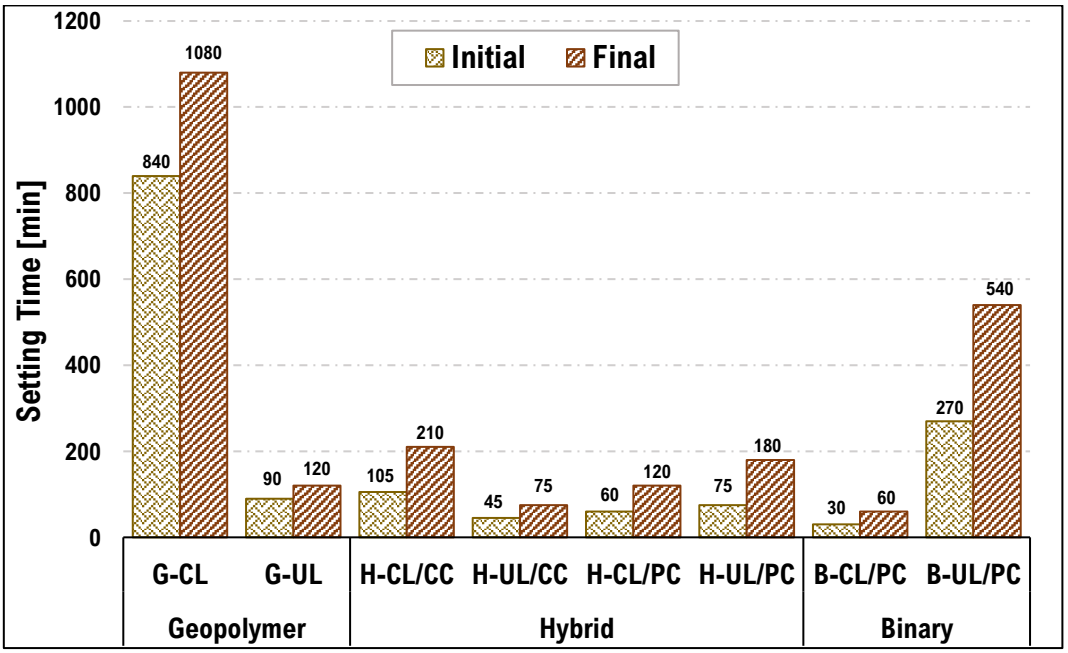

Figure 5.1: Setting times of the mixes.

Interestingly, the uncalcined laterite mix achieved the shortest setting times within the geopolymer category, exhibiting setting times nine (9) times lower than Mix G-CL. This differs from the results reported by Kaze et al. [2], where initial setting times of 4320 and 5040 minutes were observed for two samples of uncalcined iron-rich laterite activated with sodium hydroxide and sodium silicate, and also, 67 and 78 minutes, respectively, for the same materials calcined at 700 ˚C. The behaviour of the uncalcined aluminium-rich laterite mix in this study can be attributed to the rapid reaction between the gibbsite [$Al(OH)_3$] mineral in the uncalcined laterite and the alkaline solution, leading to the formation of precipitates of sodium aluminate silicate. Gibbsite has a high tendency to attract and react with hydroxide ions in solution. Therefore, in the presence of a solution saturated with sodium ions (Na^+), hydroxide ions (OH^-) and silicate ions (SiO_4^{4-}), gibbsite will first react with OH^- ions, forming aluminate ions, which will then react with Na^+ to form sodium aluminate as described in Equations 5.1 and 5.2, respectively. The sodium aluminate will subsequently react with the SiO_4^{4-} species present to form sodium aluminate silicate, as illustrated in Equation 5.3. It is worth noting that the possibility of the below reactions taking place simultaneously exists but has been presented in such a sequence for illustrative purposes. Also, the exact nature of the resulting sodium aluminate silicate depends on several factors, including the concentrations of the various species, prevailing temperature, and pH of the solution.

$$Al(OH)_3 + OH^- \rightarrow Al(OH)_4^- \qquad \text{Equation -------5.1}$$

$$Al(OH)_4^- + Na^+ \rightarrow NaAl(OH)_4 \qquad \text{Equation -------5.2}$$

$$NaAl(OH)_4 + SiO_4^{4-} \rightarrow Na[Al(SiO_4)_2] + 4OH^- \qquad \text{Equation -------5.3}$$

Given the absence of gibbsite in the calcined laterite due to dehydroxylation, it is logical to assume the absence of the above reaction in Mix G-CL, hence the prolonged setting time. The calcined laterite did have an aluminium-bearing compound present in the form of alumina (Al_2O_3) as a result of the dehydroxylation of gibbsite. However, considering the long setting times of Mix G-CL, it can be assumed that the Al_2O_3 is very stable and did not react with the hydroxide ions or, at least, reacted at a much slower rate, making no meaningful contribution to the setting behaviour of the mix. More details on the possible reactions taking place in the mixes are presented in the phase identification section.

In relation to other studies, the setting time values obtained for mix G-CL are far above the range reported in the literature for calcined laterite activated with sodium hydroxide and

sodium silicate. However, it should be noted that the setting times of laterite-based geopolymer reported in the literature vary according to mineralogical composition, activator type and concentration, as well as calcination temperature [3,4].

5.2.2 Spread Flow Diameter

The flow behaviour of the paste and mortar was assessed using the flow table test, and the results are presented in Figure 5.2. As shown in Figure 5.2, the spread flow diameters of pastes within the geopolymer and hybrid mix categories are within the range of 250 ± 5 mm, displaying similar flow behaviour and consistency. For the binary mixes, the pastes exhibited lower spread flow diameters compared to the other categories, with the paste of Mix B-CL/PC displaying the lowest spread diameter of all mixes. The flow behaviour of the geopolymer and hybrid pastes can be attributed to the viscosity of the activating solution. The viscosity of the activating solution controlled the flow behaviour of the geopolymer and hybrid pastes. As mentioned in Section 4.5.1, the viscosity of the activating solution was found to be temperature-dependent. Therefore, at the temperature at which the activating solution was used, the solution exhibited low viscosity (thin consistency and flowed easily). This condition resulted in low stress and reduced resistance, enabling the paste to flow more freely and eliminating the influence of material properties, such as the type of precursors, particle size, and surface area, on the flow behaviour. Given that the impact of temperature on the viscosity of the activating solution was also identified during the preliminary trials, as stated in Sections 4.3 and 4.4, only one sample per mix was tested.

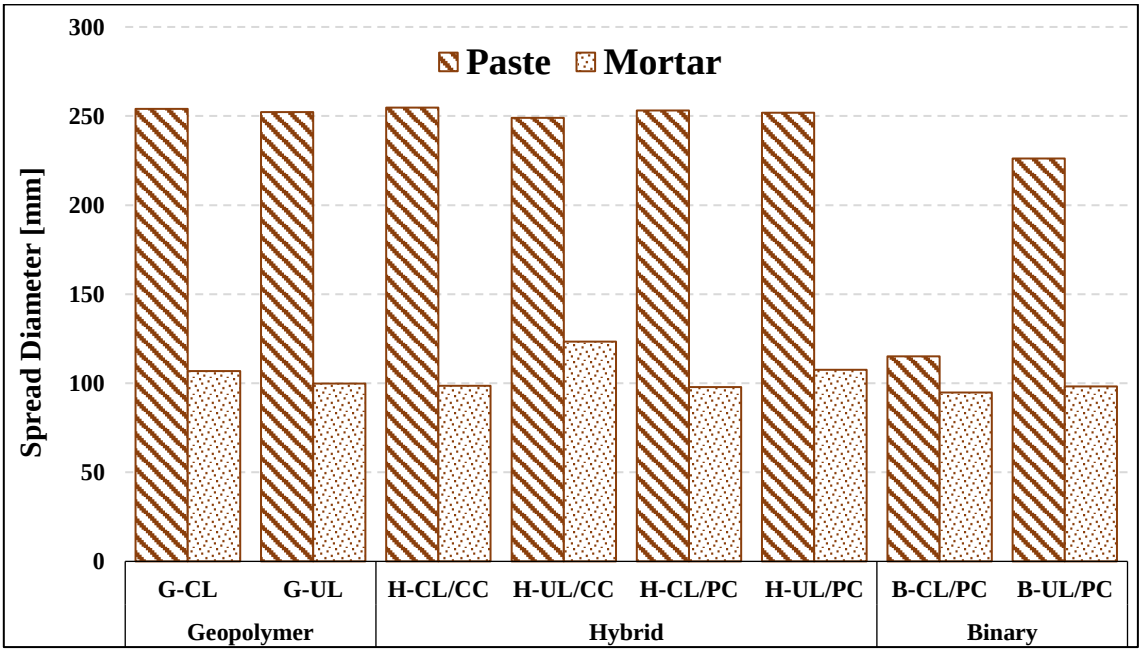

Figure 5.2: Spread flow diameter of the mixes.

For the mortar, the influence of the activating solutions was not as significant as in the paste. However, the inclusion of the aggregate is noticeable due to the low spread diameter of the mortar mixes, which are less than half of the average diameter of the paste samples. Among the mortar, Mix H-UL/CC achieved the maximum spread flow diameter of 123 mm, while Mix B-CL/PC displayed the lowest of 95 mm. It is well-known that the inclusion of aggregates increases shear stress, which, in turn, increases resistance to flow [5]. However, the low spread of the mortar in this study could potentially be attributed to the absorption of mixing water by the fine aggregate, as the mix design process did not account for aggregate absorption. Figures 5.3 and 5.4 present images of the spread flow of paste and mortar, respectively, for all mixes.

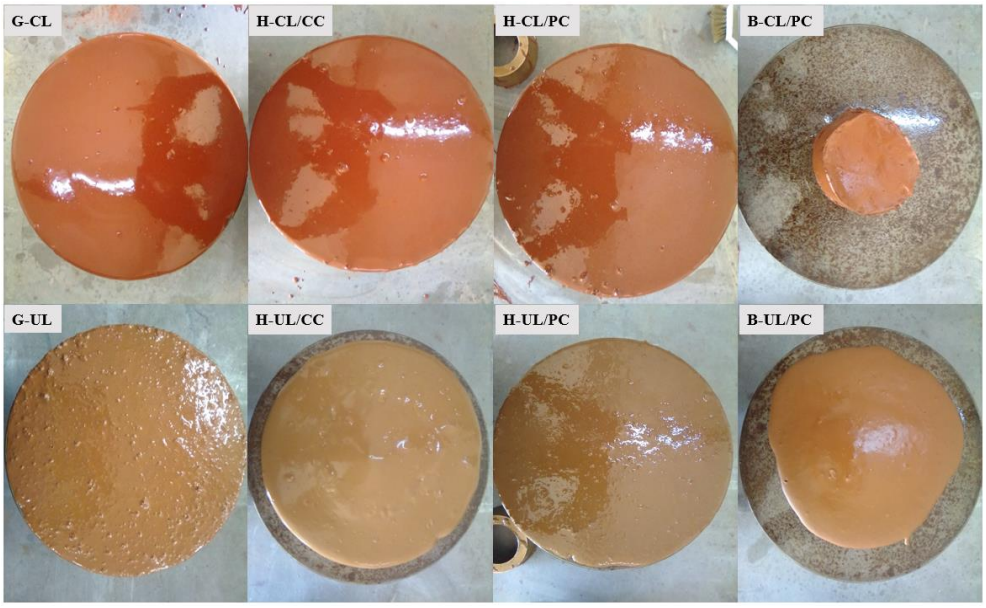

Figure 5.3: Images of spread diameter of the pastes.

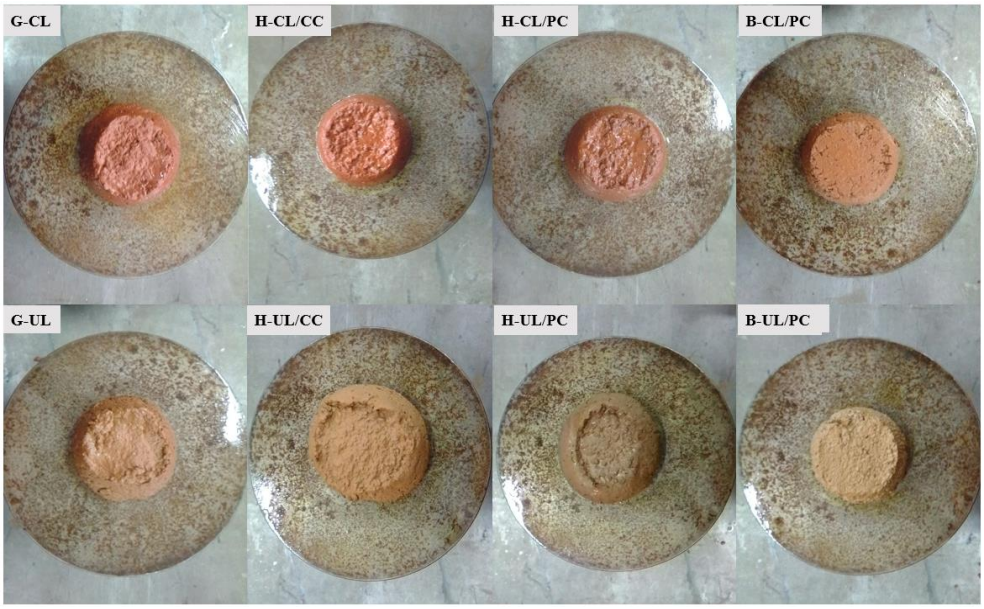

Figure 5.4: Images of spread diameter of the mortars.

5.2.3 Heat of Reaction

Figure 5.5 presents the heat of reaction curves of the mixes for the first 72 hours after the mixing solution came in contact with the precursor(s). The logged heat is presented in Joule per gram of the binder (precursor or precursors). The results show that all calcined laterite mixes within the geopolymer and hybrid categories generated larger amounts of heat than the uncalcined, with Mix G-CL liberating the highest amount of heat. Except for the geopolymer mix based on uncalcined laterite (G-UL), which only exhibited exothermic behaviour within the first 24 hours, all other mixes did give up heat throughout the 72-hour testing period. However, Mix G-UL did display the third highest rate of heat liberation, after Mix H-CL/CC and H-CL/PC, within the first hour of the test duration. In terms of heat liberation, the secondary precursors had the most profound impact on the uncalcined laterite. The mixes containing Portland cement within the hybrid category generated more heat than those containing calcium carbonate.

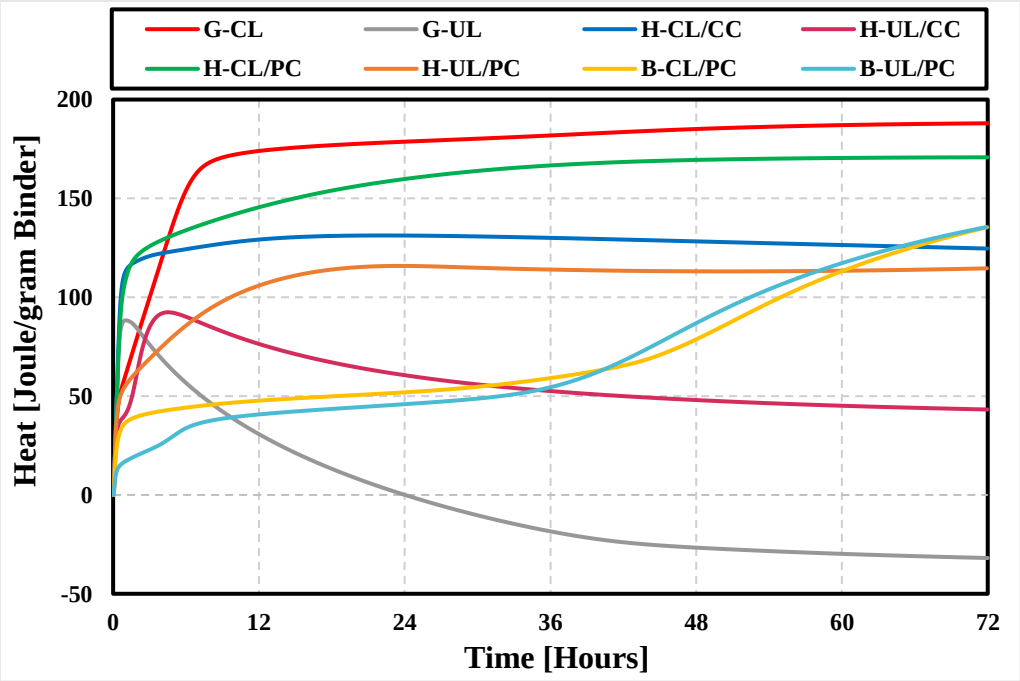

Figure 5.5: Heat of reaction of the mixes.

In the absence of activators, as shown in the binary mixes, the Portland cement generated roughly the same amount of heat in both calcined and uncalcined laterite mixes. This indicates that the presence of the activators enhances the reactivity of both calcined and uncalcined laterite, as demonstrated in Mix H-CL/PC and Mix H-UL/PC. Initially, the binary mixes generated heat at a slower rate. It is only after 36 hours that a sudden rise is observed in the heat flow curve of the binary mixes.

Considering only the exothermic heat exchange, as illustrated in Figure 5.5, the cumulative exothermic heat released for each mix is depicted in Figure 5.6. The cumulative heat release, which provides an indication of the extent of the reaction in each mix other than the total amount of heat generated [6], was obtained by integrating the area under the heat release curve (Figure 5.5) for the respective mixes using Origin software. As depicted in Figure 5.6, Mix G-UL exhibited the lowest cumulative exothermic heat, while Mix G-CL displayed the highest. This comparatively low cumulative exothermic heat of Mix G-UL suggests that the reaction in Mix G-UL did not progress for a longer time during the 72-hour testing period and can be assumed to be incomplete. Additionally, the cumulative exothermic heat data show that the binary mixes (B-CL/PC and B-UL/PC) generated relatively the same amount of heat, indicating that only Portland cement was reacting within the first 72 hours.

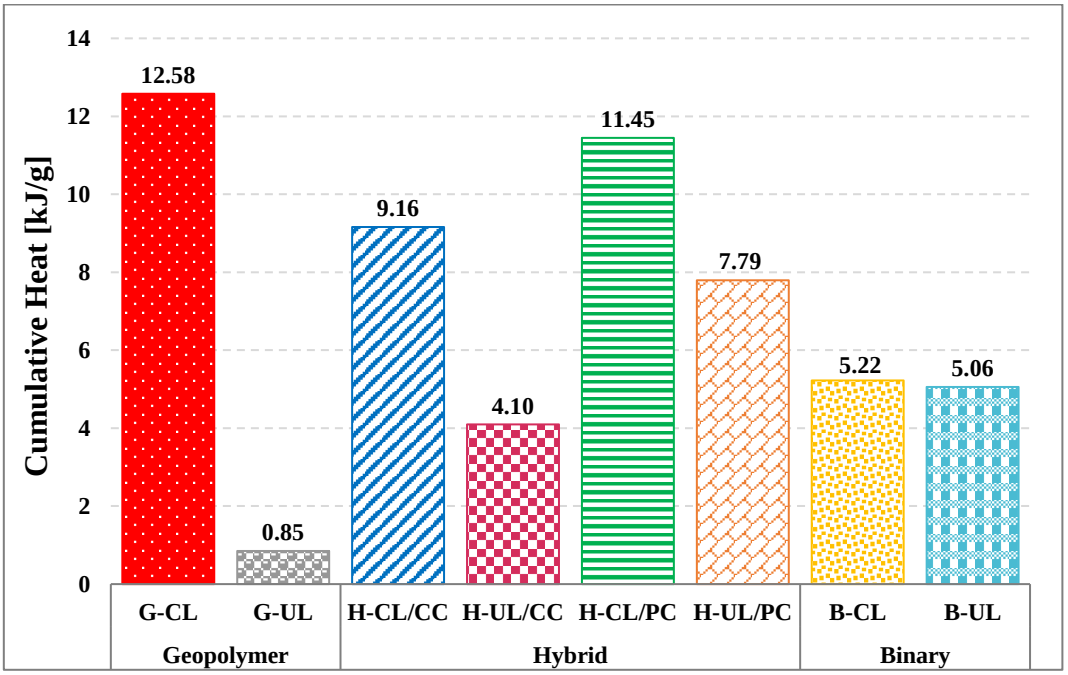

Figure 5.6: Cumulative exothermic heat of reaction of the mixes.

Although the calcined laterite had higher amorphous content compared to the uncalcined, as discussed in Section 3.3, the high heat liberated by Mix G-CL has more to do with the setting behaviour of the mix than the amorphous content of the calcined laterite. In fact, the majority of the amorphous content in the calcined laterite was in the form of alumina (Al_2O_3), given that gibbsite was the dominant mineral and constituted more than two-thirds of the laterite. This alumina, resulting from the calcination of the laterite at 750 ˚C, appears to be less reactive, as evidenced by the prolonged setting of Mix G-CL. Therefore, the high amorphous content of the calcined laterite cannot be linked to the amount of heat released. If the setting behaviour

(stiffening) of the pastes can be linked to the phases forming, then the higher heat liberation of G-CL is linked to the absence of rapid formation of phases. The setting behaviour of Mix G-CL allows the particles of calcined laterite to have sufficient access to the activation solution, enabling the geopolymerisation reaction to continue for a longer period due to the absence of rapid formation of phases.

5.3 Compressive Strength

Figure 5.7 presents the compressive strength results of the mixes. It is worth emphasising that the compressive strength testing was conducted on mortar samples of 50-mm cubes, and the presented results are based on the average of three cubes. The error bars in Figure 5.7 represent the 95% confidence interval and are based on the average of the three cubes ± two (2) standard deviations, assuming normal distribution. As presented in Figure 5.7, the results show that only the hybrid mixes of the calcined laterite series were able to attain structural strength of 25 MPa, that is according to BS EN 206 [7]. The hybrid mix containing calcined laterite and Portland cement (Mix H-CL/PC) achieved structural strength from the 14th day onward, while Mix H-CL/CC only attained structural strength on the 56th day after casting. All mixes in the uncalcined laterite series displayed lower compressive strength and experienced strength retrogression, with the hybrid containing uncalcined laterite and calcium carbonate (Mix H-UL/CC) completely disintegrating by the 90th day.

The binary mixes, in which Portland cement replaced 40% of both calcined and uncalcined laterites but without activators, exhibited higher compressive strength than their respective geopolymer counterparts. Mix B-CL/PC, in particular, achieved a strength of less than 2 MPa short of reaching the 25 MPa benchmark. Considering that the binary mixes were also sealed-cured at ambient temperature (23 ± 2 ˚C), similar to the other mixes, it can be inferred that the binary mixes would have achieved much higher strength if water-cured.

Although Mix B-UL/PC also experienced strength retrogression, the compressive strength seems to stabilise right after the initial decline at Day-56, indicating the presence of more stable phases than the other mixes in the uncalcined laterite series. For instance, Mix H-UL/PC achieved higher strength than Mix B-UL/PC as early as the 7th day after casting. However, over the course of the testing period, the compressive strength of Mix H-UL/PC drastically reduced from 14.4 to 3.9 MPa, which was 64% lower than the 180th-day compressive strength of Mix B-UL/PC. The absence of activators in Mix B-UL/PC resulted in less gibbsite dissolving into the solution, hence less participation in the formation of phases and, consequently, more stable

phases compared to those in Mix H-UL/PC. Further discussion on the phases forming in Mix B-UL/PC is presented in Section 5.4.2 under phase identification.

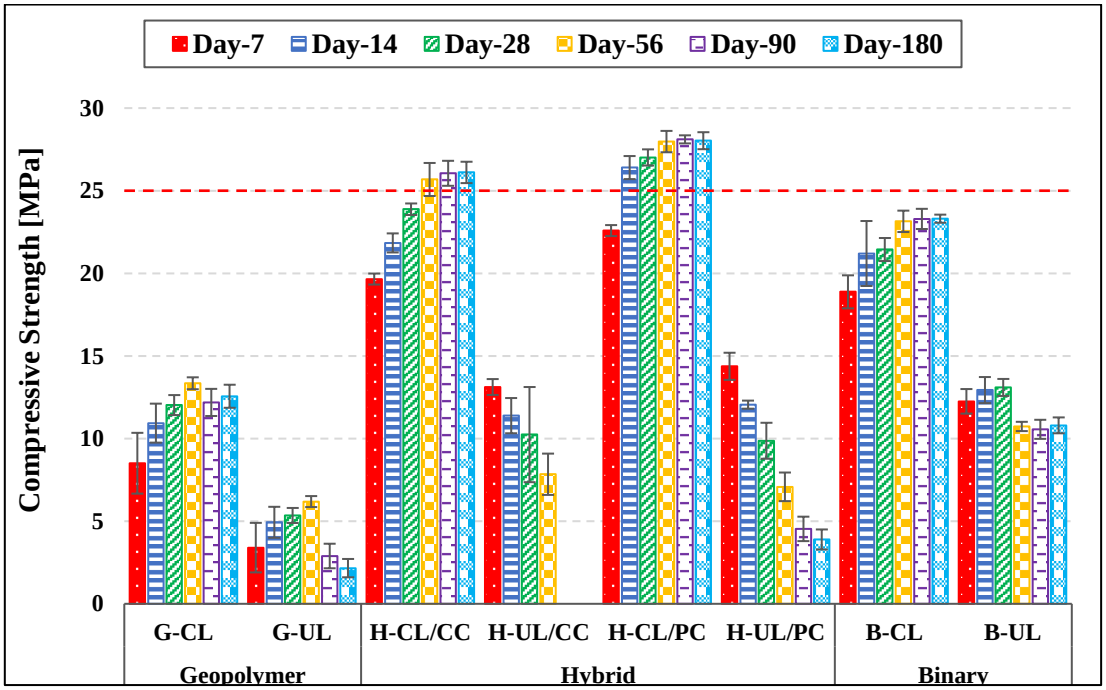

Figure 5.7: Compressive strength of the mixes.

Contrary to Gualtieri et al.'s [8] study, which reported no strength gain for the uncalcined laterite geopolymer mix even after prolonged curing at 60 ˚C in both acid and alkaline mediums, the uncalcined laterite geopolymer (Mix G-UL) in this study did display an improvement in strength with time, reaching up to 6.2 MPa by the 56th day. This difference can be attributed to the presence of gibbsite in significant quantity in the aluminium-rich laterite. It should be noted that for Gualtieri et al.'s study, the laterite used did not contain gibbsite but corundum, a very stable form of alumina.

Figure 5.8 shows cube samples of Mix H-UL/CC containing cracks at the age of 56 days. The cause of the crack formation, strength reduction, and subsequent disintegration can be attributed to the formation or transformation of crystalline phases. Further discussion on this topic is provided under the phase identification section. It is important to note that samples of Mix H-UL/CC also experienced severe efflorescence. However, at this stage, it cannot be directly linked to the disintegration, as all samples of the mixes containing calcium carbonate experienced severe efflorescence, and no strength reduction effects were observed in Mix H-CL/CC despite the severe efflorescence.



Figure 5.8: Cube samples of mix H-UL/CC after 56 days of casting.

5.4 Microstructural Analyses

5.4.1 Pore Structure and Porosity

5.4.1.1 Pore structure

The pore structure of the hardened paste was examined by studying the rate of isopropanol diffusion through the paste sample during the solvent exchange process. A high diffusion rate can be interpreted as the presence of larger pores or more extensive and interconnected pore networks. The results of the isopropanol diffusion rate for the mixes are presented in Figures 5.9 to 5.16, in unit weight per volume of the sample versus time, and the presented values are based on the average of three replicates. The results indicate that the rate of diffusion in calcined laterite mixes was generally lower than that in the uncalcined mixes across all categories, except for the mixes containing calcium carbonate, where the reverse was true. The isopropanol rate of diffusion was found to increase with age, particularly in the geopolymer mixes.

The secondary precursors appeared to have a limited impact on reducing the diffusion rate. In fact, an increase in the rate of isopropanol diffusion is observed in the hybrid mixes. Only Mix H-UL/CC exhibited a lower diffusion compared to the uncalcined mix of the geopolymer category. However, Mix H-UL/CC did disintegrate by the 56th day after casting. In terms of comparison, the calcined laterite mix containing Portland cement within the hybrid category displayed a lower diffusion rate than that of the calcium carbonate. Mix H-CL/CC displayed higher diffusion, increasing rapidly between the 56th and 180th day, and this can be ascribed to efflorescence. As early stated in Section 5.3, all the mixes containing calcium carbonate did

experience severe efflorescence. Figure 5.17 illustrates the severity of the efflorescence on Mix H-CL/CC samples at the age of 90 days.

For the binary mixes, the diffusion curves show a sharp increase in the first two hours, and this can be attributed to the rapid absorption of the isopropanol by the surfaces of the binary mix specimens since the binary mixes were not water-cured but cured under the same conditions at the geopolymer and hybrid mixes. Thus, instead of experiencing weight reduction after immersion in the isopropanol solution, the weight of the binary samples increased initially within the first hour before reducing. However, the binary mixes did display a much lower rate of diffusion compared to the hybrid mixes containing Portland cement.

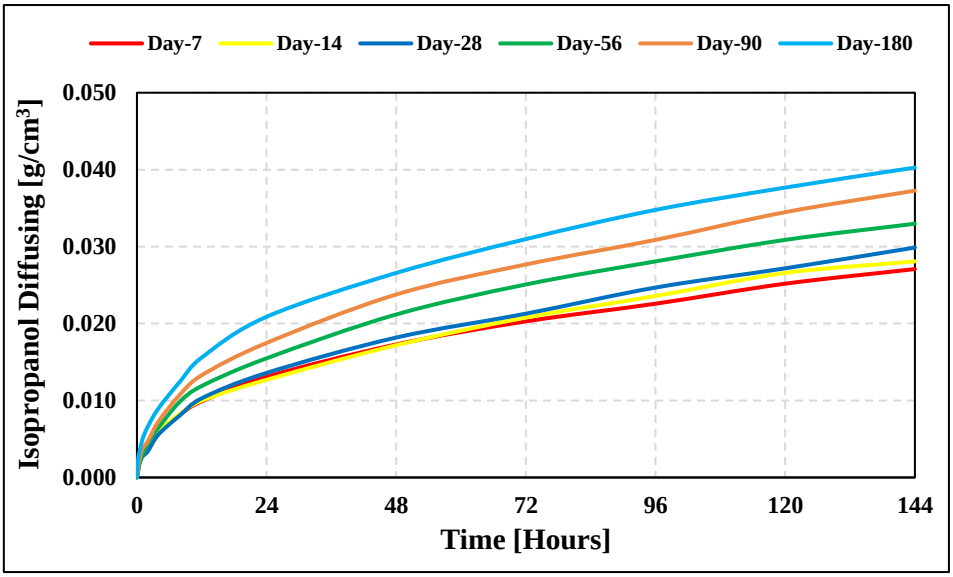

Figure 5.9: Isopropanol diffusion rate in paste samples of mix G-CL.

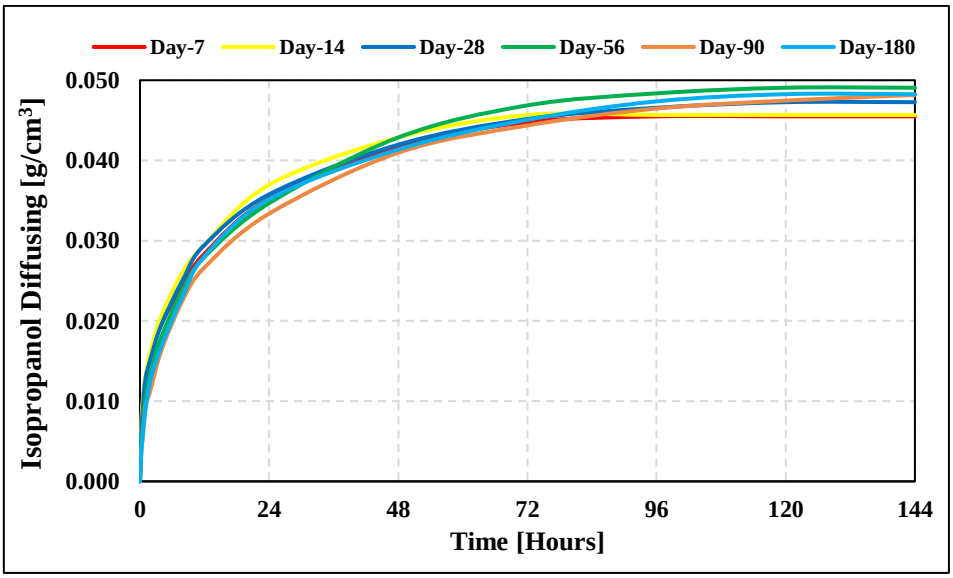

Figure 5.10: Isopropanol diffusion rate in paste samples of mix G-UL.

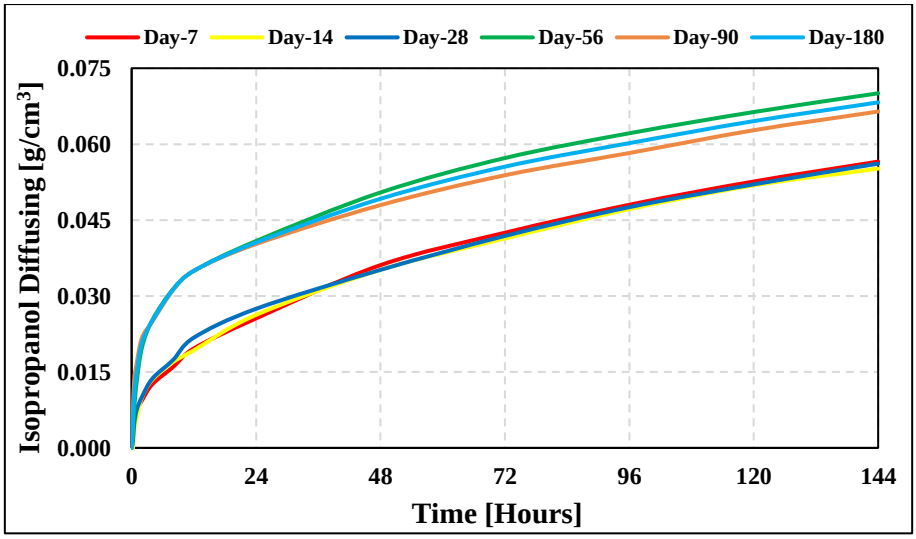

Figure 5.11: Isopropanol diffusion rate in paste samples of mix H-CL/CC.

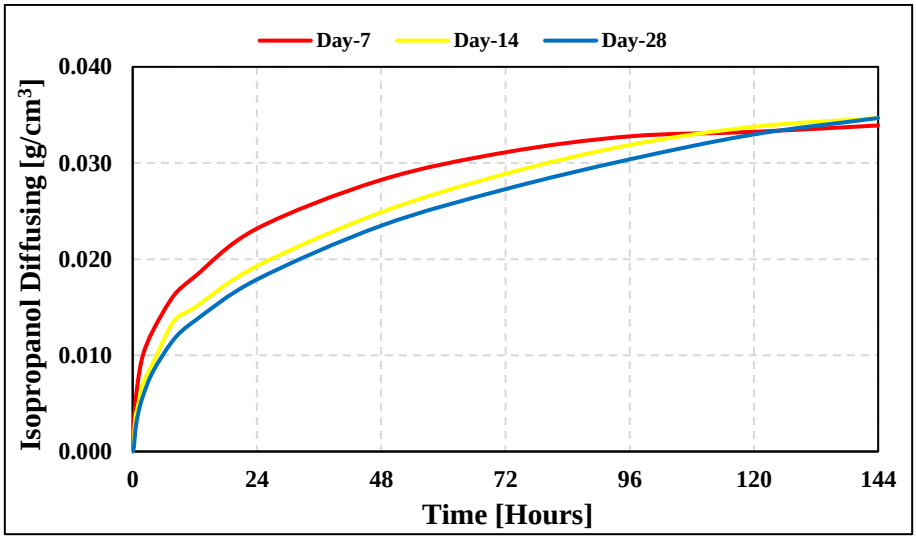

Figure 5.12: Isopropanol diffusion rate in paste samples of mix H-UL/CC.

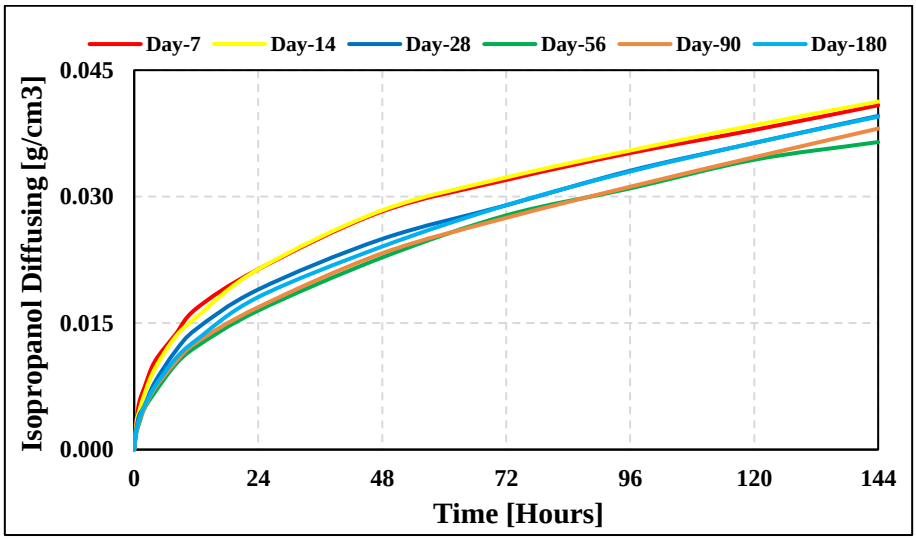

Figure 5.13: Isopropanol diffusion rate in paste samples of mix H-CL/PC.

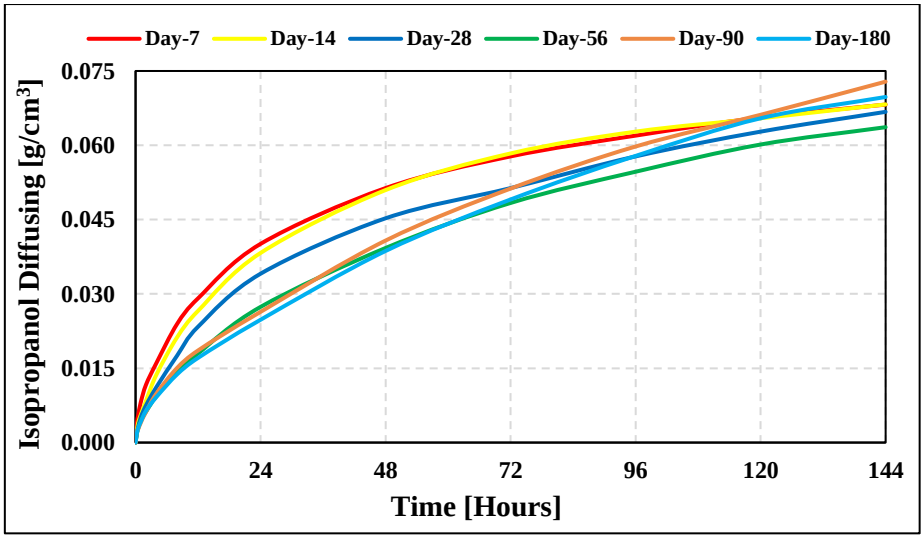

Figure 5.14: Isopropanol diffusion rate in paste samples of mix H-UL/PC.

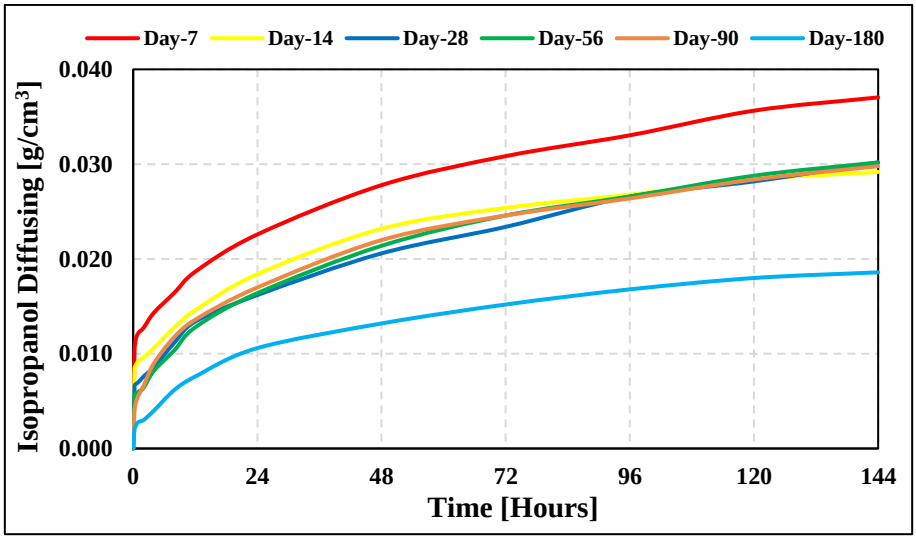

Figure 5.15: Isopropanol diffusion rate in paste samples of mix B-CL/PC.

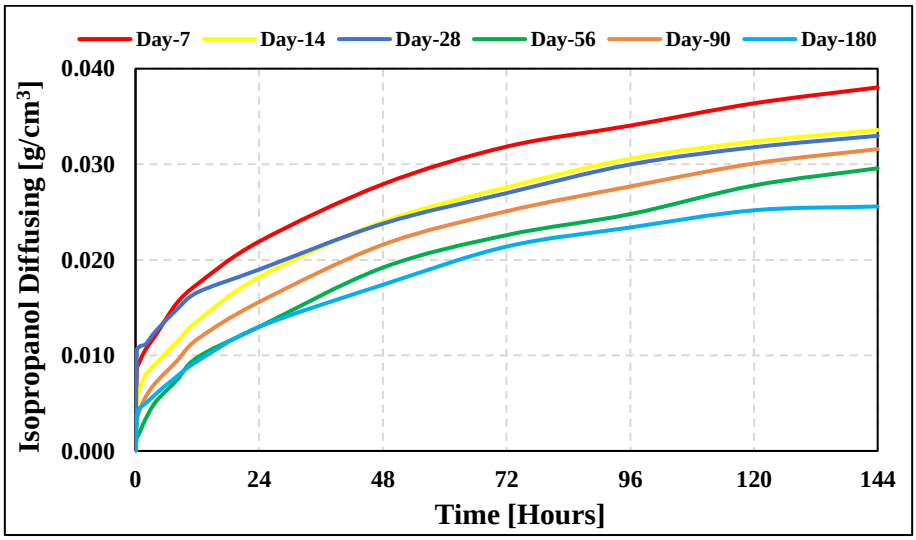

Figure 5.16: Isopropanol diffusion rate in paste samples of mix B-UL/PC.



Figure 5.17: Samples of mix H-CL/CC at 90 days after casting.

5.4.1.2 Porosity

The porosity of the samples was examined using the solvent exchange method and Helium Pycnometry. Two sets of porosities were obtained from the solvent exchange data: one based on the solvent-saturated mass and the other based on the initial mass of the samples. The general trends of the porosity results were consistent for all methods. However, the porosity determined by the helium pycnometer was the highest, while the one obtained by the solvent-saturated mass was the lowest, as the solvent was unable to penetrate smaller pores. Therefore, only these two results will be presented in this section. The presented data are based on the averages of three specimens and the error bars represent the confidence interval as described in Section 5.3.

Figures 5.18 and 5.19 present the porosity obtained by solvent exchange based on the solvent-saturated mass and helium pycnometry, respectively. The results indicate that samples of Mix H-CL/PC had the lowest porosity, while samples of G-UL and B-UL/PC exhibited the highest porosity in terms of solvent-saturated mass and helium pycnometry, respectively. For most of the mixes, porosity decreased initially before increasing with time. No relationship was observed between the porosity of the sample and the rate of isopropanol diffusion.

The inclusion of secondary precursors was found to reduce porosity, with Portland cement making the most significant contribution. However, the porosity of Mix H-CL/CC initially decreased, exhibiting porosity lower than its Portland cement counterpart, before increasing from the 28th day. The subsequent rise in porosity within Mix H-CL/CC can now be linked to the effects of efflorescence, as shown in Figures 5.20a and 5.20b. Figure 5.20a displays the isometric view of a 180-day-old paste specimen of Mix H-CL/CC experiencing efflorescence,

while Figure 5.20b shows the top view of the same specimen after some of the efflorescence has been removed. After removing the efflorescence, as shown in Figure 5.20b, an extensive network of cracks on the surface of the specimen becomes apparent, extending deep into the material. These cracks are not only linked to efflorescence but also to subflorescence. Subflorescence refers to the occurrence of efflorescence beneath the surface or within the specimen, which involves the reaction of sodium ions with CO_2 from the atmosphere, leading to the precipitation of crystallised sodium carbonate. The crystallisation of sodium carbonate within or beneath the surface of the specimen induces stress, causing structural damage, including cracks, scaling, and strength reduction [9–11]. The reduction in strength is also associated with the removal of alkalis from the geopolymer matrix due to both efflorescence and subflorescence [10,11].

Based on the evidence presented in this section, it can now be concluded that the increase in porosity, strength reduction, and subsequent cracking and disintegration of samples containing calcium carbonate can be ascribed to both efflorescence and subflorescence, which negatively affected the structural integrity of the material. Although the compressive strength of Mix H-CL/CC mortar seems not to be affected by severe efflorescence, the emergence of cracks and increased porosity in the paste sample of Mix H-CL/CC suggests that the structural integrity of Mix H-CL/CC was compromised. However, the steady compressive strength displayed can be attributed to better bonding between the paste and the fine aggregate in Mix H-CL/CC than in Mix H-UL/CC. Mortar samples of Mix-UL/CC displayed extensive cracks by the 56th day, and the paste samples completely disintegrated before the 56th day.

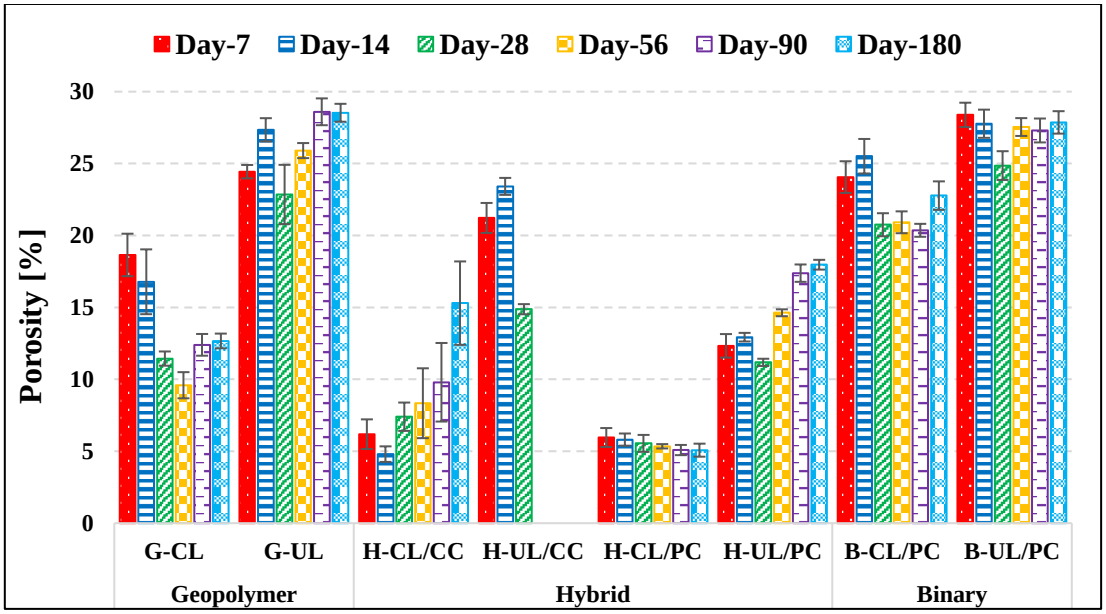

Figure 5.18: Porosity of the mixes obtained by Solvent Exchange.

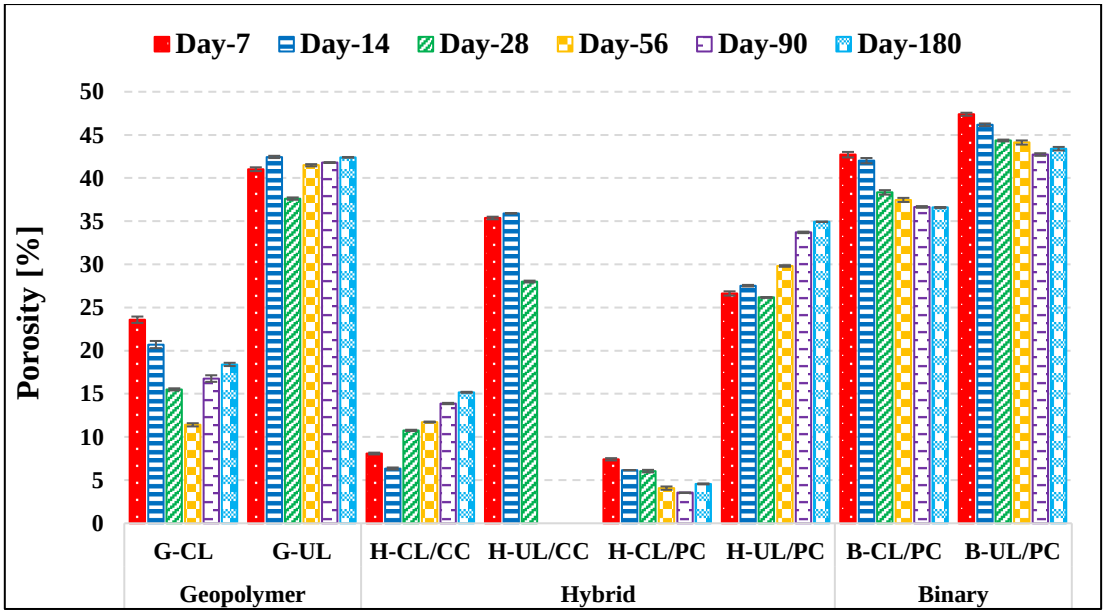

Figure 5.19: Porosity of the mixes obtained by Helium Pycnometry.

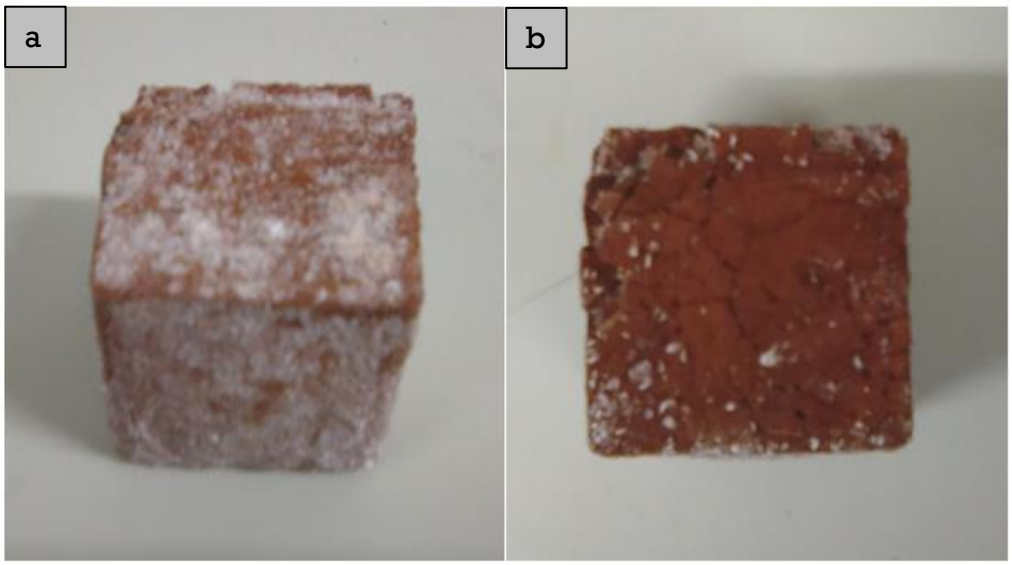

Figure 5.20: Sample of mix H-CL/CC at 180 Days: (a) Isometric view (b) Top view.

5.4.2 Phase Identification

5.4.2.1 X-ray Diffraction Analysis

Figures 5.21 to 5.28 present XRD diffractograms illustrating the crystalline phases identified in the mixes. The analysis revealed a distinct set of phases forming across the mix categories. The hybrid and binary mixes exhibited more complex phases, particularly in the uncalcined laterite series. In the calcined laterite series, quartz and hematite, the original mineral composition for the calcined laterite, remained constant across all categories, while in the uncalcined series, quartz was consistently present. The presence of these phases indicates that

they did not participate in the reactions, be it geopolymerisation or the hydration of Portland cement.

From the XRD patterns of the geopolymer mix made from calcined laterite (G-CL), as shown in Figure 5.21, only quartz and hematite were detected within the first 72 hours. It was only at Day-7 that a zeolitic phase, in the form of hydrosodalite, was identified in addition to quartz and hematite. The presence of these phases persisted up to 180 days after casting. Although the compressive strength of Mix G-CL started to decline after 56 days, no differences in the phase composition were detected between the 28th, 56th, and even up to the 180th day. However, the decline in strength could most likely be attributed to either an increase or decrease in the amount of crystalline phases. The absence of the formation of new phases within the first 72 hours clearly explains why Mix G-CL displayed the longest setting time and also supports the explanation provided in section 5.2.3 as to why Mix G-CL liberated the highest amount of heat.

Mix G-UL, on the other hand, exhibited a somewhat complex mineralogical evolution from an early age. The XRD patterns (Figure 5.22) of Mix G-UL displayed peaks for hematite, quartz, and sodium aluminate silicate hydrate in the form of hydrosodalite throughout the tested age. It is worth noting that, apart from quartz, the crystalline phases detected in Mix G-UL were not present in the uncalcined laterite. The initial mineral composition of the uncalcined laterite included quartz, gibbsite, goethite, and kaolinite. However, upon activation, gibbsite, goethite, and kaolinite disappeared, suggesting the occurrence of reactions including geopolymerisation.

The appearance of hydrosodalite signifies the reaction of kaolinite and, in particular, gibbsite with hydroxide and silica ions, as discussed in Section 5.2.1. Meanwhile, the presence of hematite implies the transformation of goethite to hematite, which seems somewhat unusual, as such transformations usually occur under thermal conditions. However, it should be noted that goethite also has a high affinity for hydroxide ions, and in the presence of silica species, this possibility cannot be ruled out. One plausible explanation is that goethite [FeO(OH)] reacted with hydroxide and sodium ions, releasing water and forming sodium ferrite (Na_2FeO_2), as illustrated in Equation 5.4. Subsequently, this sodium ferrite reacts with the silicate species present in the solution, leading to the formation of hematite as expressed in Equations 5.5.

$$FeO(OH) + 2Na^+ + 2OH^- \rightarrow Na_2FeO_2 + 2H_2O \qquad \text{Equation -------5.4}$$

$$2Na_2FeO_2 + 2SiO_4^{4-} \rightarrow Fe_2O_3 + 2Na_2SiO_3 \qquad \text{Equation -------5.5}$$

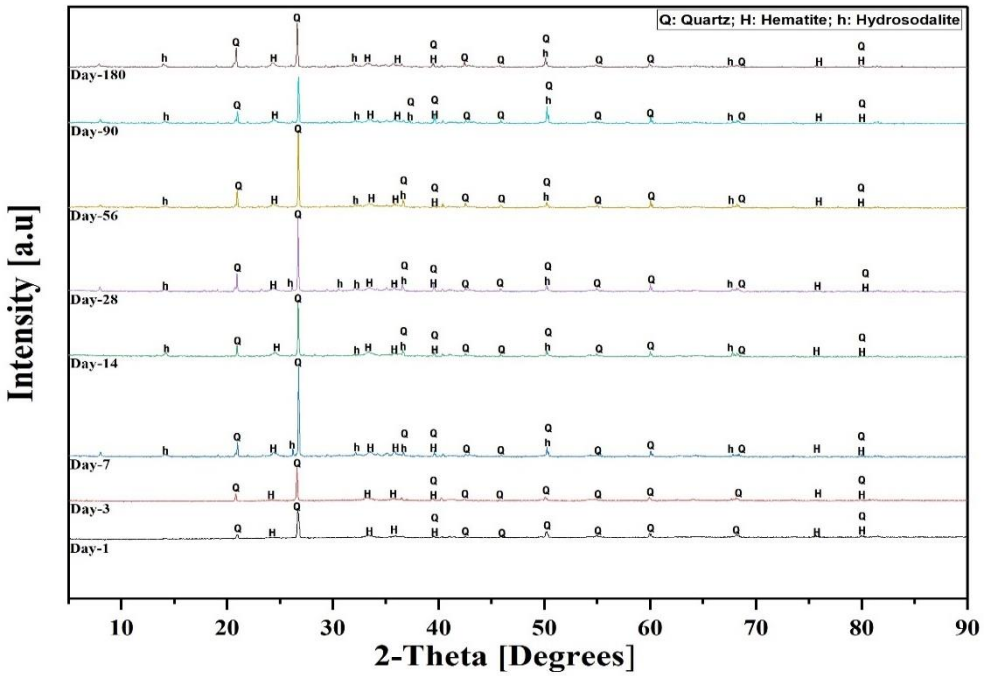

Figure 5.21: XRD spectra of mix G-CL.

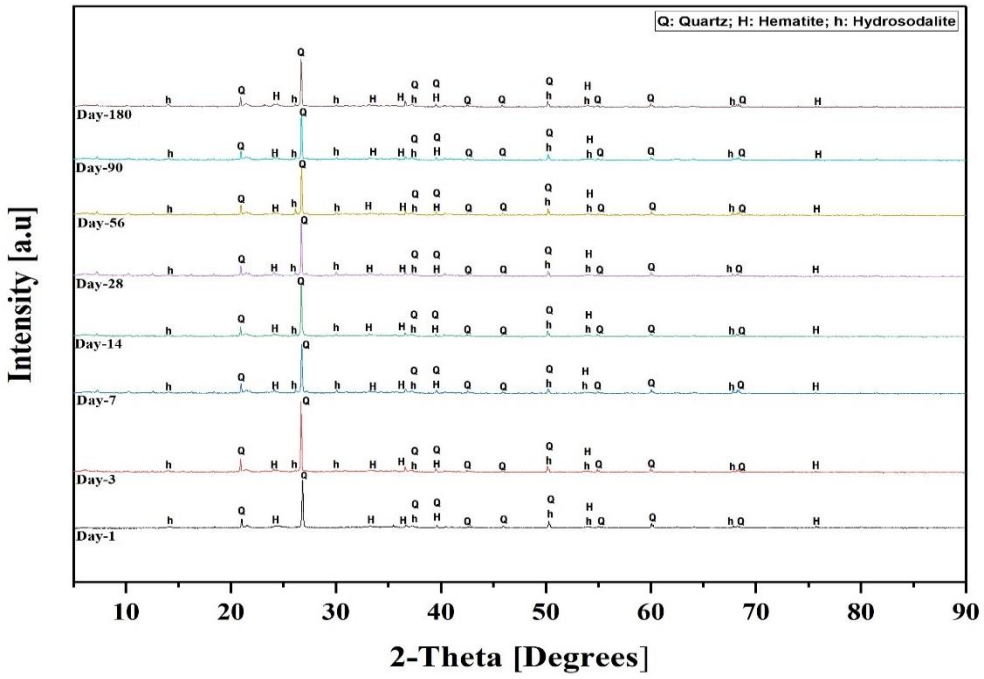

Figure 5.22: XRD spectra of mix G-UL.

In the presence of secondary precursors, both the calcined and uncalcined laterite behave differently. In Mix H-CL/CC, quartz, hematite, calcite, and thermonatrite, a hydrated sodium carbonate, were identified as early as 24 hours after casting. The presence of calcite indicates unreacted calcium carbonate, while the presence of thermonatrite suggests the decomposition of calcite into calcium oxide (CaO) and carbon dioxide (CO_2) in the alkaline environment,

leading to the formation of hydrated sodium carbonate ($Na_2CO_3 \cdot H_2O$). Although the XRD did not detect calcium oxide, it may have reacted with silicate species present in the solution to form amorphous or poorly crystallised calcium silicate hydrate (C-S-H), which is undetectable by XRD, contributing to strength development. The formation of C-S-H at an early age could be linked to the shorter setting times, higher early strength, and denser microstructure exhibited by Mix H-CL/CC compared to Mix G-CL. This justifies why most of the strength gained occurred within the first 7 days after casting. It is interesting to note that no crystalline zeolitic phases were detected in Mix H-CL/CC, as shown in 5.23.

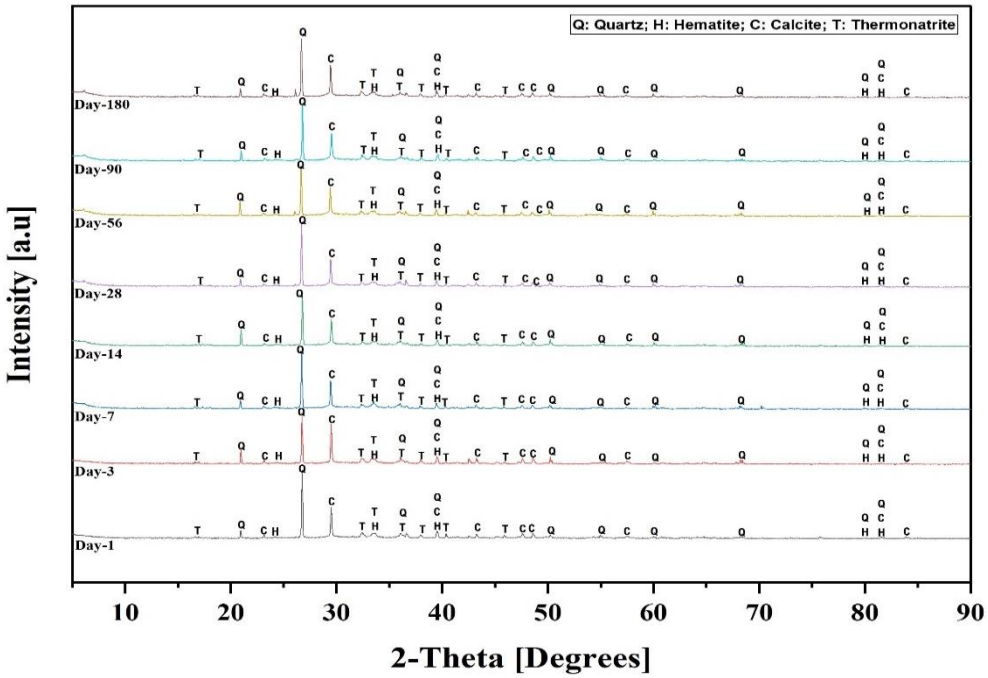

Figure 5.23: XRD spectra of mix H-CL/CC.

For the hybrid mix based on uncalcined laterite and calcium carbonate (Mix H-UL/CC), the XRD patterns shown in Figure 5.24 reveal peaks of quartz, calcite, and thermonatrite as of Day-1. These phases remain constant up to the 28th day of testing before the paste samples of Mix H-UL/CC disintegrated. Following disintegration, the same phases were also identified in the 56th-day disintegrated sample of Mix H-UL/CC. Similar to Mix H-CL/CC, no crystalline zeolitic phases were detected in Mix H-UL/CC, suggesting that the presence of calcium carbonate led to the formation of amorphous sodium aluminate silicate hydrate (N-A-S-H).

The presence of thermonatrite and calcite, as well as the absence of crystalline zeolitic phases, appears unique to the mixes containing calcium carbonate. Although there is a larger amount of residual calcium carbonate in the geopolymers made with calcium carbonate, its presence contributed to strengthening the geopolymer matrix and densifying the microstructure from an

early age, or at least before the effects of efflorescence and subflorescence set in. Despite the effects of efflorescence and subflorescence, no formation of new crystalline phases was observed. These results align with the findings of Zhang et al. [11], which stated that efflorescence does not alter the mineralogical characteristics of a geopolymer gel. The causes of strength reduction, cracks, increased porosity, and subsequent disintegration of samples containing calcium carbonate have been attributed to efflorescence and subflorescence and discussed in Section 5.4.1.2. The efflorescence in the mixes containing calcium carbonate is primarily due to the substantial amount of unreacted calcium carbonate, which leaves more unbound sodium ions to react with atmospheric CO_2.

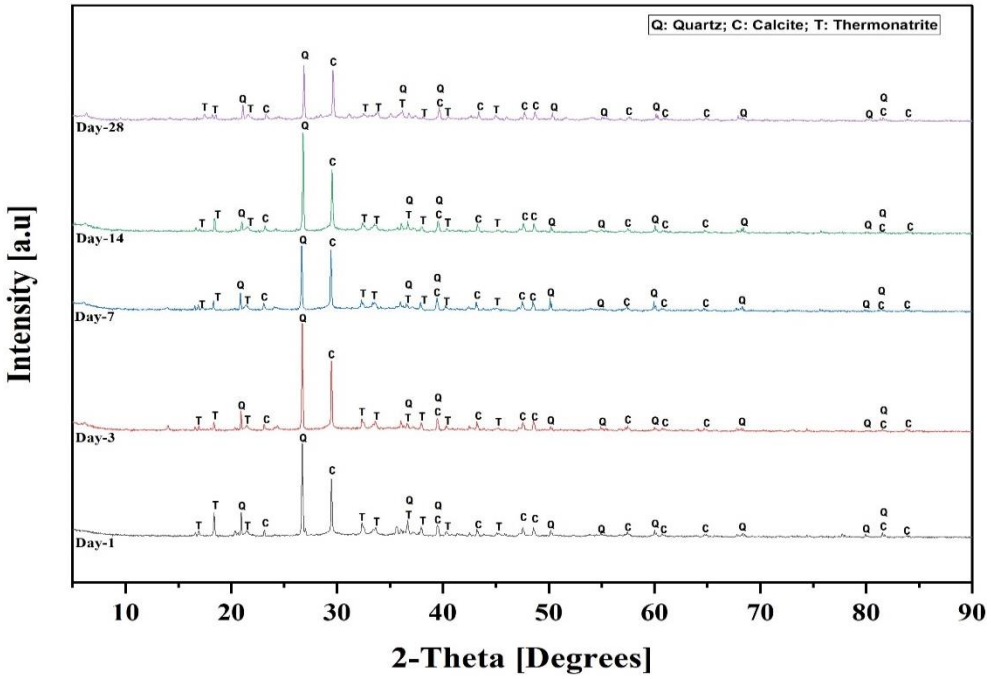

Figure 5.24: XRD spectra of mix H-UL/CC.

In Mix H-CL/PC, a constant set of phases was identified throughout the tested ages, as shown in Figure 5.25. Alongside quartz and hematite, which remained consistent across the calcined laterite series, crystalline calcium silicate hydrate (C-S-H) was detected as early as Day-1 and persisted up to 180 days after casting. The formation of C-S-H resulted from the reaction of the alite (C_3S) and belite (C_2S) phases of Portland cement. Since this reaction occurred in a highly alkaline environment, C-S-H incorporated sodium ions, identified in XRD analysis as sodium calcium silicate hydrate (C-(N)-S-H), hence the early strength gain and short setting times of Mix H-CL/PC. Remarkably, no portlandite [$Ca(OH)_2$] was detected in this system, even at an early age. The absence of portlandite suggests that $Ca(OH)_2$ reacted with the soluble silicates in the solution to form additional C-(N)-S-H.

Similarly, for the hybrid mix based on uncalcined laterite and Portland cement, the same set of phases identified at Day-1 persisted throughout the testing period, as represented in Figure 5.26. However, the phases identified were different from those of Mix H-CL/PC. In addition to quartz, chabazite [$(Ca, Na_2)Al_2Si_4O_{12}\cdot 6H_2O$] and hydrated andradite [$Ca_3Fe_2(SiO_4)_3\cdot x(OH)_{4x}$] were detected in Mix H-UL/PC. Chabazite is a zeolitic mineral, while andradite is a member of the garnet group composed of calcium iron silicate.

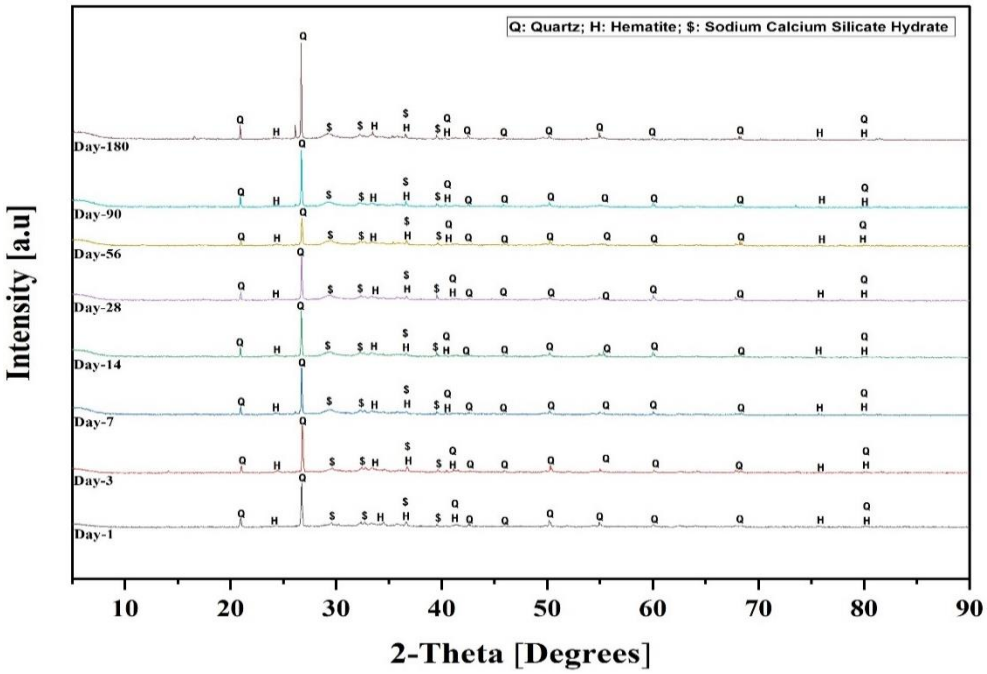

Figure 5.25: XRD spectra of mix H-CL/PC.

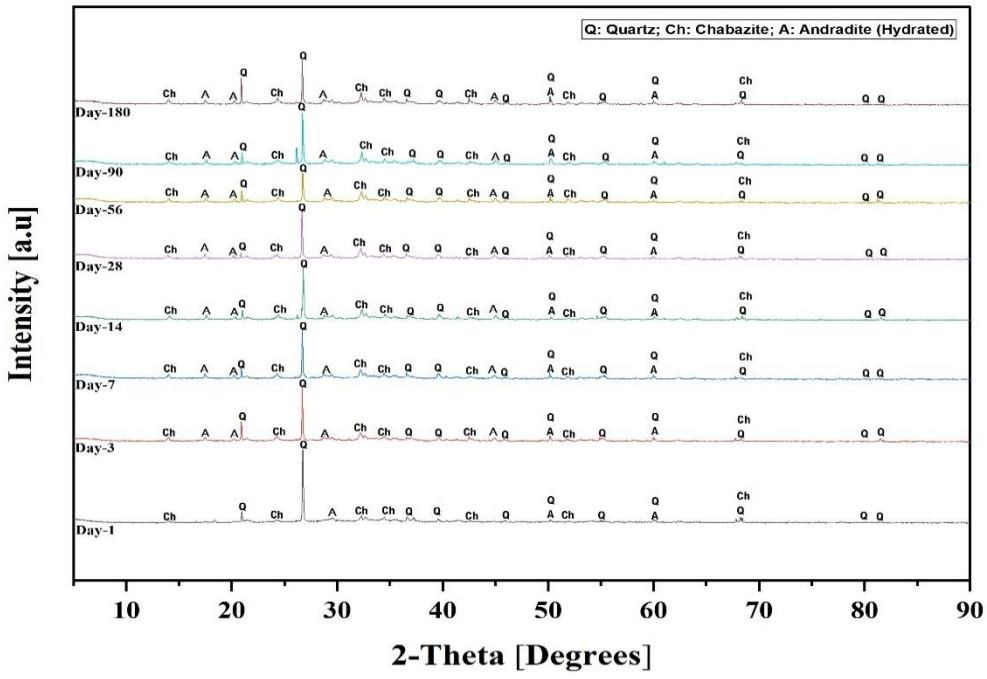

Figure 5.26: XRD spectra of mix H-UL/PC.

The phases in the binary mixes were primarily influenced by the presence of Portland cement, as presented in Figure 5.27 and Figure 5.28, respectively, for Mix B-CL/PC and Mix B-UL/PC. In Mix B-CL/PC, alongside the unreactive phases of calcined laterite (quartz and hematite), C_3S and C_2S were detected at Day-1. By Day-3, portlandite emerged in addition to C_3S and C_2S, which disappeared by Day-7. Portlandite persisted up to the 28th day, and by the 56th day, portlandite had been consumed. However, no crystalline C-S-H was detected in Mix B-CL/PC.

In Mix B-UL/PC, in addition to the unreacted phases of Portland cement, gibbsite was detected from an early age and persisted throughout the testing period. This suggests that gibbsite is highly stable in the presence of calcium hydroxide compared to sodium hydroxide. However, goethite was undetectable, indicating that goethite has a stronger attraction for hydroxide ions compared to gibbsite.

Similarly, as in the case of Mix B-CL/PC, C_3S and C_2S disappeared by the 7th day, although portlandite persisted for a more extended period. The disappearance of portlandite coincided with the emergence of katoite. Katoite is a mineral that belongs to the garnet group and is also part of the subgroup called hydrogrossular garnet. This mineral mainly consists of calcium, aluminium, and silicate. The emergence of katoite could be associated with the reaction of portlandite and kaolinite in the uncalcined laterite. It is worth noting that no zeolitic phase was observed in the binary mixes, given the absence of activators.

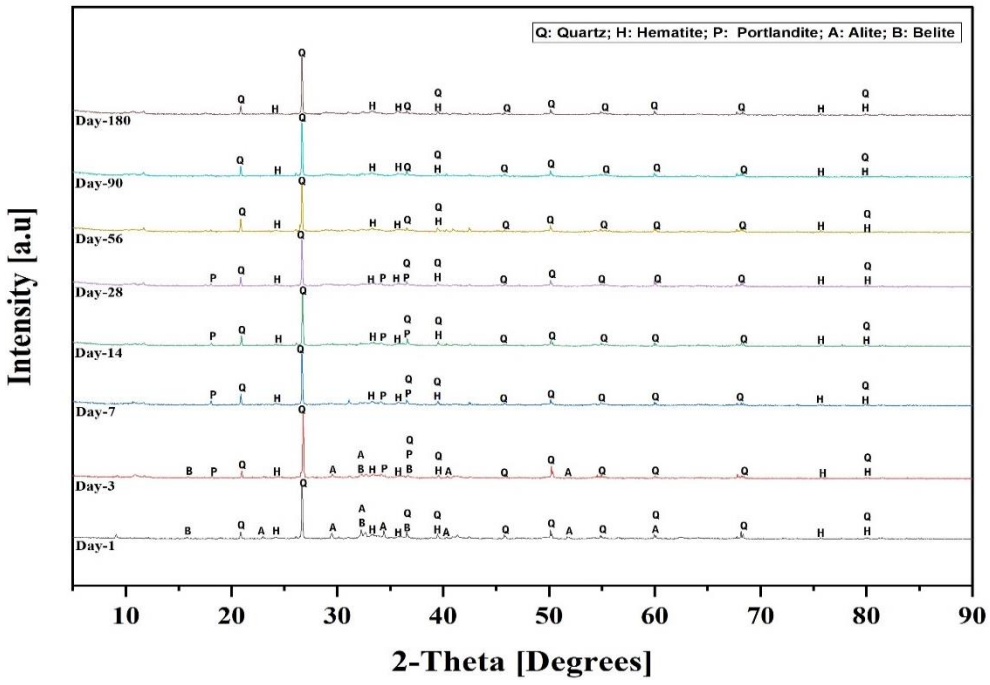

Figure 5.27: XRD spectra of mix B-CL/PC.

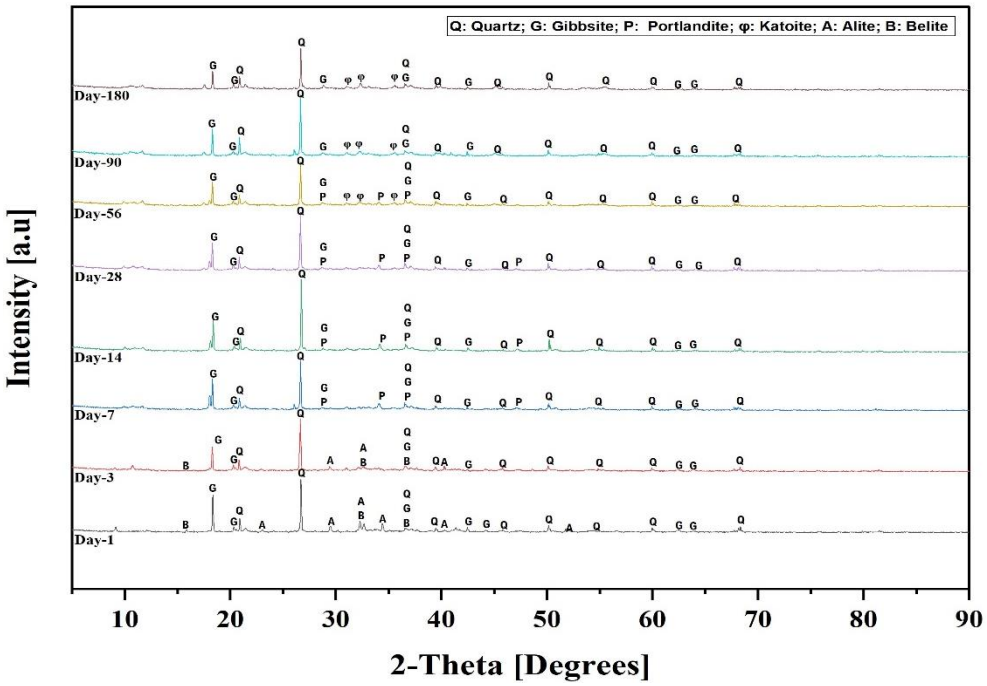

Figure 5.28: XRD spectra of mix B-UL/PC.

5.4.2.2 Fourier Transform Infrared Spectroscopy

The FTIR spectra presented in Figure 5.29 to Figure 5.36 provide additional insights into the composition of the mixes in terms of phase assemblage. The results of the FTIR analysis not only support the findings from XRD analysis but also offer complementary information, particularly in identifying phases that were not detectable by XRD.

For instance, in Figure 5.29, the FTIR analysis revealed the presence of hydrosodalite in the G-CL mix as early as Day-1. However, the peaks became broader by Day-7, possibly explaining why XRD only detected the hydrosodalite phase on the 7th day after casting. In the case of Mix-GUL, the FTIR spectra in Figure 5.30 displayed similar peaks to Mix G-CL, confirming the presence of quartz, hematite, and hydrosodalite.

In Figure 5.29, the peak at 3676 cm^{-1} corresponds to the OH stretching vibration in hydrosodalite, while 960, 896, and 776 cm^{-1} represent Si-O-Al bonds found in hydrosodalite. Similarly, in Figure 5.30, the 3676 cm^{-1} peak indicates the OH stretching vibration in hydrosodalite, while 960, 798, and 662 cm^{-1} correspond to Al-O-Si vibrations of hydrosodalite. The peaks at 838 and 688 cm^{-1} and 728 and 550 cm^{-1} correspond to Fe-O in hematite, respectively, in Mix G-CL and Mix G-UL. The remaining peaks in the region below 500 cm^{-1} can be attributed to either Si-O or Al-O vibrations. It should be noted that the Si-O-Al bond is often represented as Si-O-T, where “T” stands for tetrahedral coordination involving Si or any element, such as Al and Fe, that can substitute Si in tetrahedral coordination [12].

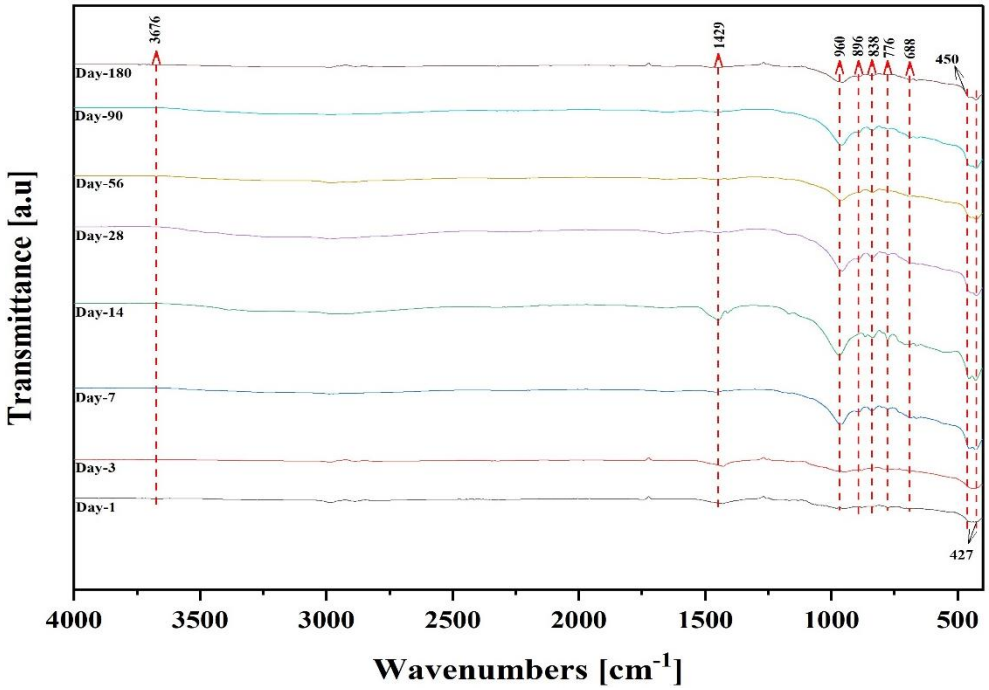

Figure 5.29: FTIR spectra of mix G-CL.

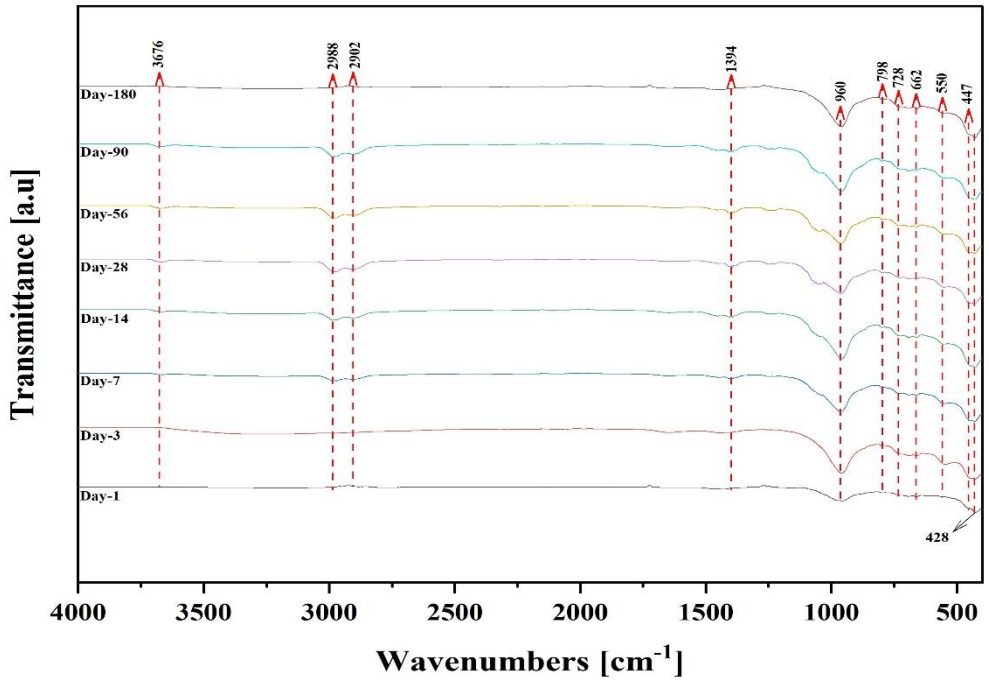

Figure 5.30: FTIR spectra of mix G-UL.

Besides the initial constituent minerals of the laterites, calcite (residual calcium carbonate) and thermonatrite were identified as crystalline phases through XRD analysis. However, as illustrated in Figures 5.31 and 5.32, the FTIR analysis of Mix H-CL/CC and Mix H-UL/CC reveals peaks of Si-O-Al at 960, 956, 869, and 668 cm^{-1}. These peaks suggest the presence of an amorphous zeolitic phase incorporating calcium or an amorphous C-S-H or C-A-S-H, as would be expected in the case of uncalcined laterite due to the abundance of gibbsite.

Calcite and thermonatrite share the same molecular bond of CO_3^{2-}. The only distinguishing feature is the water molecule, which reflects bands of OH stretching vibrations in the region of 3200 to 3600 cm^{-1}. The peaks between 1482 and 1414 cm^{-1}, as shown in Figures 5.31 and 5.32, are caused by the stretching vibration of CO_3^{2-}, while those at 869, 868, 714 and 710 cm^{-1} are caused by the bending vibrations of CO_3^{2-} in calcite and thermonatrite [13,14]. The absence of an OH band in the functional group region suggests a relatively weak bonding of the water molecule, as weaker bonds generally result in less pronounced peaks in FTIR analysis.

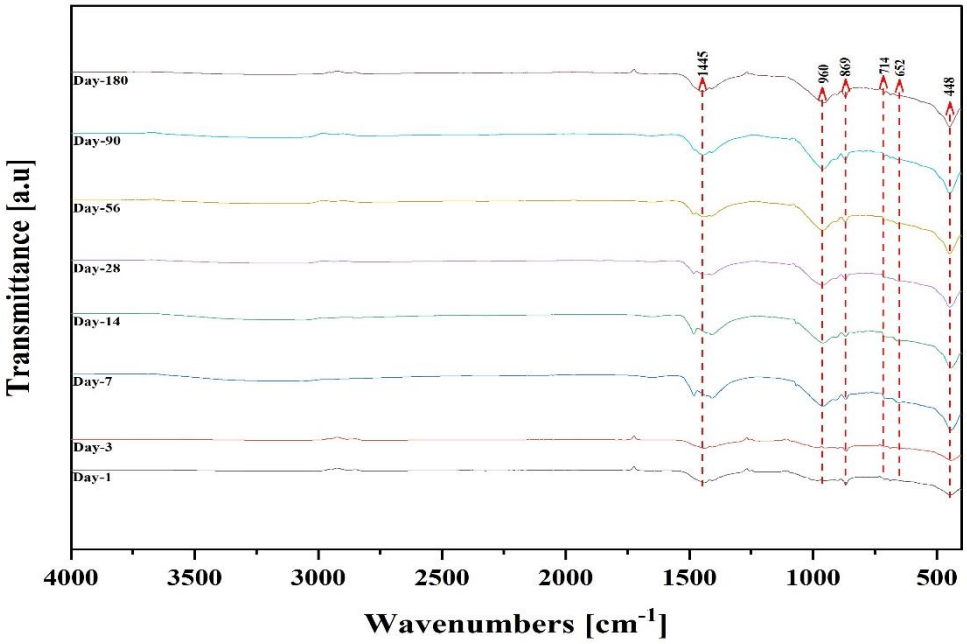

Figure 5.31: FTIR spectra for mix H-CL/CC.

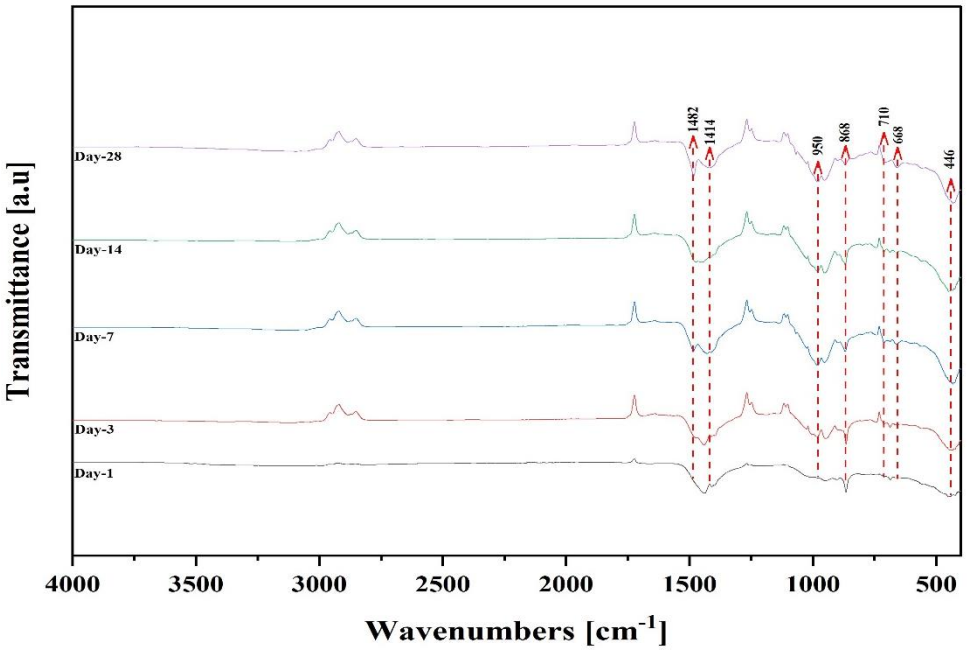

Figure 5.32: FTIR spectra of mix H-UL/CC.

For the hybrid mix containing calcined laterite and Portland cement (Mix H-CL/PC), the FTIR transmittance peaks of interest are 937, 896, 815, 686, and 432 cm^{-1}. The peaks at 937, 896, and 686 cm^{-1}, which reflect the Si-O-T bonds, correspond to the sodium calcium silicate hydrate identified in the XRD analysis. The remaining peaks, as depicted in Figure 5.33, are characteristic of Fe-O and Si-O bonds. It should be noted that peaks within the 1482 – 1390 cm^{-1} range in most of the FTIR spectra are caused by CO_3^{2-} vibrations, resulting from the reaction of atmospheric CO_2 with unbound alkalis [15,16]. Meanwhile, peaks between 2880 – 3000 cm^{-1} are caused by vibrations of C-H bonds, which relate to the isopropanol used in the solvent exchange. The presence of C-H bonds indicates that the drying process did not completely remove or desorb the isopropanol from the specimen surfaces.

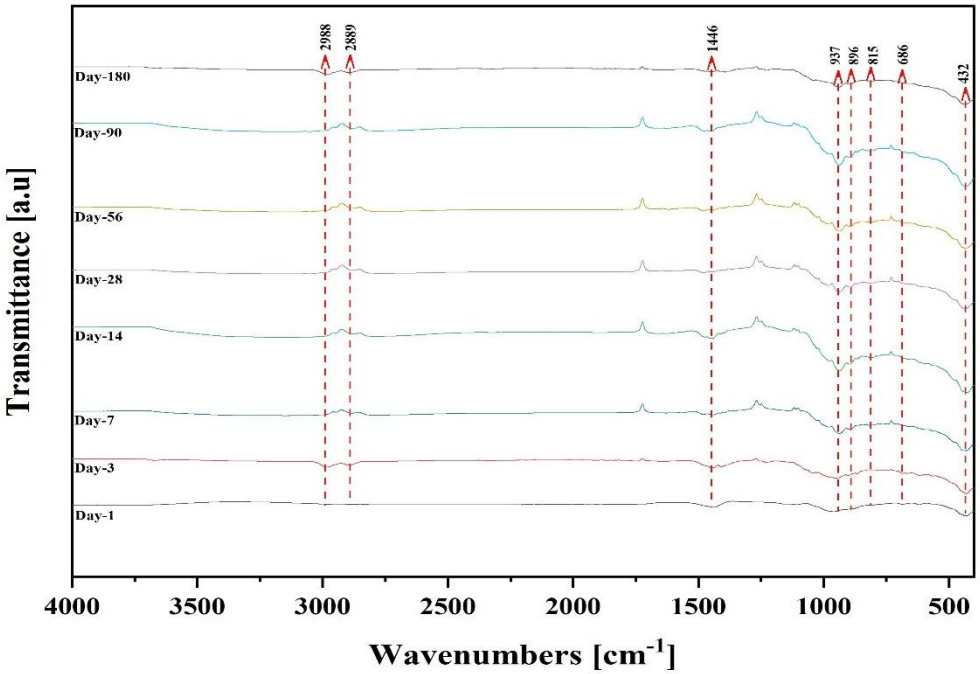

Figure 5.33: FTIR spectra of mix H-CL/PC.

The FTIR analysis of Mix H-UL/PC, presented in Figure 5.34, confirms the presence of andradite and chabazite. The peaks at 1100, 956, and 662 cm^{-1} correspond to the Si-O-T vibrations in chabazite, while 800 and 602 cm^{-1} are associated with the Fe-O and Ca-O, respectively, in andradite. Although andradite was detected as hydrated andradite by the XRD, and chabazite also has a water molecule attached, there were no OH vibrations in the FTIR spectra of Mix H-UL/PC. This indicates that the water molecules were weakly bonded in both chabazite and andradite. It is important to emphasize that the amorphous C-S-H forming in the mixes containing calcium carbonate, as well as the thermonatrite, did not exhibit any OH absorption or transmittance peaks.

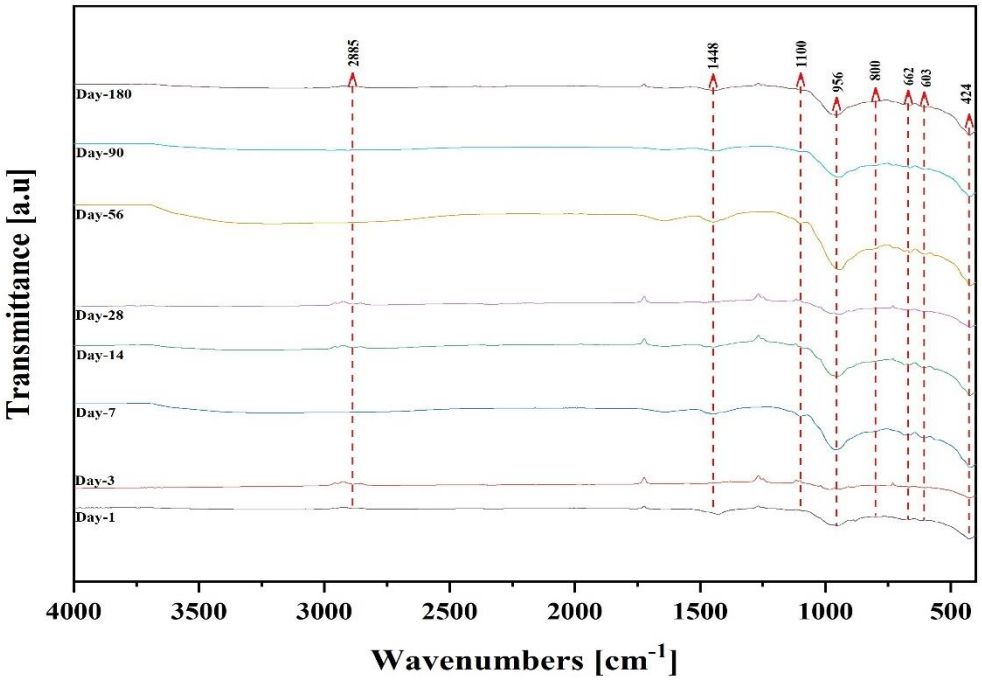

Figure 5.34: FTIR spectra of mix H-UL/PC.

For Mix B-CL/PC, the FTIR spectra shown in Figure 5.35 reveal the presence of the amorphous phase that was not detected by the XRD. The peaks at 956, 872, and 776 cm^{-1} are attributed to Si-O-T vibrations, and the stretching vibration at 3669 cm^{-1} is caused by water molecules. Given that this mix contained only Portland cement as the reactive ingredient, this phase can be identified as calcium silicate hydrate (C-S-H).

Also, for Mix B-UL/PC, the FTIR analysis confirms the presence of quartz, gibbsite, and katoite. In the functional group region, as depicted in Figure 5.36, the OH stretching vibration at 3676 cm^{-1} corresponds to katoite, while the peaks at 3527 and 3376 cm^{-1} are associated with gibbsite. Interestingly, these were the exact same peaks assigned to gibbsite in the as-received and milled laterite (uncalcined). This confirms the nonparticipation of gibbsite in the reaction or the formation of phases in Mix B-UL/PC. Given the stability in terms of strength retrogression or the slight decline shown by Mix B-UL/PC compared to the other mixes within the uncalcined laterite series, it can be concluded that the participation of gibbsite in phase formation is the cause of the unstable phases in the uncalcined laterite mixes.

In the fingerprint region, the peaks at 1242, 1046, and 662 cm^{-1} correspond to the stretching and bending vibrations of Si-O-T bonds in katoite. Other peaks, such as 979 and 420 cm^{-1}, are associated with Al-O and Si-O bonds, respectively, while 516 cm^{-1} is linked to the Ca-O bond. The peak at 1394 cm^{-1}, as previously stated, is associated with CO_3^{2-}, caused by the reaction of atmospheric CO^2 with unbound alkalis.

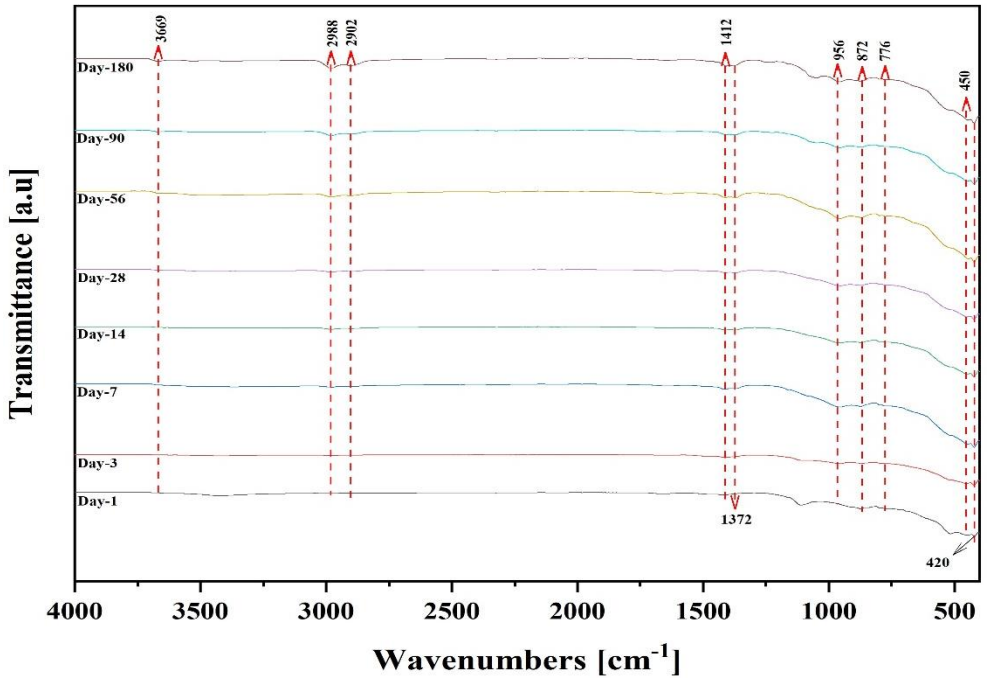

Figure 5.35: FTIR spectra of mix B-CL/PC.

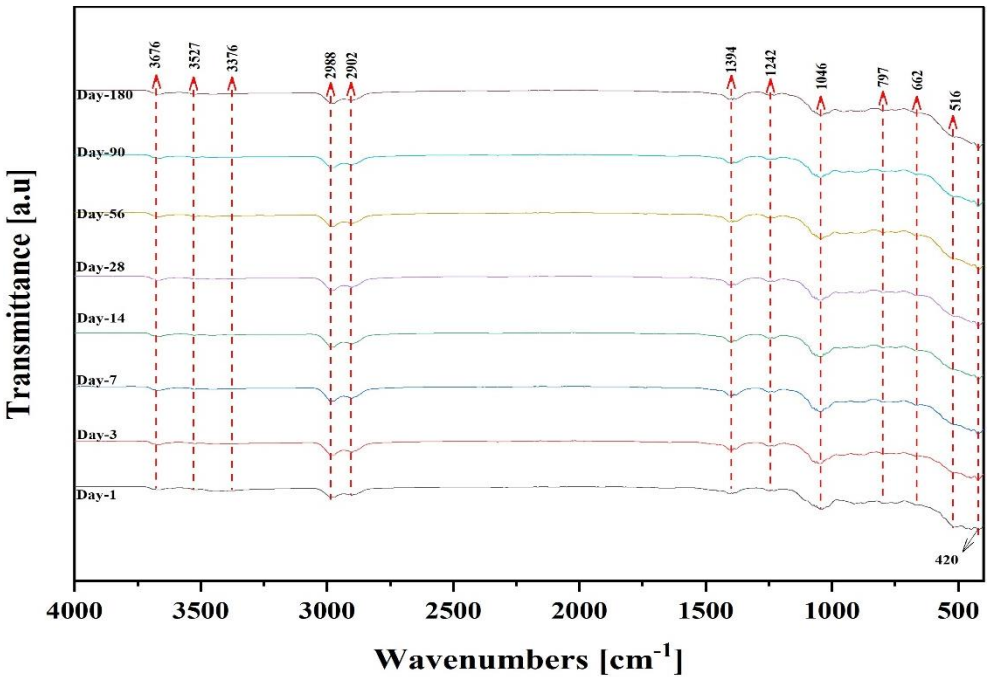

Figure 5.36: FTIR spectra of mix B-UL/PC.

5.5 Summary

The findings of the laboratory investigation, which examined the fresh and hardened properties of geopolymers derived from aluminium-rich laterite and derivatives containing calcium minerals, have been presented in this chapter. The flow behaviour of the paste was found to be controlled by the viscosity of the activating solution, a factor dependent on temperature. The

geopolymer mix based on calcined laterite (Mix G-CL) exhibited the longest setting time among all mixes, while Mix G-UL displayed the shortest within the geopolymer category. The addition of calcium minerals did reduce the setting time, with calcium carbonate resulting in shorter setting times in the uncalcined laterite, while Portland cement was effective in the calcined laterite. Mix G-CL also displayed the highest amount of heat liberated of all mixes, while Mix G-UL displayed the lowest.

Both calcium carbonate and Portland cement were found to increase the rate of heat liberation within the first hour of the isothermal calorimetry test. All mixes within the calcined laterite series exhibited higher compressive strength than their uncalcined counterparts. However, only the calcined laterite mixes containing calcium minerals were able to obtain structural strength. All mixes within the uncalcined laterite series experienced strength regressions, with samples of the uncalcined laterite mix containing calcium carbonate disintegrating by the 56th day after casting. Surprisingly, samples of the binary category displayed compressive strength comparable to the hybrid category despite the absence of activators.

The microstructural examinations revealed that the porosity, pore structure, and phase assemblage were influenced by the type of laterite and the presence of calcium carbonate or Portland cement. The addition of calcium carbonate also resulted in severe efflorescence and subflorescence, negatively impacting the porosity, resistance to penetration, and structural integrity of the microstructure. In the absence of activators, as demonstrated by the binary mixes, more stable phases were observed in Mix B-UL/PC compared to those formed in the other mixes within the uncalcined laterite series.

5.6 References

1. Nwaubani, S.O., Properties, Hydration and Durability of Pozzolanic Mortars and Concretes, PhD Thesis, Univerity of Leeds (Department of Civil Engineering), (1990).
2. Kaze, R.C., Beleuk à Moungam, L.M., Fonkwe Djouka, M.L., Nana, A., Kamseu, E., Chinje Melo, U.F., Leonelli, C., The Corrosion of Kaolinite by Iron Minerals and the Effects on Geopolymerization, *Applied Clay Science*. (2017) **138** 48–62.
3. Metekong, J.V.S., Kaze, C.R., Adesina, A., Nemaleu, J.G.D., Djobo, J.N.Y., Lemougna, P.N., Alomayri, T., Kamseu, E., Melo, U.C., Tatietse, T.T., Influence of Thermal Activation and Silica Modulus on the Properties of Clayey-Lateritic Based Geopolymer Binders Cured at Room Temperature, *Silicon*. (2022) **14** 7399–7416.

4. Kaze, C.R., Lecomte-Nana, G.L., Adesina, A., Nemaleu, J.G.D., Kamseu, E., Chinje Melo, U., Influence of Mineralogy and Activator Type on the Rheology Behaviour and Setting Time of Laterite Based Geopolymer Paste, *Cement and Concrete Composites*. (2022) **126** 104345.
5. Zhao, Y., Duan, Y., Zhu, L., Wang, Y., Jin, Z., Characterization of Coarse Aggregate Morphology and Its Effect on Rheological and Mechanical Properties of Fresh Concrete, *Construction and Building Materials*. (2021) **286** 122940.
6. Wadso, L., Winnefeld, F., Riding, K.A., Sandberg, P., Calorimetry, In: *A Practical Guide to Microstructural Analysis of Cementitious Materials*, CRC Press, (2016).
7. BS EN 206, Concrete - Specification, Performance, Production and Conformity, (2013).
8. Gualtieri, M.L., Romagnoli, M., Pollastri, S., Gualtieri, A.F., Inorganic Polymers from Laterite Using Activation with Phosphoric Acid and Alkaline Sodium Silicate Solution: Mechanical and Microstructural Properties, *Cement and Concrete Research*. (2015) **67** 259–270.
9. Marzal, R.M.E., Franke, L., Deckelmann, G., Predicting Efflorescence and Subflorescences of Salts, *MRS Online Proceedings Library*. (2008) **1047** 403.
10. Yao, X., Yang, T., Zhang, Z., Compressive Strength Development and Shrinkage of Alkali-Activated Fly Ash–Slag Blends Associated with Efflorescence, *Materials and Structures*. (2016) **49** 2907–2918.
11. Zhang, Z., Provis, J.L., Ma, X., Reid, A., Wang, H., Efflorescence and Subflorescence Induced Microstructural and Mechanical Evolution in Fly Ash-Based Geopolymers, *Cement and Concrete Composites*. (2018) **92** 165–177.
12. Derouane, E.G., Fripiat, J.G., Quantum Mechanical Calculations on Molecular Sieves. 1. Properties of the Si-O-T (T = Si, Al, B) Bridge in Zeolites, *The Journal of Physical Chemistry*. (1987) **91** 145–148.
13. Chukanov, N.V., Infrared spectra of mineral species: Extended library, Springer Science & Business Media, (2013).
14. Chukanov, N.V., Chervonnyi, A.D., Infrared Spectroscopy of Minerals and Related Compounds, Springer, (2016).
15. Wan, Q., Rao, F., Song, S., García, R.E., Estrella, R.M., Patiño, C.L., Zhang, Y., Geopolymerization Reaction, Microstructure and Simulation of Metakaolin-Based Geopolymers at Extended Si/Al Ratios, *Cement and Concrete Composites*. (2017) **79** 45–52.

Chapter 6

Conclusions and Recommendations

6.1 Introduction

This study aimed to investigate the potential of utilising aluminium-rich or aluminous laterite in the development of eco-friendly and affordable cement-based materials through geopolymerisation. Aluminium-rich laterite is readily available in West Africa and South America. This material, which is usually found near the surface or in the top layer of lateritic profiles, holds immense promise for serving as an environmentally-friendly construction material. In this study, the potential of using uncalcined aluminium-rich laterite in the formation of geopolymer was also investigated since laterite is a semi-crystalline material. Additionally, the impact of incorporating calcium-based minerals as secondary precursors on the properties and performance of the derived geopolymer was explored. The calcium-based minerals investigated were calcium carbonate and Portland cement. The objectives of this research, as outlined in Chapter 1, were as follows:

1. To conduct an extensive literature review on the properties, microstructure and durability performance of geopolymers derived from laterite in order to identify the current gaps and develop an appropriate research methodology.
2. To characterise the physical, chemical and mineralogical properties of the aluminium-rich laterite to be used in this investigation.
3. To investigate the rheology, setting times and the heat release during geopolymerisation.
4. To investigate the compressive strength development of the geopolymer derived from aluminium-rich laterite.
5. To characterise the products of geopolymerisation and the pore structure of the hardened material derived from aluminous laterite.

It is worth noting that all of the aforementioned objectives have been successfully achieved and are presented throughout this thesis. In Chapter 2, an extensive literature review is presented, covering the historical development of geopolymer, its mechanisms and fundamental concepts, as well as factors affecting the properties and performance of

geopolymers. Chapter 2 also provides a detailed review of the use of laterite in geopolymerisation, along with a review of laterite as a geological material.

The second objective is addressed in Chapter 3, where detailed characterizations of both calcined and uncalcined aluminous laterites, as well as the secondary precursors employed in this research, are presented and discussed. These characterizations encompassed physical and chemical properties, such as oxide composition, mineralogical phases, particle size distribution, particle micrograph, surface area, and true density. Chapter 3 also includes discussions on the impact of milling and calcination on the laterite's physical and chemical properties.

The third, fourth, and fifth objectives were achieved by experimentally examining the flow behaviour, setting times, and reaction kinetics of the fresh mixes. For the hardened properties, the experimental investigation involved compressive strength testing, pore structure analyses, and phase identification. The laboratory investigation considered three categories of mixes: geopolymer, hybrid, and binary, and each category consisted of both calcined and uncalcined laterite mixes. The hybrid mixes incorporated calcium carbonate and Portland cement, respectively, at a 40% replacement level of the laterites, while the binary mixes only incorporated Portland cement at the same 40% replacement level but without activators. A blend of sodium hydroxide and sodium silicate was used as activators. The outline and descriptions of the experimental procedures are presented in Chapter 4, while results and discussion of the laboratory experiment are found in Chapter 5.

6.2 Conclusions

The findings of this research provide insights into the behaviour of aluminium-rich laterite, as the primary precursor, in geopolymerisation, as well as the impact of incorporating calcium minerals as a secondary precursor. Based on the findings of this investigation, covered in Chapters 3, 4 and 5, the following conclusions can be drawn:

6.2.1 Impact of Milling and Calcination

The milling and calcination were major aspects of the laterite processing, and both were found to influence the physical and chemical characteristics of the laterite. The milling was conducted in a vibratory disc mill to have about 90% of the laterite particles below 45 μm, while the calcination process was carried out in an electric furnace at a temperature of 750 ˚C for an hour.

Apart from reducing the particle size, the milling of the laterite was observed to reduce the crystallinity of the as-received laterite by 16.6% and rendered the kaolinite phase undetectable by XRD. However, the milling process did not remove the hydroxyl group or water molecule

from the kaolinite's structure, as confirmed by TGA and FTIR analyses. The milling process was also found to reduce the amount of heat required to cause dehydroxylation of hydrated minerals, as well as their respective weight losses in the TGA analysis, compared to the as-received sample. These findings indicate that the milling process caused dehydration and alteration in the crystal structure of the constituent minerals.

The calcination of the milled laterite led to the dehydroxylation of hydrated minerals (gibbsite, goethite, and kaolinite), resulting in the formation of alumina (Al_2O_3), hematite (Fe_2O_3), and metakaolin ($Al_2O_3 \cdot 2SiO_2$), respectively. The calcination was also found to reduce the crystallinity of the milled laterite by 11.4%, attributed to the removal of hydroxyl groups. The dehydroxylation resulted in the formation of a new crystal structure, as observed with the appearance of hematite, as well as the formation of x-ray amorphous phases such as alumina and metakaolin. Consequently, the calcination process induced alterations in the crystal structure of milled laterite, which resulted in a lower degree of crystallinity.

The calcination process also resulted in an increase in true density and particle size, as well as a decrease in surface area. The increase in particle size and subsequent decrease in surface area can be attributed to the coarsening of particles induced by the calcination process, while the increase in true density is likely due to the dehydroxylation and particle coarsening.

6.2.2 Factors Influencing the Reactivity of the Laterite

The reactivity of the laterites was found to be more dependent on the mineralogical composition than on particle size and surface area. Although uncalcined laterite had a larger surface area and smaller particles, the shorter setting times (9 times lower) and higher rate of heat release (within the first hour) of the uncalcined laterite geopolymer mix are due to the strong affinity of gibbsite and goethite for hydroxide ions. The presence of these minerals, particularly gibbsite, which was present in a large amount, initiated an immediate reaction with the alkaline solution, leading to rapid precipitation of sodium aluminate silicate.

In contrast, in the calcined laterite, these minerals (goethite and gibbsite) were transformed into hematite and amorphous alumina, respectively, resulting in reduced reactivity. Amorphous alumina and hematite are relatively stable and inert under alkaline conditions at ambient temperature; hence, did not participate in the geopolymerisation reaction.

6.2.3 Factors Influencing Rheology and Flow Behaviour

The rheology and flow behaviour of the geopolymer pastes were influenced by the viscosity of the activating solution, which varied with temperature. In the case of mortars, the flow

behaviour was influenced by the absorption of the fine aggregates. In the absence of activators, the type of laterite used influenced the flow behaviour, as demonstrated in the binary mix category. The paste of the binary mix containing uncalcined laterite displayed superior flow behaviour (higher spread flow diameter) compared to its calcined laterite counterpart.

6.2.4 Factors Influencing Properties and Performance of the Derived Geopolymer

The setting times, heat of reaction, compressive strength, porosity and pore structure, as well as the phase assemblage of the derived geopolymer, were influenced by the type of laterite and the presence and type of secondary precursors (calcium carbonate and Portland cement).

6.2.4.1 Influence of the type of laterite

All mixes containing calcined laterite displayed higher compressive strength, higher cumulative heat of reaction, and lower porosity compared to those made with uncalcined laterite. Notably, all uncalcined laterite mixes within the geopolymer and hybrid categories experienced significant strength regression, which can be attributed to the formation of unstable phases due to the presence of gibbsite in uncalcined laterite.

The presence of gibbsite in a high alkaline environment, such as the geopolymer and hybrid mix conditions, led to its dissolution and subsequent participation in the formation of phases. Meanwhile, in the absence of an activating solution, as shown in the binary mix containing uncalcined laterite, which did not experience a significant decline in strength, the dissolution of gibbsite is inhibited, leading to the formation of stable phases.

The influence of the calcined and uncalcined laterites was manifested primarily in terms of mineralogical composition. Therefore, it is the mineralogical composition of the calcined laterite, particularly the presence of metakaolin, that is responsible for the higher compressive strength, greater cumulative heat of reaction, and lower porosity observed in mixes of the calcined laterite series compared to uncalcined laterite.

6.2.4.2 Influence of Secondary Precursors

Calcium carbonate and Portland cement were incorporated as secondary precursors to promote setting and hardening at ambient temperature (23 ± 2 ˚C). The findings of this investigation revealed that the inclusion of calcium minerals reduced setting times, increased the rate of heat liberation (within the first hour), improved compressive strength, and reduced porosity. Despite the reduction in porosity, the secondary precursors had limited influence on the resistance to isopropanol diffusion (hybrid category).

The presence of calcium carbonate and Portland cement also resulted in the development of calcium-bearing phases, including calcium silicate hydrate (C-S-H), in the calcined laterite mixes of the hybrid category. Portland cement promoted the formation of crystalline C-S-H, detected by XRD and FTIR analyses, while calcium carbonate facilitated the formation of amorphous C-S-H, confirmed by the FTIR analysis. The presence of the C-S-H phase in the calcined laterite mixes of the hybrid category explains why only these two calcined laterite mixes, containing Portland cement and calcium carbonate respectively, achieved the minimum strength required for structural concrete.

However, the presence of calcium carbonate also resulted in severe efflorescence and subflorescence, which, over time, led to a reduction in strength, the development of cracks, an increase in porosity, and subsequent disintegration of some samples. The efflorescence and subflorescence were caused by the huge quantity of unreacted calcium carbonate in mixes containing calcium carbonate, leaving more unbound sodium ions to react with atmospheric CO_2.

6.3 Implications and Practical Applications

Despite the considerable potential of aluminium-rich laterite as a sustainable source of aluminosilicates, the overall findings suggest that it is not a suitable candidate for geopolymerisation. This is due to the low compressive strength observed and the presence of unstable phases, particularly in the uncalcined laterite geopolymer and hybrid mixes.

However, in the context of developing eco-friendly and affordable cement-based material, this research has highlighted the benefits of using aluminium-rich laterite in conjunction with traditional cementitious material, such as Portland cement. The advantages of blending aluminium-rich laterite with Portland cement were demonstrated through the hybrid and binary mixes. Specifically, the binary mixes, where 40% of the calcined and uncalcined laterite were replaced with Portland cement and, in the absence of activators, displayed better performance in terms of compressive strength and resistance to isopropanol diffusion. These findings clearly demonstrate the potential of aluminium-rich laterite as a supplementary cementitious material.

Although the results reveal that the hybrid mix based on calcined laterite and Portland cement is suitable for structural concrete applications, given that it achieved the highest compressive strength and showed enhanced durability (lowest porosity and good resistance to isopropanol diffusion), this mix may not be as cost-effective as its binary counterpart, which, without activators, displayed a similar range of strength development. In terms of cost-effectiveness,

the binary mixes stand out as the most affordable for the given performance. Moreover, these mixes can be tailored in an economical manner to achieve better performance, which includes the application of water curing.

Similarly, the hybrid mix based on calcined laterite and calcium carbonate met the strength requirement for structural concrete and exhibited the second lowest porosity, as well as the presence of amorphous C-S-H. However, its susceptibility to efflorescence and subflorescence might limit its applications.

6.4 Limitations of Findings

It is important to note that the lateritic material employed in this research was sourced from a single geographical location and hence, could serve as a potential limitation in terms of generalising the findings of this study. The characteristics of the extracted laterite used in this study may not be representative of the broader spectrum of aluminous laterite found worldwide or even across West Africa. For instance, some aluminous laterite may have more than one aluminium hydroxide minerals, such as boehmite and diaspore, while for this study, the laterite contained only gibbsite. These aluminium hydroxide minerals may behave differently in the presence of sodium hydroxide. Another potential limitation could be the processing procedures of the laterite, specifically the milling and calcination processes. A variation in the milling time, calcination temperature and duration can impact the dissolution rate of the constituent minerals or the reactivity of the laterite, which could potentially influence the performance of the resultant geopolymer or the outcomes of this study.

6.5 Recommendations for Further Research

Although the overall outcome of this work indicates that aluminium-rich laterite is not an ideal candidate for geopolymerisation, the findings also unveil promising avenues for further research on this material. In light of these insights, the following areas warrant further investigation:

1. Develop a geopolymer composite incorporating both calcined and uncalcined laterite. The uncalcined laterite may replace a portion of the calcined variant to facilitate the immediate release of aluminium, thereby reducing the extended setting times observed in the calcined laterite geopolymer mix and serving as nucleation sites for the formation of N-A-S-H phases.

2. Explore the use of aluminium-rich laterite in waste encapsulation, as some of the identified phases, especially the aluminosilicate phases, have the capacity to immobilise contaminants.
3. Examine how the phase assemblage in the binary mixes can be tailored to improve strength development and microstructure compactness.
4. Utilise gibbsite-rich laterite in the formulation of calcium sulfoaluminate cement or cement containing ye'elimite phase, leveraging its high alumina content.
5. Explore the potential of further enhancing the performance of the geopolymer mix based on calcined laterite despite its suitability for low-strength applications.